Controlled Diffusion Solidification: Process Mechanism and Parameter Study

Controlled Diffusion Solidification: Process Mechanism and Parameter Study

By

ABBAS ABDUL AMER KHALAF, B.Sc., M.Sc.

A Thesis

Submitted to the School of Graduate Studies

in Partial Fulfillment of the Requirements

for the Degree of

Doctor of Philosophy

McMaster University

©Copyright by Abbas Abdul Amer Khalaf, November, 2010

DOCTOR OF PHILOSOPHY (2010) **McMaster University**

(Mechanical Engineering) **Hamilton, Ontario**

TITLE: **Controlled Diffusion Solidification: Process Mechanism and Parameter Study**

AUTHOR: **Abbas Abdul Amer Khalaf**

B. Sc (University of Technology, Baghdad, Iraq)

M.Sc. (University of Technology, Baghdad, Iraq)

SUPERVISORS: **Dr. Sumanth Shankar**

Department of Mechanical Engineering

NUMBER OF PAGES: **xiv, 153**

To My Mother…

Abstract

In the last forty years, most of researches in casting fields especially in semi-solid metal state were dedicated to find new ways to enable near net shaped casting of Al alloys to improve the product properties and decreases the product cost. The thixoforming and rheocasting processes are presented as a ways by which the microstructure of the alloys can be changed to non-dendritic microstructure leading to improve the mechanical properties by mitigating the defect associated with the dendritic microstructure. Unfortunately, these processes have proved to be capital cost prohibitive and complicated for commercial production. Further, near net shaped casting of Al wrought alloys along with the superior properties and performance of these alloys have been a challenge for conventional casting routes due to the main disadvantage of hot tearing or hot cracking during solidification, which renders the cast component ineffective. To overcome the disadvantages of thixoforming and rheocasting processes, Controlled diffusion solidification (CDS) process was innovated to enable casting aluminum alloys with a non-dendritic morphology of the primary Al phase in the resultant cast microstructure and thus alleviating the problem of hot tearing and obtaining a cost effective product with improved mechanical properties. The CDS is a simple process involving mixing of two precursor alloys of different thermal masses (temperature and solute) and subsequently cast the resultant mixture of the desired solute composition and temperature as a near net shaped cast product. The process lends itself to easy commercialization with a marginal capital cost required for set up such as the addition of an extra holding furnace. Further, the CDS process would prove itself to be unique in its ability to cast Al based wrought alloys into near net shaped components without additional processes and cost.

The CDS process has been proven to yield a cast product with a non-dendritic Al phase morphology and this dissertation presents the in-depth details and analysis of the various events occurring during the process to obtain a successful cast part. The process involves various inter-related events such as mixing, re-distribution of thermal field, re-distribution of solute field, three types of nucleation events and growth of these different nuclei. Further the dissertation aims to present a study of the critical parameters such as temperatures of the two pre-cursor alloys, initial mass ratio of these alloys and the rate of mixing them on the effectiveness of the CDS process.

The results from this study shows that mixing two precursor alloys to form the final desired alloy presents a natural environment for copious nucleation events aided by distribution of these nuclei by forced convection followed by the formation of unique cells in the resultant mixture (micro-scale) with significant thermal and solute gradients. The solidification in the CDS process is unique and different from conventional casting process in that initial growth of the nuclei takes place with the solute diffusing towards and temperature diffusing away from the solid/liquid interface which presents a favorable environment for a stable unperturbed growth of the solid/liquid interface resulting in a non-dendritic morphology of the primary Al phase.

The proposed events in the CDS process has been verified with a few Al based wrought alloys and organic alloy systems.

Acknowledgements

At the beginning, I would like sincerely to thank my supervisor Dr Sumanth Shankar for his guidance, patience, valuable support and for giving me this opportunity to complete my PhD study in the casting field especially in controlled diffusion solidification. We had various interesting discussions regarding the present project along the last four years that significantly contributed to remove all the technical difficulties and helped in shaping the path of achieving the goals of the present research activity. Without his encourage and support, this research work and the dissertation could not be completed and presented to all.

I also like to thank deeply the committee meeting members, Many thanks to Dr. Ponnambalam (Ravi) Selvaganapathy and Dr. Hatem Zurob for their guidance and numerous insightful academic discussions.

I extend my sincere thanks to the faculty members, technicians, and non-teaching staff in the department of mechanical engineering for their help and support. I thank Joe Verhaeghe, JP Talon, Mark MacKenzie, Jim McLaren and Ron Lodewyks for their intensive support in machining and welding various components for my experiments.

I would also like to thank my colleagues at the Light Metal Casting Research Centre (LMCRC) for all their help and insightful discussions as well as providing a peaceful environment for study and growth. Special thanks go to my colleagues Dr. Xiaochun Zeng, Dr. Peyman Ashtari and Dr. Manickaraj Jeyakumar for their support.

I would like to thank Doug Culley, Rob Lemmon and Ed McCaffery of the Department of Materials Science and Engineering for their patient assistance in metallography and chemical analysis.

Finally, I would like to thank in deep my family in Iraq. Many thank to my father, my brothers and my sisters also special thanks to my wife, my sons and daughters for being patient throughout my research period.

Table of Contents

List OF Figures

List of Tables

CHAPTER 1. INTRODUCTION

Casting is a commercially important field in which a large numbers of investigators have been dedicated in research and development for more than a century. Techniques such as sand, gravity permanent mould, high and low pressure die casting and squeeze casting have been developed to improve the mechanical properties and reduce the product cost of the metallic alloys. Aluminum alloys have high strength to weight ratio compared to steel and copper alloys and they are classified as light metals and widely used in automotive, domestic and aerospace applications [1,2,3]. Various compositions of alloying elements such as copper, silicon, magnesium and manganese are usually added to Al to obtain a wide variety of mechanical and performance properties, and castability. Al alloys can be broadly classified as cast and wrought alloys depending on the chemical composition and processing route. Figure 1-1 shows a schematic binary phase diagram of a generic Al alloy consisting of Al and another alloying element B; wherein, α and β are primary solid solutions of Al and B, respectively. Most Al alloys used in casting typically form a eutectic phase with the major alloying element as shown in Figure 1-1; wherein, the alloys with compositions past the solid solubility limits of α and close to the eutectic composition are termed cast alloys because of the ability to shape cast these alloys into near net shaped components due to the short freezing range and short residence time in the two phase of semi-solid region.

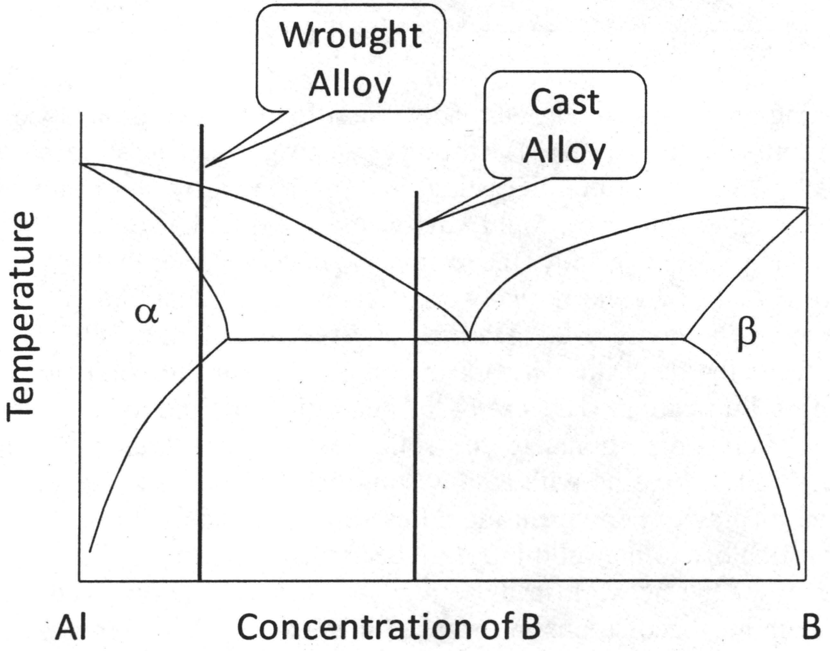

Figure 1-1 Schematic diagram for phase diagram of binary alloys representing limited solubility case.

Alloys with compositions less than the maximum solid solubility of α are termed wrought alloys because of the inability to shape cast these alloys due to the large freezing range inducing casting defects such as hot tearing. Wrought alloys would have to be cast into billets or rods and further transformed into net shaped products via solid state transformation processes such as rolling, extrusion, forging and stamping [4]. Casting processes such as sand, gravity permanent mould, low and high pressure die casting are typically used commercially to cast Al cast alloys. Al-Si hypoeutectic alloy is one of the most widely used Al cast alloy due to its high fluidity/castability and high strength to weight ratio. Table 1-1 shows the notations for identifying various families of Al cast and wrought alloys.

Table 1-1. Notations for various families of Al cast and wrought alloys.

Alloy Element	Cast Alloy	Alloy Element	Wrought Alloy
Al (> 99.0 %)	1xx.x	Al (> 99.0 %)	1xxx
Copper	2xx.x	Copper	2xxx
Silicon, copper, magnesiu	3xx.x	Manganese	3xxx
Silicon	4xx.x	Silicon	4xxx
Magnesium	5xx.x	Magnesium	5xxx
		Magnesium, silicon	6xxx
Zinc	7xx.x	Zinc	7xxx
Tin	8xx.x	Tin	8xxx
Other Elements	9xx.x	Other Elements	9xxx

Recently, casting processes could be broadly classified into two groups, conventional casting and semi-solid metal (SSM) casting. In conventional casting such as sand casting , gravity and pressure diecasting, the molten alloy at a high superheat temperature is poured into the mould cavity and solidified to obtain the near net shaped component [5]. Typically the primary Al phase morphology in the cast microstructure is that of a dendritic network. A simple schematic of such a dendritic network is shown in Figure 1-2. During solidification of these alloys, the liquid continuously feeds the dendritic network to compensate for the volumetric shrinkage associated with solidification. The size of the dendritic arms and the complexity of the network is inversely proportional to the solidification rate of the alloy during the casting process. In processing with a slow solidification rates such as a thick walled casting in sand or gravity permanent mould casting, the feedability in the base of the dendritic network close to the solid interface becomes increasingly difficult due to the large complexity of the network in these regions. Such situations lead to shrinkage porosity and high localized strains in these regions leading to hot tearing as shown in Figure 1-2. Typically these defects occur in the two phase region at solid fractions greater than 0.82 [6].

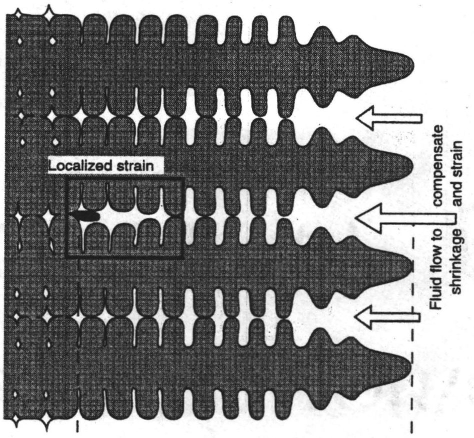

Figure 1-2 Schematic diagram of the microstructure of the primary phase as a dendritic network [6].

To overcome the porosity and hot tearing defects in the dendritic microstructure, semi-solid metal (SSM) casting processes were innovated during the last forty years. Broadly, in the SSM process, the alloys is brought to the two phase semi-solid region and subsequently cast into a shaped component with a pressure assisted casting process such as squeeze casting. The primary phase in the microstructure of the products in SSM casting are typically non-dendritic due to the breakdown of the solidifying dendrites with the application of an external force [7]. SSM processes are broadly classified as thixoforming/thixocasting and rheocasting process. Figure 1-3 (a) and (b) show schematics of temperature-time graphs for typical rheocasting and thixocasting processes, respectively. In, the rheocasting process route (Figure 1-3(a)) the liquid alloy of a desired composition is brought to the semi-solid region (fraction solid of about 0.15 to 0.25) by continuously applying an external force such as mechanical, magneto hydro dynamic or electromagnetic force on the cooling liquid to induce forced convection coupled with copious nucleation of the primary solidifying phase in the liquid. Further, the semi-solid slurry in maintained in an isothermal environment in an induction furnace for a few minutes to enable thermal homogenization and stable/homogenous growth of a non-dendritic primary phase. The slurry is subsequently cast into a shaped component via a pressure assisted casting process. In thixocasting/thixoforming (Figure 1-3(b)), the alloy melt of a desired composition is initially solidified as billets or rods with a highly grain refined primary phase caused by means of rapid solidification, grain refinement and/or stirring. These billets are further sectioned into slugs to the required dimensions and weight as dictated by the final shaped component. The slugs are then heated and maintained in an isothermal environment of an induction furnace at a temperature in the semi-solid region as dictated by a fraction solid of about 0.15 to 0.25 in the alloy phase diagram; after which they are cast into shaped components by a pressure assisted casting process [8,9].

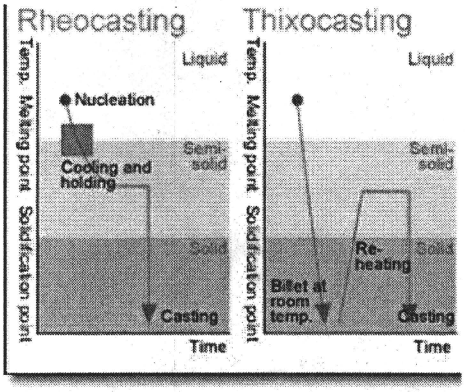

(a) (b)

Figure 1-3 Schematic process plots of the temperature versus time for (a) rheocasting and (b) thixocasting[8].

The thixocasting/thixoforming processes have been cost prohibitive due to the additional stages of billet casting and re-heating. Hence, these processes are being phased out commercially. Most of the rheocasting processes have been under research and development for the past thirty years except the New Rheocasting Process (NRC) [10]; because of the high capital cost and the inability to overcome inclusions and casting defects in most processes. The NRC has had limited commercial success [11].

The controlled diffusion solidification (CDS) was innovated to enable casting Al based cast and wrought alloys into near net shaped components with a non-dendritic morphology of the primary Al phase in the cast microstructure. The novelty of the CDS technology circumvented the problems associated with shaped casting Al wrought alloys such as hot tearing and enabled successful shaped casting of alloys such as the 2xxx, 3xxx, 4xxx, 5xxx and 7xxx Al alloy series [12]. Figure 1-4 shows a comparative example of a product cast in a ring mould with the Al 2014 wrought alloy and cast via conventional and CDS processes, respectively. The conventional process generate significant hot tearing in the cast part (Figure 1-4(a)) and the CDS process presented a defect free casting (Figure 1-4(b)) [13].

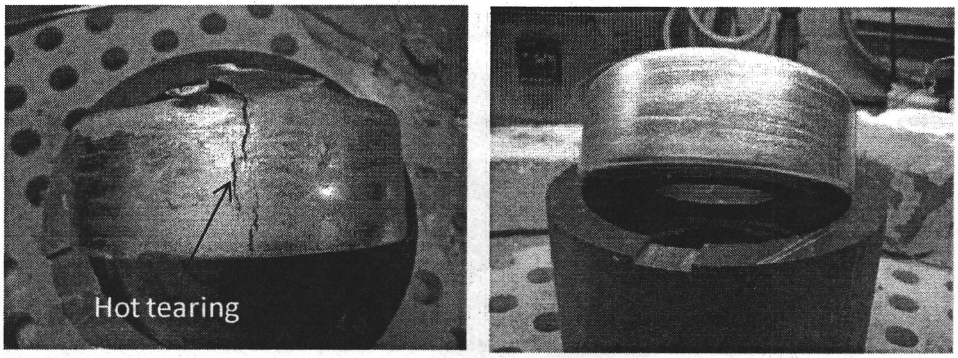

(a) (b)

Figure 1-4 Ring mould test of Al 2014 wrought alloy made by (a) conventional casting and (b) CDS process.[13]

A schematic of the CDS process is shown in Figure 1-5; wherein two precursor alloys of specific temperature and composition are mixed and subsequently cast as a shaped component in a process that may or may not be pressure assisted. In the CDS process, the mixing of the two alloys induces both the forced convection and copious nucleation of the primary Al phase which establishes a favorable initial condition to obtain a non-dendritic phase morphology.

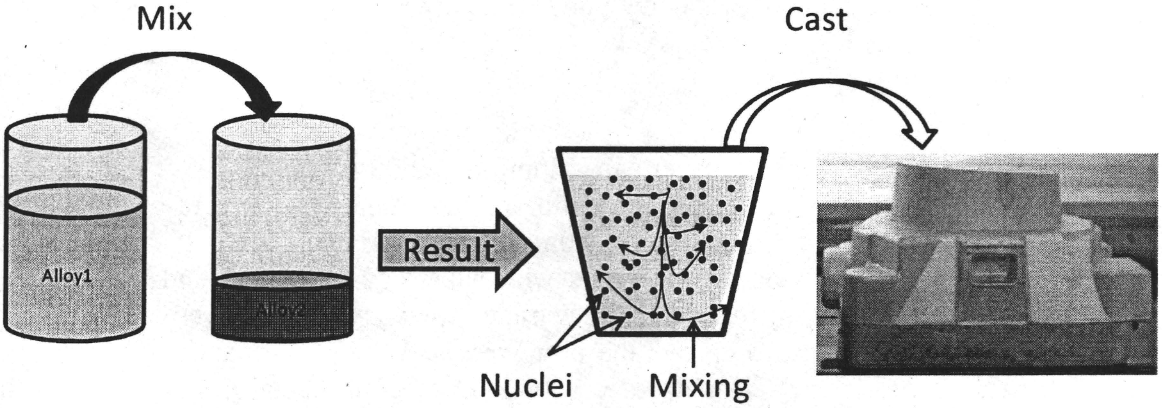

Figure 1-5 Stages in a typical Controlled Diffusion Solidification (CDS) process.

The CDS process presents a promising and viable casting process to enable high integrity shaped casting of Al wrought and cast alloys with a non-dendritic morphology along with the associated advantages of high mechanical and performance properties. Understanding the mechanism of the solidification in a CDS process is critical to identify and optimize the critical process and alloy parameters.

The following features distinguish the CDS process over other SSM processes (Thixoforming and Rheocasting).

1. *Less Process Time:* Lack of any isothermal holding time (~10 min for other SSM processes) at the semi-solid temperature.
2. *Flexibility of Casting Process:* Ability to cast with and without a pressure assisted casting process.
3. *Simplicity*: The simplicity of the process lies in the minimal additional processing steps over SSM casting processes. The additional steps involve mixing a two precursor alloys at controlled temperature and alloy compositions before casting the mixed slurry in a mould.
4. *Low Capital Cost*: The simplicity of the CDS process results in a low capital cost for commercial processing. The only additional cost would be that of an additional melting and holding furnace.
5. *Low Production Cost*: Since the CDS process involves minimum additional processing steps over the conventional process, the cost increase in part production would be marginal as compared to the fairly high cost of manufacturing with other SSM processes [12,9,14]
6. *Non dendritic microstructure*: The cast part using the CDS process results would have a non dendritic primary phase in the solidified microstructure without any entrapped liquid phase or any extraneous phases entrapped during the semi-solid processing.[12,9,14,15].
7. *Shape Cast Al wrought alloys*: The CDS process would uniquely be able to shape cast Al based wrought alloys which would present commercial possibilities of producing parts with superior mechanical and performance properties.

Canada is one of the global players in Aluminum industry and one of the priority mandates for the government is to focus on the research and development of innovative, environmentally friendly and economic casting processes to enable manufacturing of net shaped structural components of Al alloys with superior mechanical and performance properties. A thrust area for research has been identified as developing novel techniques such as semisolid casting to improve the properties and the performance of the casting and increases the efficiency of the process [16]. Thus, commercial development of the CDS would be valuable and understanding the mechanism of solidification in this technology would be the first steps in the commercial development.

CHAPTER 2. NOMENCLATURE

The nomenclature used in the dissertation to define the various alloys and parameters are given below:

Text Notation	**Description**
A	Area
Alloy1	Precursor alloy with higher thermal mass (higher temperature and higher mass).
Alloy2	Precursor alloy with lower thermal mass.
Alloy3	Resultant desired alloy.
C	Solute Concentration
D	Solute Diffusion Coefficient
G	Temperature gradient
G°	Molar Gibbs free energy
L	Latent heat of fusion
c	Specific heat capacity at constant pressure
L	Characteristic length
m	slope of the Liquidus
mr	Mass ratio (m_1/m_2)
k	Equilibrium partition ratio
N	Number
R	Radius of the Nucleus
r	Critical radius calculated from nucleation theory
S/L	Solid –liquid interface
T	Temperature
t	Time
V	Growth rate
X	Spatial dimension
u	Velocity
ξ	Transient position of extent intersection of temperature and concentration curve.
ρ	Density
μ	Dynamic viscosity
γ	Interfacial surface energy.
K	Thermal conductivity coefficient
α	Thermal diffusivity
δ	Perturbation amplitude
ω	Frequency of sinusoidal perturbation
σ	Surface tension
ΔT	Undercooling below alloy liquidus temperatures.

Subscript Notation	**Description**
1,2,3	Represents Alloy1, Alloy2 and Alloy3 respectively

A	Element A
actual	Actual temperature in the cells morphology in Area2
B	Element B
c	Critical radius
cu	Copper
Initial condition	Initial condition of the temperature in Area2
L	Liquid
L1, L2, L3	Liquidus temperatures of Alloy1, Alloy2 and Alloy3, respectively
liquidus	Instantaneous liquidus temperature
m	Melting point temperature
o	Pre-exponential factor, resultant alloy solute.
Pe	Peclet number
quench	Quenching process
s	Solid
T	Total length
v	Latent heat of fusion
We	Weber Number
∞	Bulk condition

CHAPTER 3. OBJECTIVES AND THESIS PLAN

This chapter presents the objectives of this project and the project plan adopted to successfully address the objectives.

3.1. OBJECTIVES

The following are the main objectives of this project.

- Develop an in-depth quantitative understanding of the sequence of events occurring in the CDS process, specifically the mixing of the two precursor alloys, thermal and solute field homogenization and solidification.
- Identify, describe, quantify and optimize the critical alloy and process parameters that affect the sequence of events in the CDS process.

3.2. PROJECT PLAN

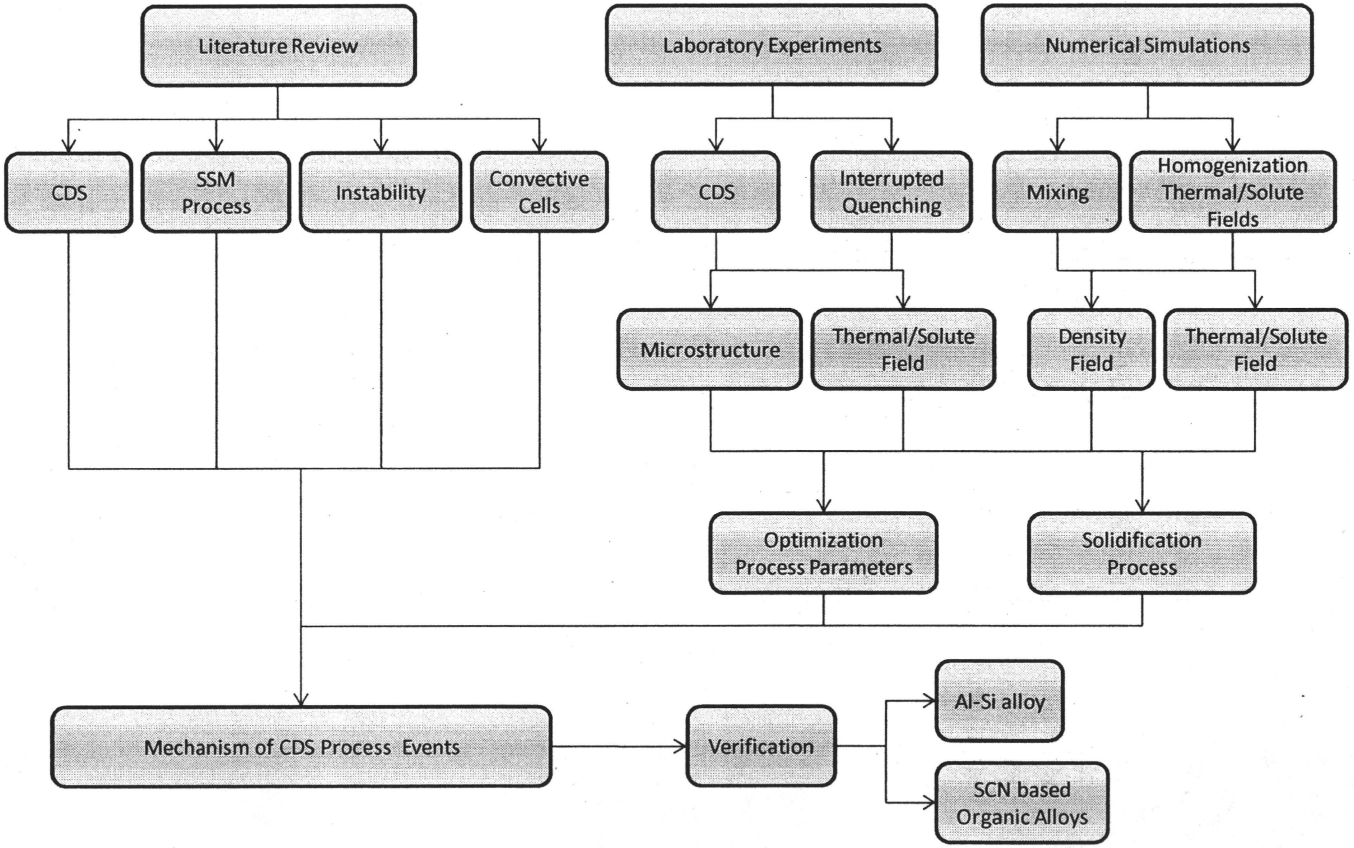

CHAPTER 4. REVIEW OF PRIOR ART

In this chapter an in-depth review of the prior-art in the following areas related to this project would be presented:

- Review of the CDS art
- Semi-Solid Metal Processing of Al alloys
- Mixing of two Fluids
- Solidification of Alloys

4.1. REVIEW OF CDS ART

Controlled diffusion solidification (CDS) was innovated to cast Aluminum cast and wrought alloys into near net shape components with a non-dendritic morphology of the primary Al phase. The process was developed to mitigate the inter-dendritic shrinkage and significantly reduce the network forming tendencies of the dendrites to decrease hot tearing in wrought alloys during solidification. The concept of diffusion solidification was first developed and patented by Goetzl and Ellis[17] in 1952 for casting steel. Later the process was further investigated and developed by Langford and Cunningham [18] and Langford and Apelian [12,19]. In diffusion solidification, as shown in Figure 4-1, solid particles with solute composition C_1 is introduced into the liquid with solute composition of C_L and the mixture is held isothermally to attain a final homogeneous solute composition of C_2 in the resultant solid as shown in Figure 4-1. In conventional casting a liquid with solute composition of C_2 is directly cast in to a mould from a sufficient superheated temperature above the respective liquidus (Figure 4-1). In diffusion solidification, the solidification strongly depends on the rate of solute diffusion between the solid particles and liquid and the solidification time is independent of the size of the casting while in the conventional solidification; it strongly depends on heat extracted from the melt and dependent on the size of the casting.

a) PHASE DIAGRAM

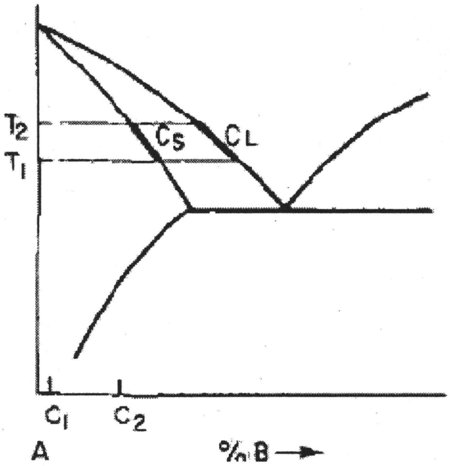

C_1 = COMPOSITION OF PREEXISTING SOLID

C_2 = AVERAGE COMPOSITION OF THE MIXTURE OF SOLID AND LIQUID

C_S = SOLUTE CONCENTRATION AT SOLID/LIQUID INTERFACE

C_L = COMPOSITION OF LIQUID

T_2-T_1 = TEMPERATURE RISE DUE TO THE HEAT OF SOLIDIFICATION

b) MECHANISM: SOLID AND LIQUID MIXED INSTANTANEOUSLY IN A REFRACTORY VESSEL

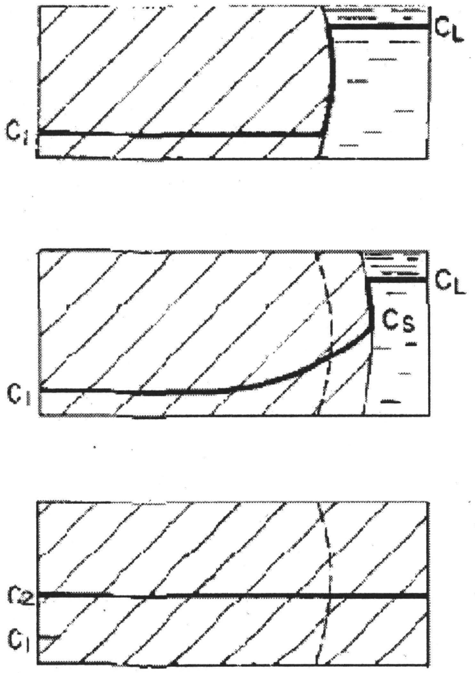

START AT TEMPERATURE T_1
NO DIFFUSION HAS TAKEN PLACE

PARTIALLY SOLIDIFIED; HEAT IS EVOLVED AT THE SOLID/LIQUID INTERFACE AS B DIFFUSES INTO THE SOLID; C_L DECREASES

COMPLETELY SOLIDIFIED; ENTIRE PRODUCT HAS BEEN HEATED TO T_2. IF HELD SUFFICIENTLY LONG, HEAT WILL BE DISSIPATED AND THE PRODUCT WILL RETURN TO TEMPERATURE T_1; SOLID IS HOMOGENEOUS WITH RESPECT TO B

Figure 4-1: Mechanism of diffusion Solidification (a) binary alloy phase diagram and (b) mechanism of diffusion solidification [18].

In the CDS process, as shown in Figure 4-2, two precursor liquids, Alloy1 and Alloy2 of specific solute compositions of C_1 and C_2, respectively and temperatures T_1 and T_2, respectively are mixed such that the a resultant alloy, Alloy3 is obtained with a solute composition of C_3. The Alloy1 with a higher thermal mass (temperature and mass) is mixed into the Alloy2 with a lower thermal mass to obtain a homogeneous mixture of Alloy3 and the forced convection during the mixing of alloys coupled with the copious nucleation of primary Al phase from Alloy1 mixed into Alloy2 would establish favourable conditions for a non-dendritic morphology of the primary Al phase in the resultant solidified structure of Alloy3.

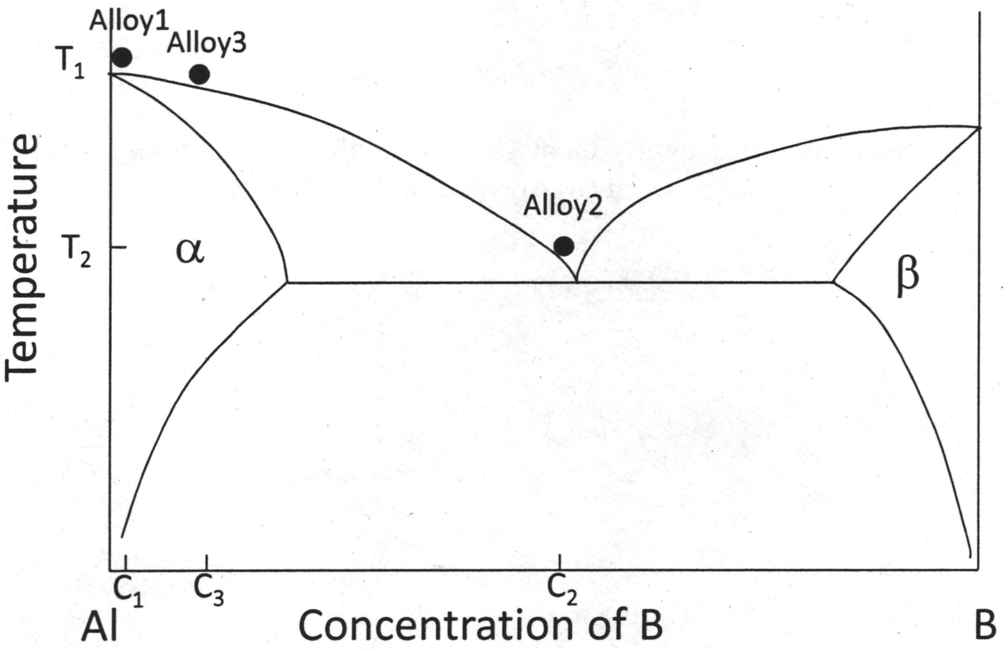

Figure 4-2: A typical binary phase diagram showing the CDS process technology.

Saha et al [12] have demonstrated the proof of concept of the CDS process by producing a solidified part of Al-4.4wt% Cu by mixing a higher thermal mass of pure Al at 665 °C into a lower thermal mass of Al-33wt%Cu eutectic alloy at 550°C. The optical micrographs shown in Figure 4-3 reveal the non-dendritic microstructure of the primary Al phase in the CDS process compared with the predominantly dendritic Al phase morphology in the conventional cast structure of the Al-4.4wt%Cu alloy. The 2014 Al-Cu wrought alloy was cast into a wedge shaped steel mould via CDS process and conventional process [12]. Figure 4-4 shows the results of this study wherein the dendritic microstructure dominate in all conventional castings at various cooling rate and different initial superheat temperature while a non-dendritic structure was obtained in the CDS process for all cooling rates. In the CDS process, the globularization of the primary phase was inversely proportional to the cooling rate of solidification as shown in Figure 4-4 (a) and (d).

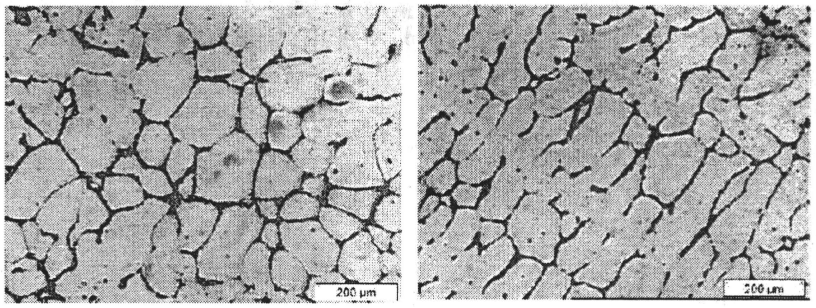

(a) (b)

Figure 4-3: Microstructure images of Al-4.4wt%Cu wrought alloy (a) CDS process and (b) conventional casting [12].

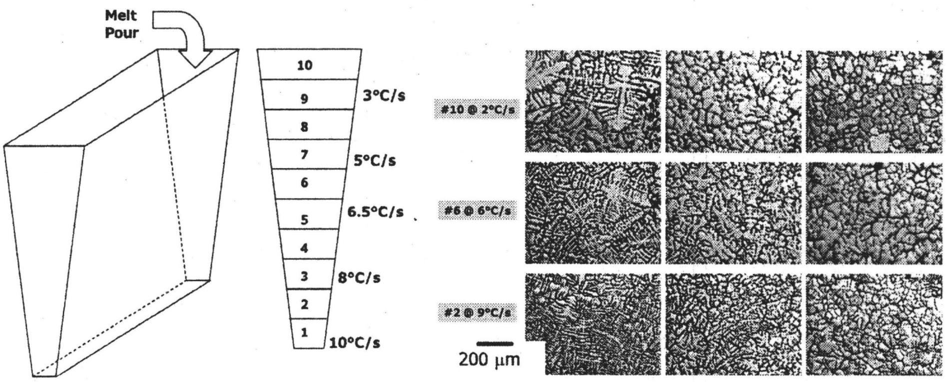

(a) (b) (c) (d)

Figure 4-4: A microstructure of 2014 alloy for different cooling rate cast into wedge mould via CDS and conventionally, (a) schematic of the wedge mould and cooling rate obtained at different depth, (b) conventional casting poured at 50°C superheat temperature, (c) conventional casting poured at 5°C superheat temperature and (d) CDS process [12].

Saha et al [12, 20] further demonstrated the CDS process by casting the 2014, 4145, 5056 and 7050 Al wrought alloys, and 222 and 319 Al cast alloys (as shown in Table 4-1) with a non-dendritic primary phase morphology. They found out that in all these experiments, the morphology of the primary Al phase became more dendritic as the superheat of the Alloy1 increased.

The commercial viability of the CDS process was amply demonstrated by the sound and defect free shaped castings of an automotive ABS housing by gravity tilt pour permanent mould casting process (Figure 4-5(a)) and a plate casting sand casting process (Figure 4-5(b)) by Shankar [21].

Table 4-1: wrought alloys and cast alloys used by [12].

Alloy System	Commercial Alloy	Precursor Alloy #1			Precursor Alloy #2		
		C (wt. %)	T (°C)	W	C (wt. %)	T (°C)	W
2xxx	2024	100Al	665	0.86	67Al-33Cu-1.5Mg	552	0.14
4xxx	4145	87.3Al-12.7Si	585	0.85	67Al-33Cu	552	0.15
5xxx	5056	100Al	665	0.86	65Al-35Mg	458	0.14
7xxx	7050	90.9Al-6.4Zn-2.7Mg	640	0.89	78Al-22Cu	593	0.11
2xx.x	222.0	100Al	665	0.73	67Al-33Cu	552	0.27
3xx.x	319.0	93Al-7Si	620	0.88	67Al-33Cu	552	0.12

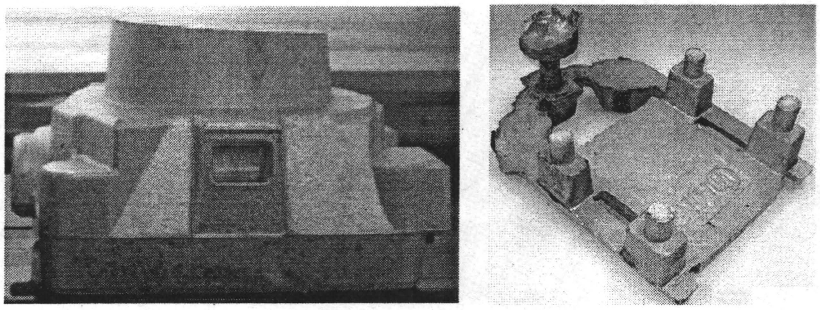
(a) (b)

Figure 4-5: Sample products made via CDS process (a) Automotive Automatic Breaking System housing by tilt pour permanent mould casting and (b) plate by sand casting [21]

Apelian et al [22] laid out a theoretical framework consisting of three salient conditions for a successful CDS process with a non-dendritic microstructure, as illustrated below:

- *Thermodynamic consideration*: the Gibbs free energy of two liquids before mixing process must be less than that of the resultant alloy at its liquidus temperature. Equation 4-1 [22,23,24] presents the total Gibbs free energy per mole after mixing two elements (A and B). However Figure 4-6 clearly shows that there is difference between the Gibbs free energy of the mixture obtained by

CDS and the alloy of the same composition in a conventional solidification. Accordingly, it was suggested that the temperatures of the two precursor alloys should be closer to their respective liquidus temperatures so as to make a mixture with a lower Gibbs free energy.

Equation 4-1

$$G_m = RT(X_A\, LnX_A + X_B\, LnX_B) + \alpha RTX_AX_B + (X_AG_A^O + X_BG_B^O)$$

Where R is the gas constant, T is absolute temperature, α is the regular solution constant, X_A and X_B are the mole fractions of A and B respectively and G_A^o and G_B^o are the molar Gibbs free energies of the pure elements A and B in the binary solution.

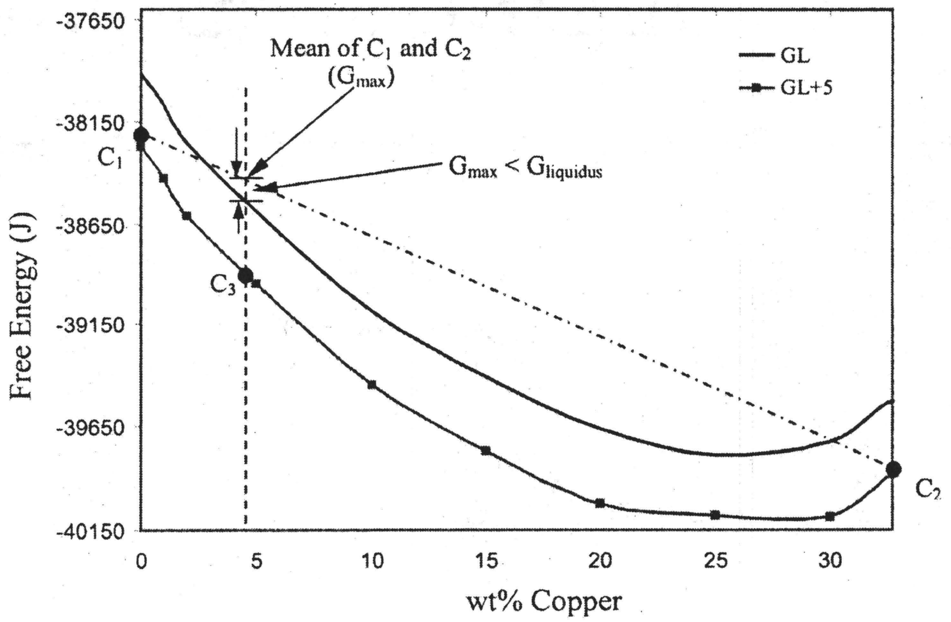

Figure 4-6: Gibbs free energy of Al-Cu alloy as a function of Cur content at liquidus temperature ($G_{liquidus}$) and at 5°C superheat ($G_{liquidus}$+5) [22]

- *Liquid mixing consideration*: when two liquid at different thermal mass mix, a pockets of undercooled liquid form in the mixture. Since the temperature equilibrates faster than the solute, fluctuation in concentration can provide favorable sites to forms nucleation in the resultant mixture [25].
- *Solidification consideration*: during the mixing process the nuclei of the primary Al phase would be exposed to turbulence and initially grow with a rosette shaped morphology which changes to a globular morphology with increases turbulence [26,27].

The work by Apelian et al [22] presents a general overview of the necessary conditions for a successful CDS process. However, specific events during the various stages of the process have not been identified nor the critical process parameters optimized. These would form the principle objectives of this dissertation.

Symeonidis et al [13] had used Al-Cu system to study the mechanism of the CDS process. Pure Al was mixed into Al-33wt% Cu to make Al-4.5 wt%Cu as the resultant alloy. The mechanism proposed was broken down into three steps , mixing, nucleation and growth as shown in Figure 4-7 (a), (b) and (c) respectively.

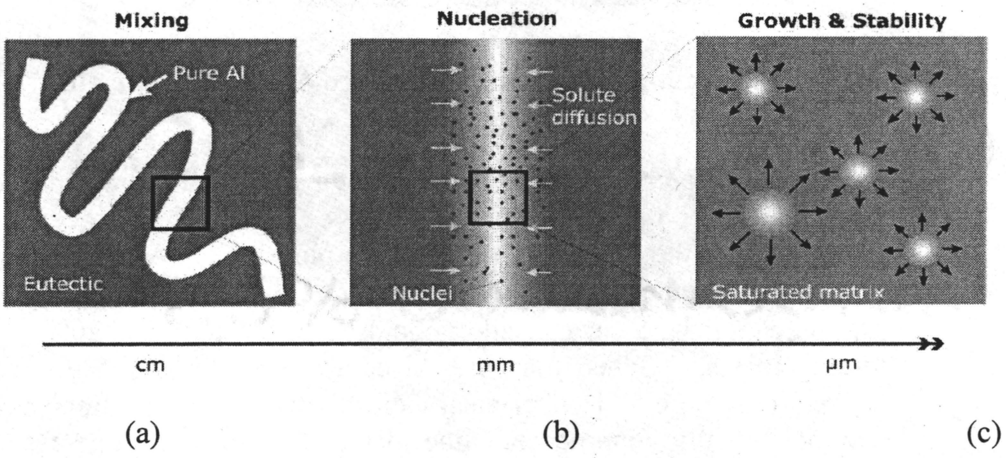

Figure 4-7 Three steps of CDS mechanism proposed by [13], (a) mixing, (b) nucleation and (c) growth.

The three steps of the mechanism were illustrated below;

1) *Mixing step*: the total energy of the resultant mixture equals to the sum of the energies of the two mixed alloys plus a small amount of heat of mixing. The two mixed liquids form striations of each other in the resultant mixture followed by the solute diffusion from the eutectic alloy towards pure Al. Figure 4-8 shows the striations form at the interface between pure Al and Al-Cu eutectic alloy. The solute diffusion equation and the heat diffusion equation have been solved numerically to study the evaluation of undercooling between pure Al and eutectic alloy morphology in the striation. The numerical results show that the thermal equilibrium across the Al striation takes place after 0.05s whereas the solute equilibrium occurs after 0.5s. The difference was due to the thermal diffusivity much faster from solute diffusivity.

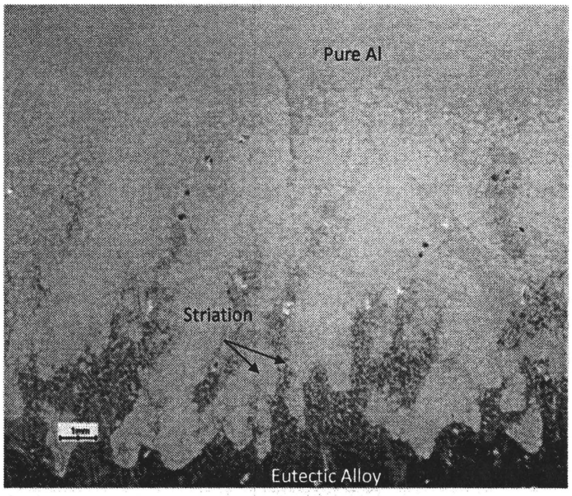

Figure 4-8 striation forming during mixing of pure Al into eutectic alloy.[13]

2) *Nucleation step*: Figure 4-7(b) shows a schematic diagram for the observation for the nucleation taking place in the CDS process. It was proposed that the nucleation occurs from pure liquid (Al) due to the heat extraction by eutectic Al-33wt%Cu alloy. The predicted undercooling of the pure Al in the eutectic alloy could be in the range of 20°C to 60°C during mixing. When the pure Al come together with Al-Cu eutectic alloy, the pure Al nucleates before the final mixture becomes compositionally homogeneous due to the heat transfer being faster than the solute transport. Figure 4-9 drawn from numerical data of solving the heat and solute equations shows that that the nucleation takes place from pure Al due to being exposed to a high degree of undercooling. However facilitating of nucleation from pure Al in the striation occurs in the centre of the striation (χ=0) more than that in χ=0.55 due to bigger undercooling existing in the centre of the striation.

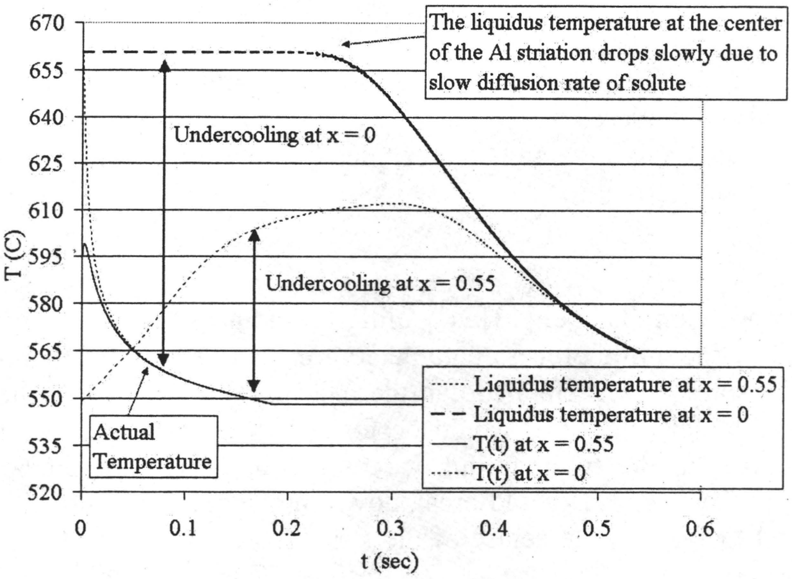

Figure 4-9: Actual and numerical thermal date in Al striation at χ=0 (centre) and χ=0.55 (periphery) drawn with the respective liquidus temperature showing the undercooling of pure Al [13].

Symeonidis et al [13] showed that the primary Al phase nucleates from the pure Al and not from the bulk mixture after mixing by adding grain refiners for the primary phase in the pure Al before mixing. The grain refiners resulted in a refinement of the primary Al phase grains. When the grain refiners were added to the Al-33wt%cu alloy before mixing, no refinement of the primary Al grains were obtained in the final solidified alloy. Figure 4-10 (a),(b) and (c) shows the micrographs from the study with the grain refiners.

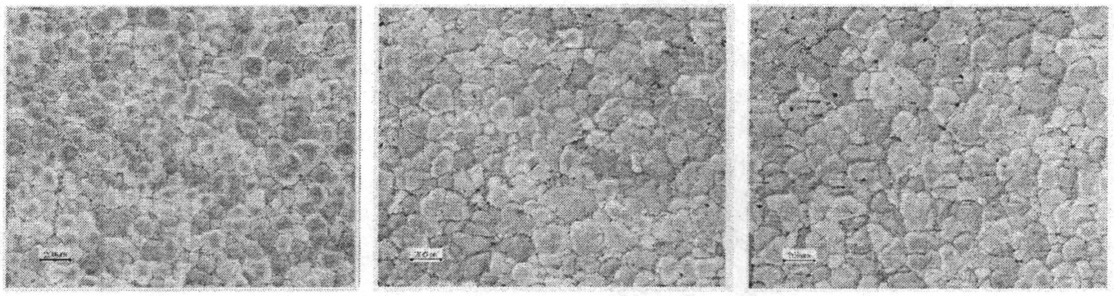

(a) (b) (c)

Figure 4-10 Typical microstructure from adding grain refiner adding during the CDS process (a) adding to pure Al, (b) adding to eutectic alloy and (c) adding to Al-4.5%Cu form conventionally[13].

3) *Growth step*: the nuclei formed from pure liquid will exist in a solute rich and undercooled liquid. This condition will prevent the constitutional undercooling and hence, leading to the formation non- dendritic microstructure

The work by Symeonidis et al [13] is qualitative and no efforts were made to identify, quantify and optimize the process parameters for a successful CDS process. Further, in the mixing stage, it was claimed that the Alloy1 would mix into Alloy2 in form of striations. Although, striations would be formed in the first instant of mixing, they would soon break up due to the turbulence dissipation energy and the continuity of the mixing stream from Alloy1 would break down into segments. Further, the nucleation was proposed to form in the centre of the striations of Alloy1 and was hypothesized with no experimental evidence. The results of experiments presented in this dissertation contradict the proposed nucleation mechanism [13] during the initial stages of mixing. The outer regions of the striations of Alloy1 would be at a lower temperature in contact with the striations of Alloy2 and hence, these outer regions would be more prone to have the nucleation events. However, the proposal that the first nucleation in the mixture is the primary Al phase from Alloy1 was an accurate assessment. The reasons for the stable growth of the S/L interface in the final stages of CDS are speculative and no experiment evidences were presented to substantiate the stability of the S/L interface during the growth stage.

Along with this doctoral dissertation, there were two researchers working alongside in tandem to develop the optimum CDS process conditions for commercial applications. Peyman et al [28] have studied the effect of alloy composition and superheat of the Alloy1 on the microstructure of the resultant casting by the CDS process. They had cast Al wrought alloys such as 2024, 7005 and 7075 via the CDS process by using the mechanism proposed in this dissertation as published by Khalaf et al [29, 30]. The optimum process conditions were briefly outlined as below:

1. The difference between the liquidus temperature of the precursor alloys before mixing should be more than 80°C for the alloys being investigated
2. The maximum temperature attained during mixing of the two alloys should preferably be more than the liquidus temperature of the resultant alloy to facilitate complete filling of the casting mould.
3. The mass ratio between the two precursor alloys should be equal to or more than 3.

Birsan et al[31] have used the mechanism proposed in this dissertation and presented by Khalaf [29,30] to cast the 2024, 6082 and 7075 Al wrought alloys via CDS process into near net shaped components by the tilt pour permanent mould casting process. The wrought alloys 2024, 6082 and 7075 have been made by mixing two precursor alloys which had been chosen in a way such that the different temperature between the precursors alloys before mixing were more than 60°C. The investigators have optimized the parameters for the three wrought alloys for the CDS process. Figure 4-11 (a), (b) and (c) shows the results of this study with the 2024 alloy, wherein the globular non-dendritic morphology of the primary phase in the microstructure dominates at low superheat temperature of the Alloy1 (2°C) and it changes to a rosette like non-dendritic morphology at a superheat of 15°C for Alloy1 and the morphology becomes fully dendritic at a superheat of 25°C for Alloy1. The results validate the mechanism proposed in this dissertation. Figure 4-12 (a) and (b) shows the results of this study for the 6082 and 7075 alloys, respectively at optimum process conditions; wherein the non-dendritic morphology were obtained by the CDS process.

Subsequently Birsan et al [31] developed the methodology to cast the 2024, 6082 and 7075 Al wrought alloys into near net shaped components by the tilt pour gravity casting process. A steel mould was pre-heated to 350°C along with a pouring cup which was preheated as well. The mixing process was carried out in the pouring cup and the tilt of the machine poured the resultant alloy mixture into the die cavity enabling a solidified shaped casting. The castings were further heat treated to various temper levels and mechanical properties were determined. Figure 4-13 (a) shows typical scanning electron microscopy (SEM) images for fracture surface taken from the cross section of a typical tensile test sample of the 7075 alloy casting. The fracture surface of a CDS casting is compact with non-dendritic microstructure with no visible casting defects, whereas that of a conventional casting had no integrity or strength in the dendritic microstructure which was filled with voids and shrinkage cavities from the hot cracking phenomenon (Figure 4-13(b)). Figure 4-14 shows comparative photographs of the as cast samples of the 2024 wrought alloy, showing hot cracking defects in the conventional process (Figure 4-14(a)) and no defects (sound casting) in the CDS (Figure 4-14(b)). Table 4-2 shows the results of the tensile testing for the three alloys showing that the CDS process produced good castings with reasonable integrity as compared to the bad casting with no integrity produced by the conventional casting process.

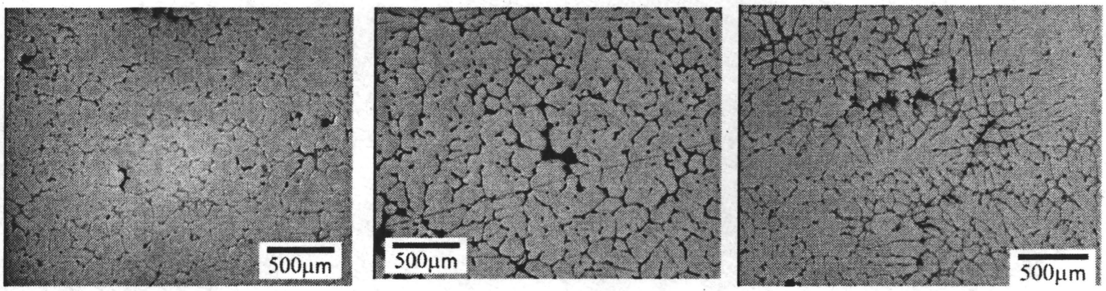

(a) (b) (c)

Figure 4-11 Microstructure images for 2024 wrought alloy made by CDS mixed at different superheat of first precursor alloy, a) 2°C , b) 15°C and c) 25°C [31]

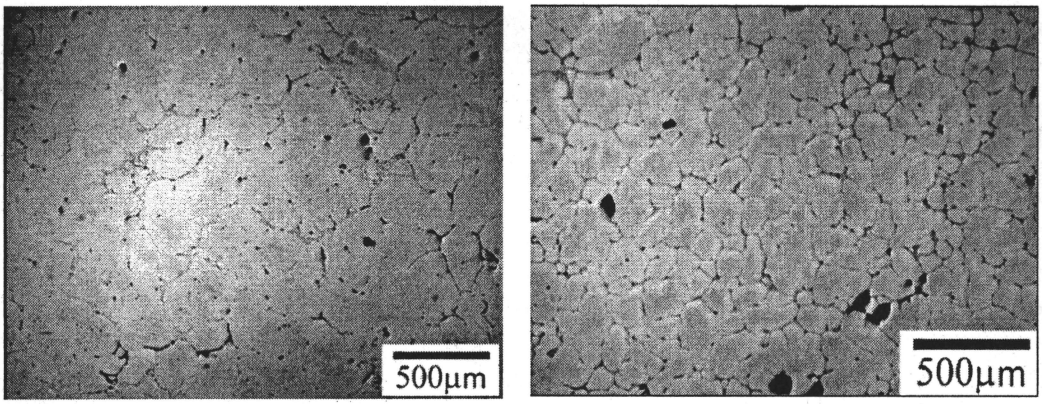

(a) (b)

Figure 4-12 Microstructure image for 6082 and 7075 wrought alloys mixed by CDS process a) rosette grains mixed with equiaxed (6082) and b) fully globular (7075) [31].

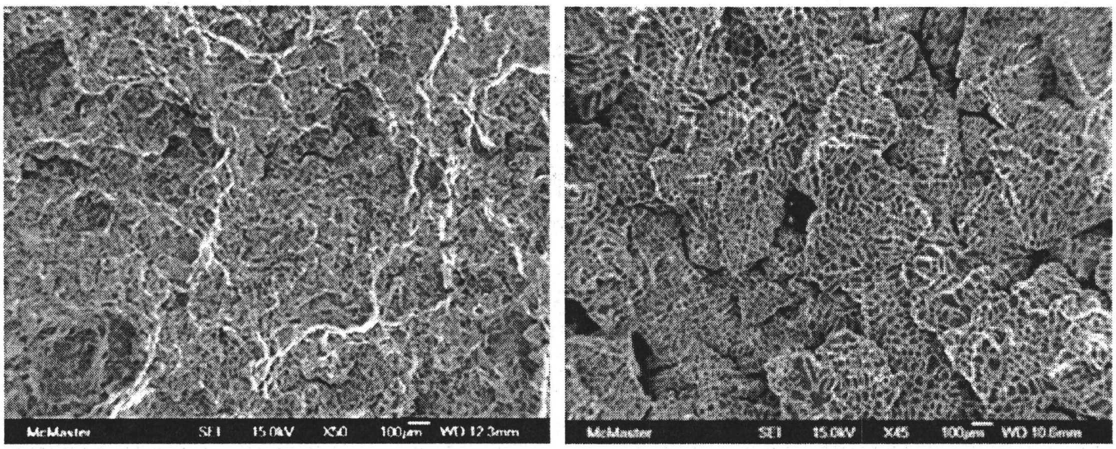

(a) (b)

Figure 4-13 Typical scanning electron Microscopy (SEM) images for 7075 wrought alloy shows fracture surface of the tensile bar cross section a) CDS and b) as cast [31].

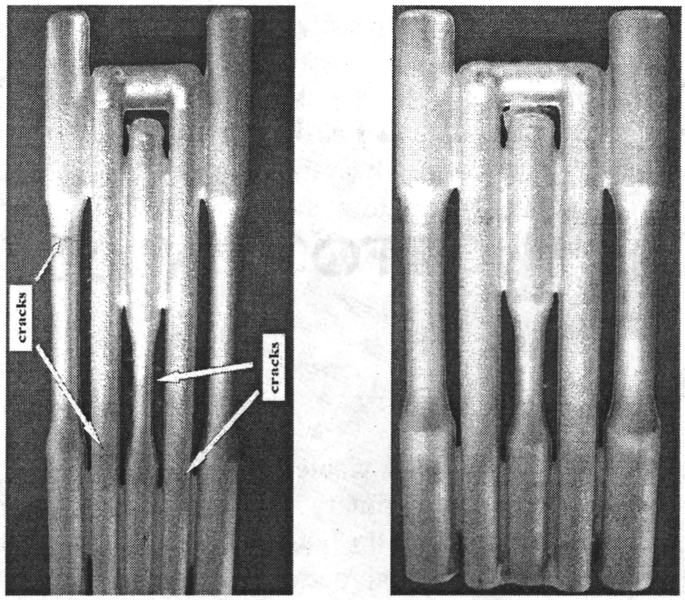

(a) (b)

Figure 4-14 Photograph of cast parts produced in tilt pour casting equipment for 2024 Al alloy a) as cast showing cracking on the casting surface, b) CDS (sound cast) [31]

Table 4-2 Tensile properties of the alloys cast in the tilt pour casting by CDS [31].

Alloy	Temper	UTS (MPa)	YS (MPa)	Elongation %
2024	As cast	217.6	152.5	1.04
	T4	212.8	142.9	1.09
	T6	212.5	151.4	0.9
6082	As cast	184.9	99	3.24
	T4	208.19	106	3.64
	T6	287.9	230.13	2.34
7075	As cast	162.3	109.6	1.08
	T4	221.57	97.3	9.37
	T6	324	301.12	0.79

The review of the limited background literature for the CDS process shows that it is a viable process to produce sound shaped castings of both the Al wrought and casting alloys by commercial processes. However, there is a lack of understanding of the mechanisms involved in the various stages of the CDS process and such an understanding is imperative to develop optimum and lucrative commercial processes to shape cast Al alloys with superior mechanical and performance properties. The work carried out in this dissertation is devoted to enabling such an in-depth understanding of the mechanisms of the CDS process.

4.2. SEMI-SOLID PROCESSING OF AL ALLOYS

Semi-Solid Metal (SSM) processing is a viable casting process for Al cast alloys wherein a non-dendritic morphology of the primary Al phase could be obtained in the cast microstructure. Since, CDS also aims to obtain a non-dendritic cast microstructure, a thorough literature review of the SSM processing of Al alloys was carried out in this project to better understand the mechanism and circumstances of such processes.

In 1971 Spencer et al [32], applied shear stress on Sn-15%WtPb alloy during the solidification process to study the hot tearing of steel alloys. The result of applying shear stress was a change in the primary phase morphology in the microstructure from a dendritic to non-dendritic [7, 33,] as shown in Figure 4-15. Since then, a significant opportunity was introduced to develop casting processes enabling non-dendritic primary phase morphology in the cast microstructure along with the benefits offered by such a microstructure. Hence, SSM processing routes of thixoforming/thixocasting and rheocasting was developed.

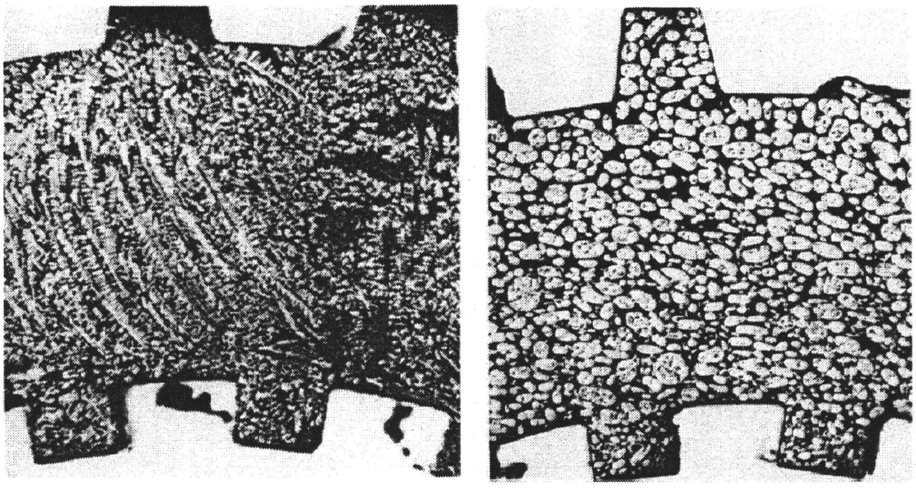

(a) (b)

Figure 4-15Microstructure of Sn-15%Pb alloy,(a) before applied shear stress and (b) After applied shear stress [33].

In SSM processing, when the solid fraction is less than 0.25, the alloy behaves as a liquid-like and called slurry whereas, when the solid fraction becomes more than 0.6, the alloy behaves as a solid-like and the alloy is called a mush. Generally, when the solid fraction is less than 0.5, the solid are not inter-connected in the alloy contrary to the case at which the solid fraction becomes more than 0.5 as shown in Figure 4-16 [34,35].

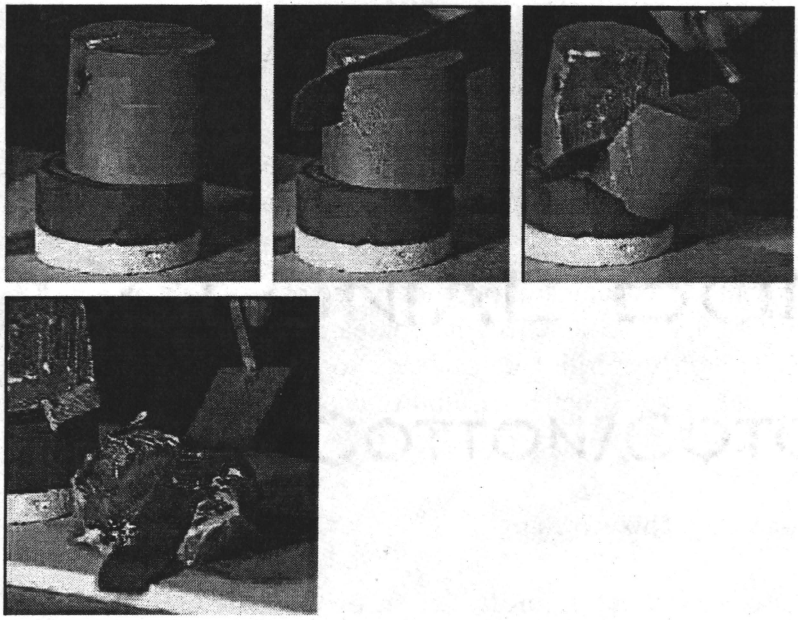

Figure 4-16: A semi solid state with fraction solid more than 0.5 showing a solid–like (thixotropic behaviour) mush [35].

The SSM is strongly affected by rheological properties. Rheology can be defined as the science of flow and deformation of materials. The advantages of using SSM in the casting processes are illustrated below [35].

1. The alloy can completely fill the mould cavity to obtain a near-net shaped final product.
2. Since the SSM temperature is less than the liquidus temperature of the alloys, the thermal shock is reduced and hence the mould life increases
3. The products quality improves due to lower amount of dissolved gases in the melt which is at a lower temperature.
4. The required energy for the SSM process is lower as compared to the conventional casting processes [35,36].
5. Smooth (near-laminar flow) filling of the die cavity enables casting of complex shape and thin wall products.
6. SSM castings are heat-treatable as compared to the high pressure die casting products.

7. Fine grain size with non-dendritic microstructure formed in the SSM process improves the mechanical properties of the alloys.

Although many scientist and companies, globally have spent a lot of their time and money to investigate in SSM state during the last three decades, there has only been one successful commercial SSM process in NRP [11] due to the following disadvantage [35,36]:

1. SSM process requires high capital cost and maintenance cost.
2. There are many difficulties to control the SSM temperature especially with the alloys which have narrow solidification range.
3. There are difficulties to control the SSM casting temperature leading to difficulties controlling the homogeneity of the solid fraction in the SSM slug.

A non- dendritic microstructure (especially the globular one) formed in SSM casting strongly improves the mechanical properties of the products. It enhances the feeding of the final solidifying liquid and hence, the hot tearing extensively mitigated [35,37,38]. Further, the finer non dendritic grains leads to better machinability, better surface finish, higher toughness and better castability when compared to conventional casting routes [39,40].

4.2.1 Thixocasting/Thixoforming

The process is called thixoforming when an open die is used to make the product, while it is called thixocasting when the product is made by a closed die [4]. Since, we are dealing with closed die processes in shaped casting, we shall, henceforth, only address thixocasting. The thixocasting process was designed to make either a slurry or mush with a fine grain morphology. The main steps in the thixocasting process are illustrated bellow:

1. *Making a billet having a medium or fine grain size*: in this step, the molten alloy is heated a few degrees above the respective liquidus temperature and cast as billets by a direct-chill (DC) casting process into a permanent mould. There are different techniques can be used to make billets having fine grains. These techniques were illustrated below.
    A. *Cooling slope (CS)*: An Inclined plate shown in the Figure 4-17(a) is used to facilitate copious nucleation events coupled with forced convection during making the billet from the molten alloy. The main parameters by which the grain size can be controlled are the superheat of the molten alloy, plate temperature, plate length and plate slope [41,42,43]. Figure 4-17(b) shows fine non-dendritic grains of Al A357 alloy formed in the billet by the cooling slope process whereas bigger dendritic grains shown in the Figure 4-17(c) form in conventional casting process.

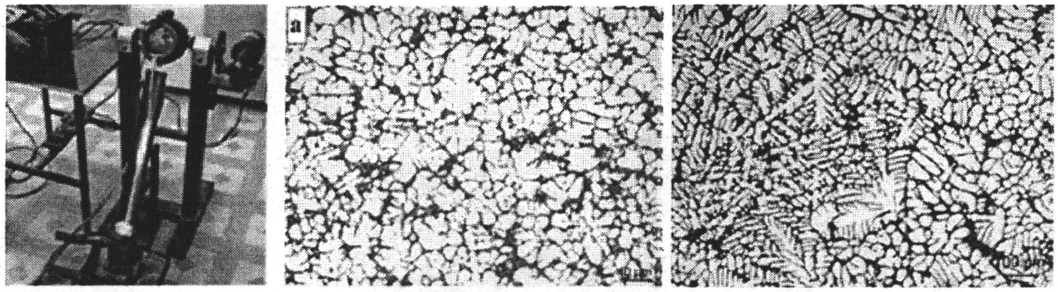

(a) (b) (c)

Figure 4-17 Cooling slope process and microstructure for Al A357 alloy to make thixocasting billets. (a) Cooling slope process, (b) typical microstructure of A357 Aluminum alloy from the process in (a) and (c) typical microstructure of A357 alloy from conventional casting ingots [41].

B. *Lowering superheat of molten alloy*: the molten alloy is heated a few degrees above its respective liquidus temperature and directly poured into an ingot mould. The superheat between (8-10)°C was reported to be sufficient to form refined equiaxed grains of the primary phase [44].

C. *Grains Pre-Deformation*: the molten alloy is poured directly into a permanent mould to make a billet which is then preheated to between 200°C to 280°C and a compression load is applied to deform the grains morphology. The deformation ratio depends on the difference between the billet height before deformation (H0) to that after deformation (H) as indicated in Figure 4-18 [45,46 ,47 ,48 ,49 ,50].

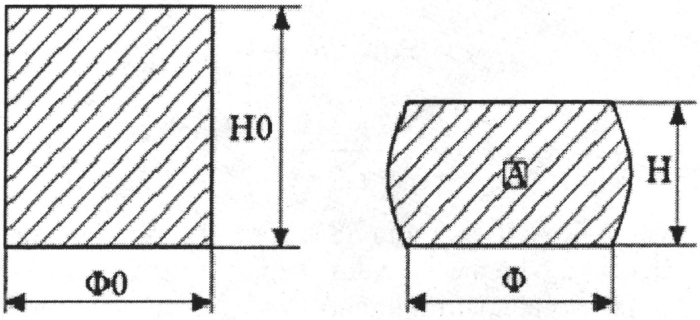

Figure 4-18 Pre-Deformation of a billet to decrease the grain size of the primary phase [46].

D. *Grain Refining (GR)*: Ti and B elements are usually added to the Al alloys to refine the grain morphology in the melt during the solidification process [51]. In SSM thixocasting processes, the Sr is added as a modifier in addition to the Ti and B to improve the rheological properties of Al-Si alloys. Nafisi et al[52] have investigated the effect of added Ti and B as well as Sr for A356 Aluminum alloy in the semisolid state. The apparent viscosity of a Sr treated alloy was lowest compared to the non-treated alloy, further, the surface tension was reduced due to add the Sr leading to improved deformability of the slurry. Jun Du et al[53] added 0.2wt%C and 0.5wt% Sr to refine the grains morphology of Mg-3%Al alloy. Figure 4-19 (a), (b) and (c) show that the grain size of the alloy was reduced by adding C alone and further reduced by added a combination of C and Sr.

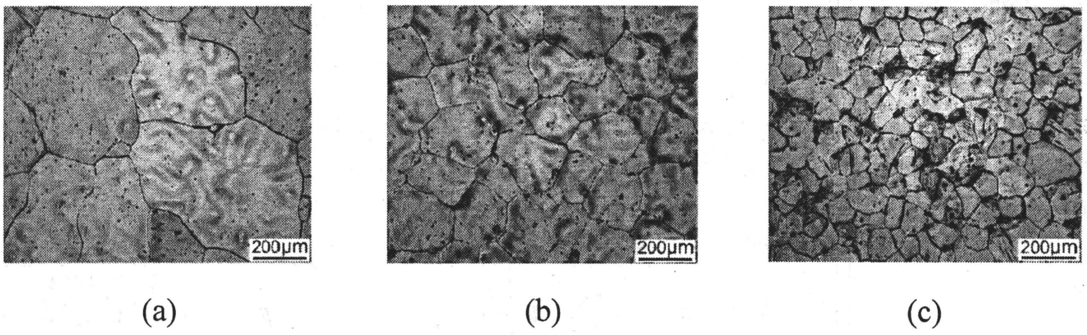

(a) (b) (c)

Figure 4-19 Typical microstructure of Mg-3Al alloy a) without any additional elements, b) addition of 0.2%C and c) with addition of 0.2%C and 0.5% Sr [53].

2. *Reheating the billet*: the billet is reheated to the required SSM temperature. Equation 4-2 (modified Scheil equation [54]) can be used to predict the liquid fraction in SSM state and predicting the required SSM temperature for a specific fraction solid.

Equation 4-2

$$F_L = \left(\frac{T_M - T}{T_M - T_L}\right)^{-1/(1-k)}$$

Where, F_L is the liquid fraction in SSM state, T_M is the melting temperature of the pure metal, T_L is the liquidus temperature for the alloy, T is SSM temperature and k is the partition ratio.

3. *Isothermal holding*: when the billet temperature reaches the SSM temperature, the billet is held isothermally for a precisely chosen time. In this step, the billet is kept inside an induction furnace or immersed in a pre-heated salt bath. In thixocasting process, the grain morphology strongly depends on the isothermal holding time and temperature. The holding time could be anywhere between 10 and 60 minutes depending on the size of the billet. A more globular microstructure can be formed at higher holding times [41-50].
4. *Shaped Casting*: cast the homogenized billet into near net shaped components by a pressure assisted process such as squeeze casting or forging process.

The advantages of the thixoforming process are increased life of the die tool, non-dendritic microstructure, minimized inter-dendritic shrinkage, reduced hot tearing and improved mechanical properties. Further, the ability of the alloy to fill the complex moulds is enhanced [35,55].

On the other hand, the thixocasting process has many disadvantages which have strongly limited the commercial use of this process. The product cost increases due to the multi steps energy intensive process starting from molten alloy to the final cast product. The oxidation of the billet adversely affects the flow characteristics of the alloys, thereby increasing the casting defects and decreasing the quality of the cast product. Further, the isothermal holding time is usually very long making the process less economically favorable [56]. Finally, some liquid would always be entrapped inside the primary grains during the grain growth occurring at the isothermal holding period. Figure 4-20 shows that the amount of the entrapped liquid increases with increasing holding temperatures. The entrapped liquid cannot be compensated from the liquid existing outside the grains. Thus, the inter-dendritic shrinkage takes place inside the growing grains. As a result, the mechanical properties decrease. These disadvantages limit the industrial applications of the thixocasting process [35,56,57].

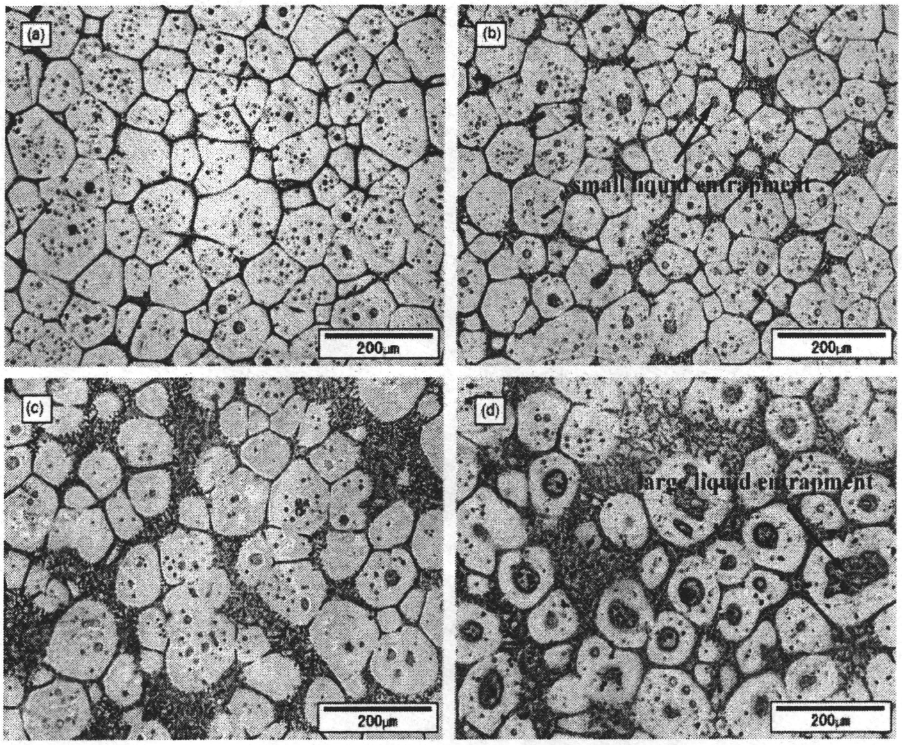

Figure 4-20 Typical microstructure of thixocasting process of AZ91D alloy isothermally hold at (a) 550°C , b) 560°C , c) 570°C and d) 580°C [50].

4.2.2 Rheocasting

To overcome the disadvantages of the thixocasting process, the rheocasting process was innovated as a SSM technique to form non-dendritic microstructure, improve the mechanical properties of the product and reduce the cost by eliminating the extra steps in the thixocasting process [58]. The main steps of the rheocasting process are illustrated below.

1. *Cooling a molten alloy from liquid state to SSM state (slurry)*: copious nucleation of the primary Al phase coupled with a forced convection in the liquid to continuously re-distribute the nuclei in the bulk melt is critical to obtaining a non-dendritic primary phase morphology in the rheocasting process. Maximizing the nucleation rate significantly reduces the size of the grains in the SSM temperature and the final cast product [59,60,61]. Various rheocasting processing routes have been developed to achieve the favorable conditions of copious nucleation of the primary phase coupled with forced convection in the liquid. Figure 4-21 (a) to (d) shows the four of the more popular rheocasting technologies in New Rheocasting Process (NRP), Continuous Rheoconversion Process (CRP), Semi-Solid Rheocasting (SSR) process and Rheo Die-Casting (RDC) process, respectively [62]. To attain copious nucleation coupled with forced convection, in the NRP process, the molten alloy with a low superheat temperature is poured on slant face of a steel crucible, in the CRP process, the molten alloy with a low superheat temperature is poured through a complex copper mould in a reactor, in the SSR process, a copper or graphite rod is dipped in the molten alloy with low superheat and stirred at high speeds, and in the RDC process, the molten alloy with a low superheat is passed through a metallic screw before being collected in the shot sleeve of a high pressure die casting machine [62].

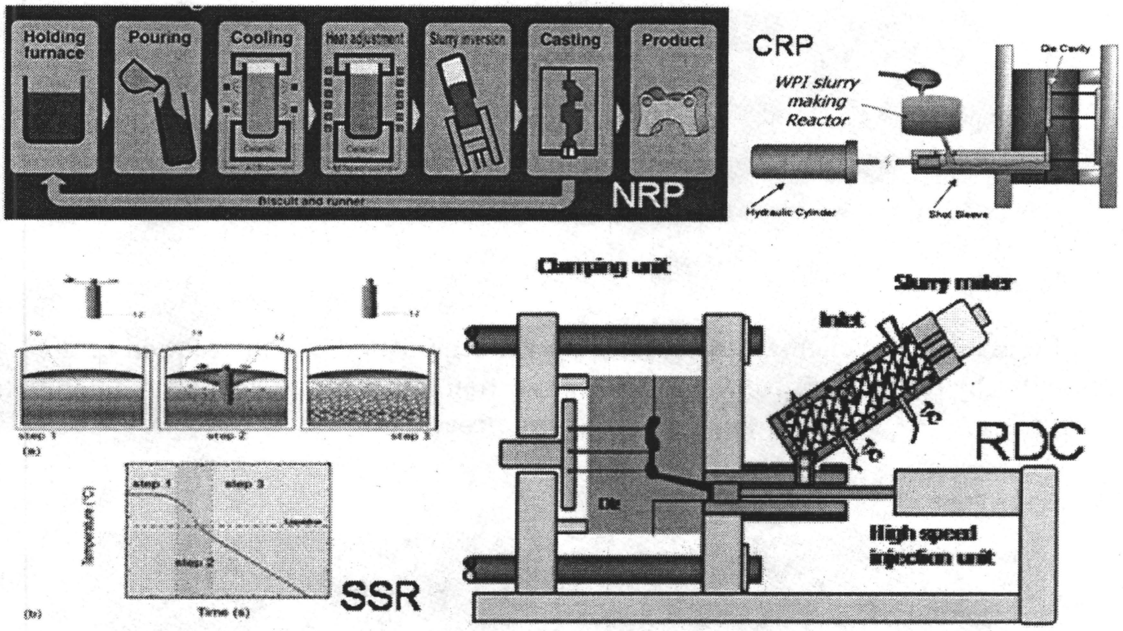

Figure 4-21 Schematic diagram of different rheocasting processes [64].

2. *Dendritic microstructure Fragmentation*: the dendrites initially formed at the heat extraction interface during the nucleation event of a rheocasting process [63, 64, 65, 66, 67, 68, 69, 70, 71, 72, 73, 74, 75, 76, 77, 78, 79] grow on two locations: the container wall (Crucible) and/or the stirrer as shown in Figure 4-22. The shearing force applied on the slurry during forced convection of the liquid around the dendrites breaks the dendrites. The degree of dendrite fragmentation is directly proportional to the intensity of the forced convection. Many techniques have been innovated to improve the intensity of the forced convection of the liquid and increase dendrite fragmentation. Figure 4-23 (a), (b), (c) and (d) show some of the popular techniques such as magneto-hydro-dynamic (MHD) or electro-magnetic stirring [35,64,80], mechanical stirring by impeller [35,66,70], mechanical stirring by screw [65,69] and swirling [67], respectively.

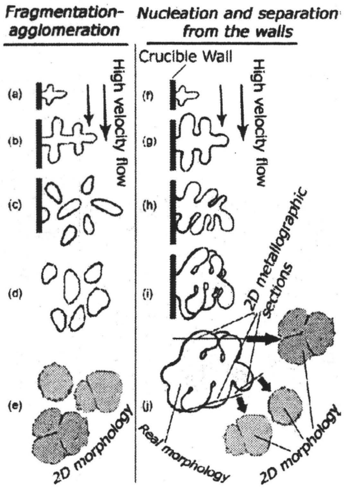

Figure 4-22 Schematic diagram of the mechanism of fragmentation of the dendrites by the intensity of the forced convection of the liquid around the dendrites in the rheocasting process [68]

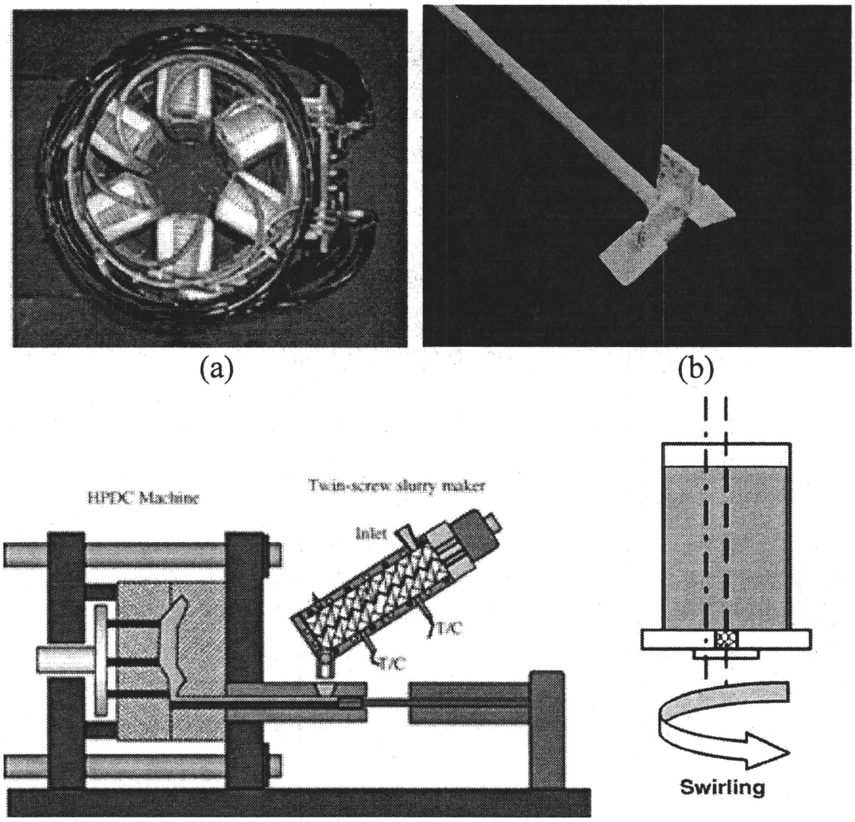

(a) (b)

(c) (d)

Figure 4-23 Some of the popular methods of stirring in the rheocasting process, a) electromagnetic stirrer, b) mechanical stirrer, c) screw slurry maker and d) by swirling.

3. *Shaped Casting*: casting of the slurry into near net shaped components by a pressure assisted casting process such as squeeze casting.

The rheocasting process did not solve all the disadvantages of the thixocasting process and conventional casting processes but it decreases the extra steps in the thixocasting process and enables a non-dendritic microstructure without any entrapped liquid in the primary phase morphology as shown in Figure 4-24.

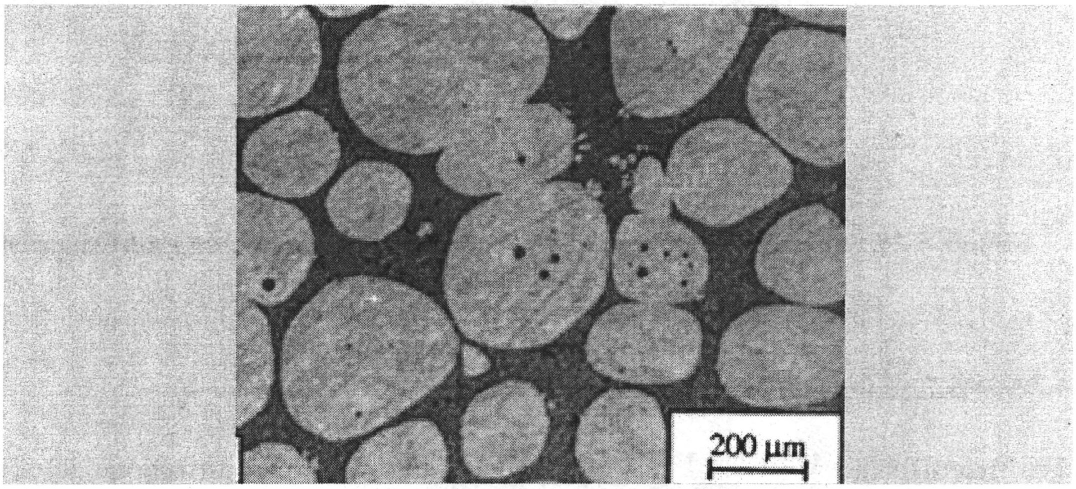

Figure 4-24 Typical microstructure of MHD rheocasting process of A356 Al-Si alloy after 15h of isothermal holding [81].

The disadvantages of rheocasting process are illustrated below.

- There are difficulties in bringing the molten alloy to the desirable SSM temperature in a short time and controlled manner.
- The stirrer need special treatment to prevent the erosion by molten Al alloy and inclusion of erosion products into the alloy melt and casting. The surface treatments to maintain the stirrer surface and mitigate erosion are cost intensive [35].
- Both rheocasting and thixocasting processes are more complicated than the conventional casting. Figure 4-25 is a schematic diagram showing the multi steps in these two processes.

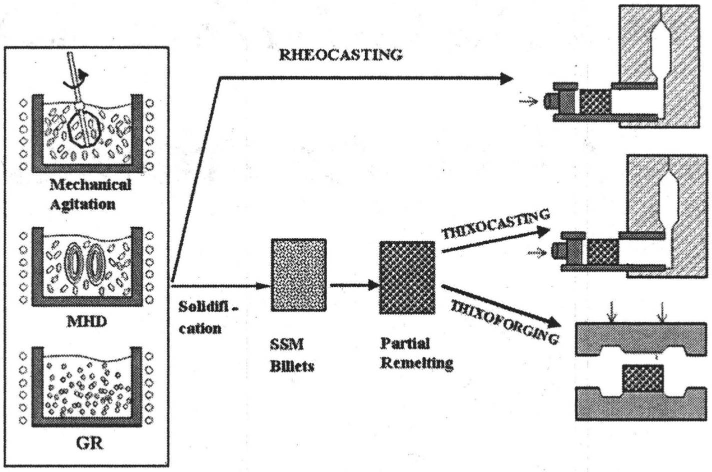

Figure 4-25 Schematic diagram of the steps in the rheocasting and thixocasting processes. [55].

4.3. CONVECTIVE CELLS AND CONVECTIVE FLOW

The first step in the CDS process is mixing of the two precursor alloys with different thermal masses to enable copious nucleation coupled with forced convection in the resultant mixture. Hence, a comprehensive literature review was carried out to understand the prior art in the mixing of two liquids.

Okubo et al [82] mixed black tea with cream in a plain pan (two different densities). Convectional patterns were formed from irregular circulation when they exposed the bottom pan to a heat source. After a while, hexagonal Bernard cells formed between the tea and the cream that formed plate-like colloidal particles inside the tea. Three interdependent factors were identified as mandatory for the formation of these Bernard cells: difference in temperature, difference in surface tension and convective flow in the mixture [82].

Further, when a thin layer of a fluid is enclosed between two horizontal surfaces which are at different temperature, the lower surface at higher temperature, the natural convection in the enclosure caused by the density gradient between the bottom and top surfaces would result in the formation of the Benard cells in the fluid as shown in Figure 4-26 [83-84-85].

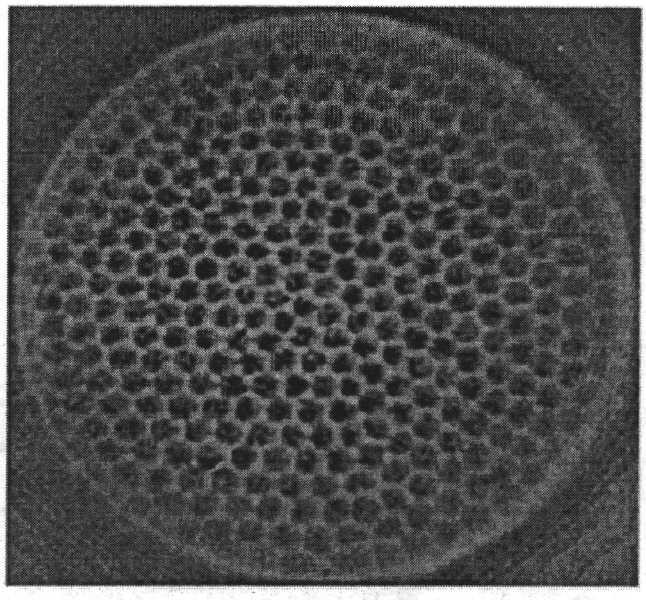

Figure 4-26 Hexagonal Benard cell [84]

As would be presented in the results section of this dissertation, cells similar to Bernard cells were obtained at the end of mixing and prior to solidification in the CDS process. Further, these cells were in the order of micrometers in dimension. Hence, a literature review was carried out to understand the transport phenomena in the micrometer dimensions.

The analysis of heat transferred in micro-scale dimension has been a popular topic of research in the last twenty five years and it has been found that the transport phenomena laws are different in the micro-scale dimensions as compared to the conventional macro-scale.[86]. The surface to volume ratio increases when the length scale decreases; thus, the parameters related to surface area such as surface roughness begin to play a more dominant role in determining the flow of mass, momentum and heat in the micro-scale dimensions. For example, the limitation of Reynolds number in the laminar-turbulence transition zone in conventional flow is between 1000 to 3000 while it was less than 650 in tube of diameter between 50 to 254 μm [87,88]. Stephan et al [89] have evaluate theoretically and experimentally the heat and mass transfer phenomena of nucleate boiling in microscale and macroscale dimensions of pure material and mixture. They found that the mass transfer is significantly affected by capillarity forces in the micro-scale. The concentration of the mixture also changes the nucleate boiling point and that strongly changes the diffusivity of heat. Nishimura et al [90] had studied the mixing of two layer of salt forming a stratified system (the difference in concentration between 0.2-0.8 wt%) in rectangular enclosure made of 15 mm thickness of an acrylic resin placed between two lateral Cu plates (5mm thickness each) and one of them being exposed to a higher temperature than the other. After 3s, a boundary layer and shear flow separated by interface were clearly observed between the hot and cold Cu plates. The interface started to tilt as the time progressed because of the horizontal temperature gradient. Figure 4-27

(b) and (c) clearly shows the stream of the convective flow between the layers. The results shown in Figure 4-28(a) and (b) indicate the following:

- The mixing time increases as the size of enclosure increases.
- The mixing time increases as the concentration between the layers increases.
- The mixing time decreases as the temperature difference between the hot plate and the cold plate increases.

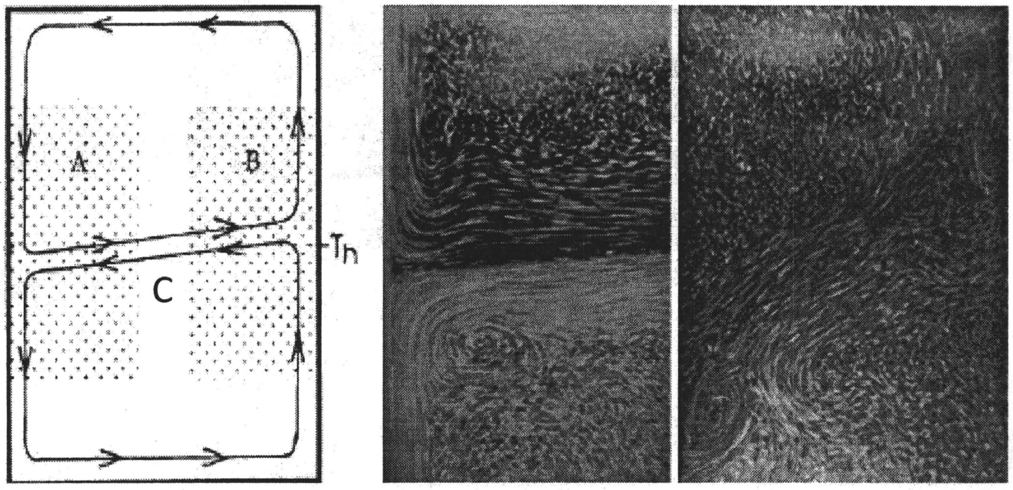

(a) (b) (c)

Figure 4-27 Flow stream of salt layers (a) a schematic diagram shows the location of the images, (b) image representing area A of colder copper plate after 74 min and (c) image representing area C after 120 s [90].

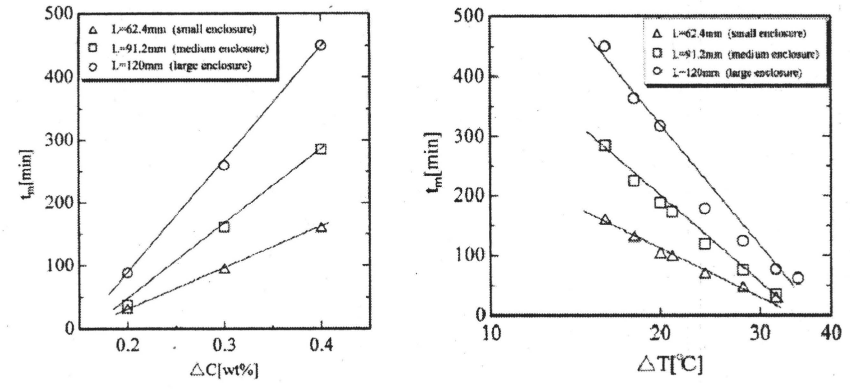

(a) (b)

Figure 4-28 Experimental data of mixing time with(a) different in salt concentration and b) temperature difference between the two copper plate [90].

Tanny et al [91] had experimentally investigated the effect of layer depth ratio on mixing of aqueous salt (NaCl) with water forming stratified flow when contained between two lateral stainless steel walls with a specific temperature difference. A convective flow was induced due to the temperature difference across the interface of the layers leading to the formation of vortices between the two layers as shown in Figure 4-29. The formation of vortices accelerated the mixing process. The deduced result shows that when one layer is deeper than the other, the mixing time was reduced.

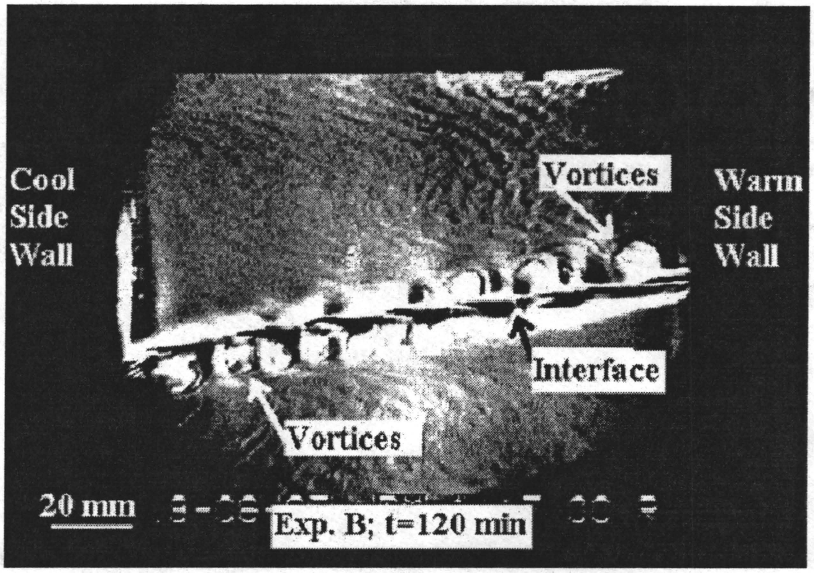

Figure 4-29 Typical image of stratified flow between aqueous salt (NaCl) and water shows the vortices at interface taking place by convection[91].

Lamsaadi et al [92] Have studied the effect of non-Newtonian behavior of fluids on the characteristics of heat transfer and fluid flow. They had solved the Navier-stocks equations, continuity equation and heat equation theoretically and numerically to predict the temperature and velocity distribution in a fluid moving as laminar flow due to natural convective. The fluid was placed in a rectangular box insulated from upper and lower sides and exposed to uniform heat flux from other lateral sides. The results show that the heat transfer and fluid flow characteristics are sensitive to non-Newtonian power index (n). The transport phenomena is significantly different for fluids with $0 < n < 1$ (shear thinning) when compared to $n=1$ (Newtonian) and to $n>1$ (shear thickening). The intensity of the flow and vortices would be the highest for shear thinning fluids, followed by that for Newtonian and minimum for the shear thickening fluids.

In the CDS process, during mixing, we have a situation where an alloy with a higher thermal mass (temperature and mass) is mixing with that of a lower thermal mass. The literature review shows that the process of mixing would be controlled by the difference in the two initial thermal masses which would determine the level of convection, time of mixing and type of mixing (vortices and Bernard cells). Further, it was recently proposed [93] that liquid metals and alloys exhibit a non-Newtonian flow behavior with a shear thinning characteristics which would further enhance the intensity of the convection currents, turbulence and vortices during mixing in the CDS process.

4.4. SOLIDIFICATION OF ALLOYS

The literature on the stability criteria for the S/L interface of growing nucleus for pure materials and alloys were reviewed and presented in this section.

4.4.1 Stability Criteria for Solidifying Interface

The interface stability was initially analyzed by Rutter and Chalmers [94] and they developed the basic criteria presented in Equation 4-3 for the stability of the S/L interface during growth. The extent of constitutional undercooling ahead of the solid liquid interface during growth was used to evaluate the stability of the interface.

Equation 4-3

$$\frac{G_L}{V} \geq -\frac{mC_L\ (1-k)}{D_L} \qquad (Stability)$$

Mullins and Sekerka [95] expanded the older criterion by introducing infinitely small sinusoidal perturbation into the morphology of the planer interface. The modified criterion was called Mullins and Sekerka criterion (MS) and it depended on the dynamic movement of the sinusoidal amplitude assumed in planer solid liquid interface. The interface was deemed unstable if any of these sinusoidal perturbations grew and was deemed stable if none of the perturbation grew. The comprehensive expression to quantify the perturbation of the solid-liquid interface during solidification of pure metal and binary metallic alloys was proposed as presented in Equation 4-4 (a) by [95]; and the terms In Equation 4-4 (a) are described in Equation 4-4 (b) to (f).

Equation 4-4

$$\frac{1}{\delta}\frac{d\delta}{dt} = \frac{V\omega\left[-2T_m\Gamma\omega^2\{\omega^*-(V/D)P\}-\left(G'+G\right)\{\omega^*-(V/D)P\}+2mG_c\{\omega^*-(V/D)\}\right]}{(G'-G)\{\omega^*-(V/D)P\}+2\omega mG_c} \qquad \text{(a)}$$

$$\omega^* = (V/2D) + [(V/2D)^2 + \omega^2]^{\frac{1}{2}} \qquad \text{(b)}$$

$$G' = (K_s/K')G_s \qquad \text{(c)}$$

$$G = (K_L/K')G_L \qquad \text{(d)}$$

$K' = \frac{1}{2}(K_s + K_L)$ (e)

P=1-k (f)

Equation 4-5 presents a simplified version of Equation 4-4 (a) as applied to solidification of pure metals.

Equation 4-5

$$\frac{1}{\delta}\frac{d\delta}{dt} = \frac{(K_S+K_L)}{L_v}\omega\left[-T_M\Gamma\omega^2 - \frac{K_SG_S+K_LG_L}{K_S+K_L}\right]$$

There were certain critical assumptions presented in proposing Equation 4-4 (a):

1. Local equilibrium at the S/L interface.
2. Isotropy in bulk and interface surface parameters.
3. Steady state of the thermal-solutal field. The solute transfer in the liquid ahead of the S/L interface is purely by diffusion. The boundary condition of the solute concentration in the liquid ahead and adjacent to the S/L interface are (C_∞/k) at the S/L interface and C_∞ past the diffuse boundary ahead of the S/L interface as determined by D_L/V.

The above assumptions have severely limited the validation of the Equation 4-4 (a) by experiment data from solidification of metals, specifically due to the lack of a purely steady state solidification scenario in experiments. Further, at the end of the solidification, the amplitude of the sinusoidal becomes bigger as it was quantified experimentally by Mullins and Sekerka [95]. Based on the above-mentioned assumptions, certain specific criteria were developed from the expression in Equation 4-4 (a) to evaluate the stability of the solid-liquid interface during solidification. These criteria were based on the values of the parameters such as thermal gradient, solute gradient, capillarity effect and the latent heat of fusion. The criteria are presented in Equation 4-6 to Equation 4-9.

Equation 4-6 represents the instability criterion during the growth of a single component material (pure) during solidification. The criterion depends on the thermal gradient at the S/L interface wherein the interface could be unstable when it is growing into an undercooled liquid with a negative G_L.

Equation 4-6

$$G^* = \frac{K_SG_S + K_LG_L}{K_S + K_L} < 0 \quad (instability)$$

The criterion shown in Equation 4-7 indicates the effect of the capillarity coupled with thermal gradient on the instability of S/L interface. The term, ($T_M\Gamma$) is always positive and hence, the Equation 4-7 depends only on the thermal gradient existing in the solid and in the liquid to define G*, as shown in Equation 4-6 [96]. In Equation 4-7, ω_{oo} represents the frequency at which $\frac{1}{\delta}\frac{d\delta}{dt} = 0$, as defined in Equation 4-4 (a). Figure 4-30 shows a schematic of the inequality in Equation 4-7; wherein the S/L interface is stable for all cases when $\frac{1}{\delta}\frac{d\delta}{dt} < 0$, and when $\frac{1}{\delta}\frac{d\delta}{dt} > 0$, ω_{oo} would exist and the interface instability is governed by Equation 4-7. In Figure 4-30, the S/L interface in the solidification case shown by *a* is always stable and that shown by *b* is stable only when $\omega > \omega_{oo}$. Further, for the case *b* in Figure 4-30, the maximum amplitude rate during an unstable growth occurs at the maximum frequency (ω_o) which is equals to $\left(\frac{\omega_{oo}}{\sqrt{3}}\right)$ [96]. Ogasawara et al [97] had investigated the effect of the curvature of the S/L interface on its instability and found that when the curvature increases, the temperature gradient in the liquid increases thereby decreasing the growth rate under a positive temperature gradient resulting in a more stable S/L interface. As a result, according to Equation 4-7, the solid liquid interface for pure metals in unidirectional solidification is always stable due to positive thermal gradient in the liquid and hence G*>0 whereas for cases when the solidification is not uni-direction, the S/L interface of equiaxed grains would always be unstable and grow as dendrites due to the negative thermal gradient ahead of S/L interface and hence, G*<0.

Equation 4-7

$$0 \leq \omega \leq \omega_{oo} = \left[\frac{-G^*}{T_M\Gamma}\right]^{1/2} \qquad (instability)$$

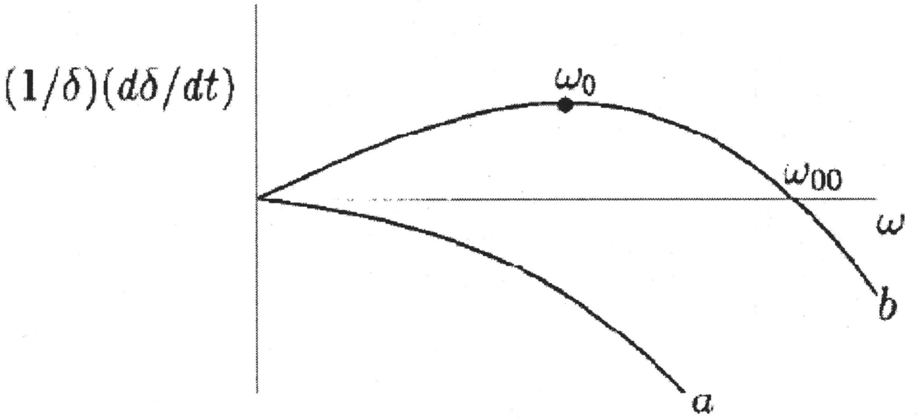

Figure 4-30 Amplitude growth rate as a function of frequency for two cases, a) stable and b) unstable.[96]

The S/L interface instability for a binary alloy solidification is shown in Equation 4-8 which is also called the modified constitutional undercooling criterion that is dependent on the thermal gradient in the solid and liquid in addition to the solute gradient in the liquid. In Equation 4-8, the term in the right hand side of the inequality represents the constitutional undercooling ahead of the growing S/L interface and the term could also be represented as ($-m_L G_c$), where G_c is the solute gradient ahead of the growing S/L interface. The criterion for pure metal solidification, in Equation 4-7 was modified by neglecting the capillarity effects and adding the effect of constitutional undercooling to obtain Equation 4-8. By Equation 4-8, the S/L interface could be unstable even for a positive value of thermal gradient in the liquid [96,98,99,100].

Equation 4-8

$$\frac{K_S G_S + K_L G_L}{K_s + K_L} \leq -\frac{m_L C_\infty \ (1-k)V}{D_L \ k} \qquad (instability)$$

Equation 4-9 was derived from Equation 4-8 to include the latent heat of fusion evolved at the S/L interface during solidification; specifically, by replacing the term ($K_s G_s$) by ($HV+K_L G_L$) from the heat balance at the S/L interface and neglecting the effect of thermal gradient in the solid; leading to the instability criteria for the S/L interface in binary alloy, presented in Equation 4-9.

Equation 4-9

$$\frac{G_L}{V} < -\frac{H}{2K_L} + \left(\frac{K_S + K_L}{2K_L}\right)\frac{m_L C_\infty \ (k-1)}{D_L \ k} \qquad (instability)$$

Equation 4-9 is the simplified instability criterion for the S/L interface in a binary alloy solidification condition as derived from Equation 4-4 (a). When, according to Equation 4-9, the interface instability condition is satisfied, Equation 4-4 (a) would be used to characterize the unstable interface with perturbations. Although, Equation 4-9 and Equation 4-4 (a) are for a steady state solidification condition and that solidification experiments of binary alloys are seldom steady state, we currently do not have an alternate instability theory to utilize and these equations are our best resource to predict stability of the S/L interface.

The solute boundary layer ahead of S/L interface was theoretically evaluated and quantified experimentally by Holmes and Catos [101]. The result indicates that the experimental data was ten orders of magnitude larger than the theoretical evaluation. This difference was mainly due to the steady state assumption in the theoretical evaluations and the lack of it in the experiments.

Mullins and Sekerka[102] had deduced that the growing sphere could grow stably when the sphere radius is less than the value of a critical radius which is seven times the critical radius (r*) derived in the theory of nucleation shown in Equation 4-10.

Equation 4-10

$$r^* = \frac{2\,\gamma_{sl}T_m}{L_v\Delta T}$$

The stability of non-dendritic microstructure exposed to a shear stress caused by stirring was studied by many investigators. Das et al [26] had simulated the solidification of the inter-dendritic structure under forced fluid flow which was turbulent at high applied shear rates. They found that when the turbulent flow penetrates the inter-dendritic region, the solute ahead of the S/L interface is moved into the bulk liquid thus reducing the extent of constitutional undercooling ahead of the interface, as shown in Figure 4-31. This condition would lead to the growth of a more stable S/L interface [26]. In rheocasting, the intensity of the forced convection in the liquid during solidification is critical to the stability of the S/L interface and obtaining a non-dendritic morphology of the primary phase.

Dhindaw et al [103] had studied the effect of the shear rate and the solute redistribution on the stability of S/L interface by casting Al-6.2% Cu alloy and Al-7.3% Si alloy in rheocasting process. They found that the microstructure changes to rosettes and spheroid when they had applied low shear rate. Further, the stirring step significantly increases the solid fraction due to fragmentation of the dendrites morphology during rheocasting steps.

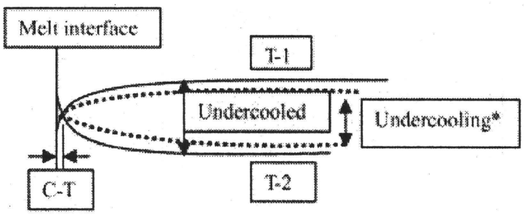

T-2 is the melt temperature profile

T-1 is the liquidus profile

C-T is the stagnant layer next to the solid tip

Undercooling* = Because of shearing

Figure 4-31 Schematic diagram of constitutional undercooling in rheocasting and conventional casting [103]

Martinez et al [104] had numerically solved the diffusion equation for a growing spherical phase particle in the rheocasting process and compared the numerical results with experimental data for the solidification of the Al-4.5wt% Cu alloy. The amplitude rate equation of linear perturbation on an initial flat and stable S/L interface had been derived and the results show that the amplitude rate increases with increasing growth rate (V) and decreasing curvature of the S/L interface as shown in Equation 4-11. Further, the effect of the cooling rate and solid fraction on the stability of the growing phase had been studied. Figure 4-32 show that the higher cooling rate will break down the planer S/L interface leading to an unstable growth. Accordingly, a higher solid fraction with lower cooling rate would be favored for a stable growth. The typical microstructures shown in Figure 4-33 (a) and (b) confirm the results in which the low cooling rate of 1.1 °C/s leads to a stable S/L interface, whereas, increasing the cooling rate to 2.8 °C/s led to the breakdown of a planer S/L interface. The investigators had deduced that, in SSM processes, high density of nuclei, higher solid fraction and low cooling rate are favorable for stable growth of the S/L interface leading to a non-dendritic microstructure.

Equation 4-11

$$\frac{d\delta}{dt} = V\omega - \frac{D_L \Gamma}{mC_o(k-1)}\omega^3$$

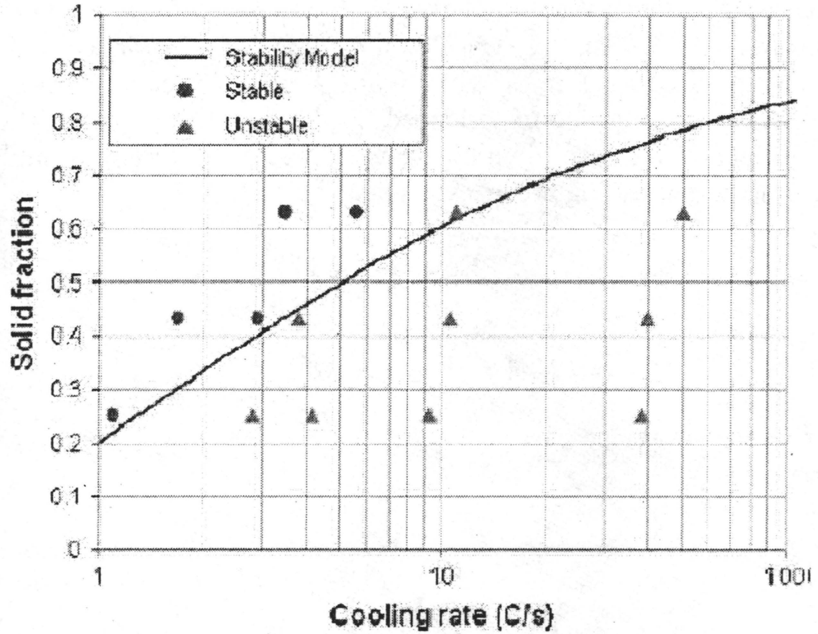

Figure 4-32 Comparison between experimental data and calculated data for rheocasting process of Al-4.5wt% Cu.[104]

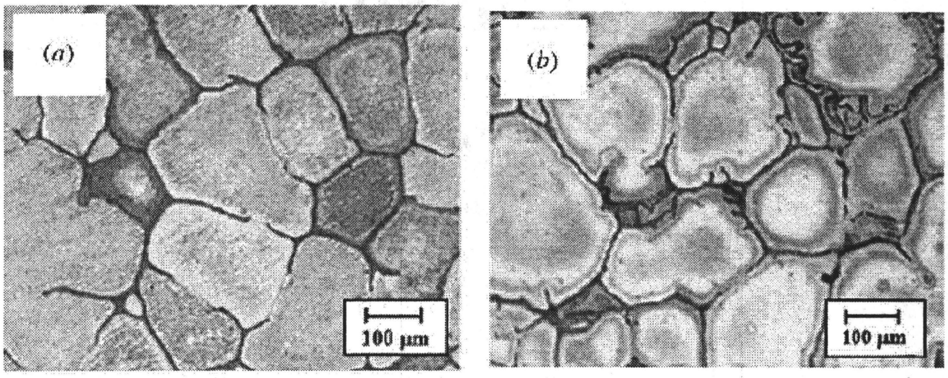

(a) (b)

Figure 4-33 Microstructure of Al-4.5wt% Cu alloy reheated to 0.25 solid fraction and cast by rheocasting process at a) 1.1 °C/s and b) 2.8 °C/s [104].

Equation 4-12 represents a new criterion proposed by Qian [105] to predict a critical radius (R_c) up to which a phase particle in a rheocasting process would grow with a stable interface. This criterion shows that the critical radius, R_c of growing nucleus morphology is much bigger than that in conventional casting ($R_c = 7r^*$). The R_c is very sensitive to the alloy undercooling ($\Delta T = T_m - T_\infty$) as shown in Figure 4-34. Equation 4-12 was proposed by using the Mg-3.8wt% Zn-2.2wt% Ca alloy with 2.5wt% Zr as a grain refiner and solidified at various cooling rates. In Figure 4-34, the undercooling, ΔT is directly proportional to the cooling rate experienced by the liquid during solidification. Hence, lower cooling rates would result in a higher value of R_C, leading to a stable S/L interface for a longer time period during the growth stage.

Equation 4-12

$$R_c = (7 + 4\frac{k_S}{k_L})r^*$$

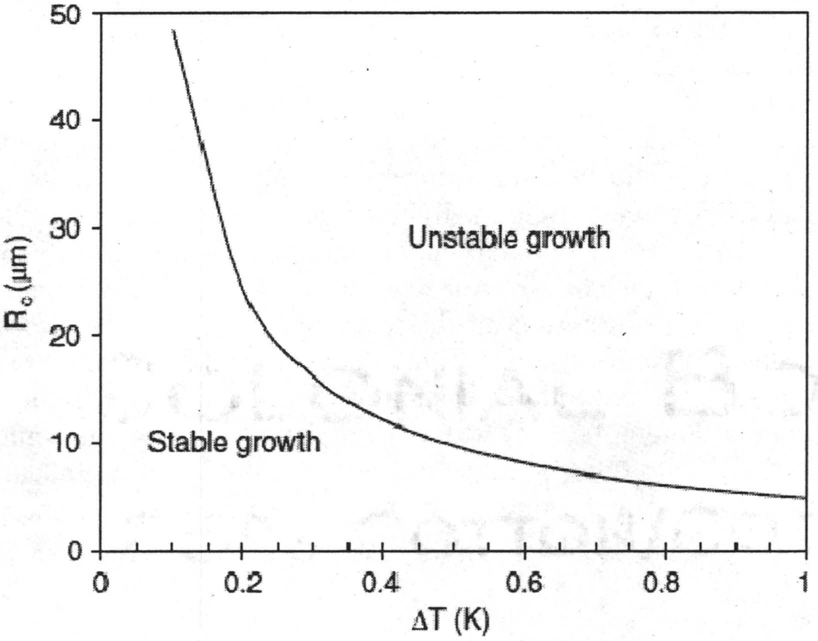

Figure 4-34 Critical radius for spherical growth in SME state of Magnesium alloy as a function of undercooling [105].

Hitchcock et al [106] proposed Equation 4-13 by modifying Equation 4-12 to evaluate the R_c for Al alloys. The theoretical evaluation of R_c had been compared the experimental data from rheocasting of the Al–7Si–0.6Mg alloy. The results indicate that the theoretical value of R_c evaluated by Equation 4-13 was between 5.12- 10.24 μm in diameter for a range of undercooling between (1-2 K) whereas the average measured diameter in experiments was 7.8 μm . The criterion shows a good agreement between the theoretical and experiment data.

Equation 4-13

$$R_c = \frac{5.12}{\Delta T} \quad (\mu m)$$

The literature review has shown that a low cooling rate coupled with either a longer isothermal holding time (thixocasting) or a short holding time with high agitation (stirring) (rheocasting) would enable the thermal solute to redistribute and reduce ahead of the S/L interface and enable the growth of a stable and unperturbed interface leading to a non-dendritic morphology.

The stability of the S/L interface during growth in the CDS process was observed by Symeonidis [13] and a schematic for the thermo-solutal fields ahead of the growing S/L interface was presented as shown in Figure 4-35 (b). The thermo-solutal conditions ahead of the S/L interface in a conventional casting are shown in Figure 4-35 (a). The solute distribution in Figure 4-35 (b) suggests that contrary to the solidification in a conventional casting process, the solute diffusion is towards the S/L interface in the CDS process during solidification; as also proposed by Khalaf et al [29,30]. However, the nature of the curve for solute distribution hypothesized in Figure 4-35 (b) was found to be erroneous from the experimental and theoretical analysis in presented in the results of this dissertation. Figure 4-35, show that the constitutional undercooling ahead of S/L interface in the CDS process was much less compared to that in the conventional casting process, leading to a stable interface in the former process. Figure 4-36 (a), (b) and (c) show that a globular microstructure could form in the CDS process at low superheat of Alloy1 and it gradually becomes more dendritic at higher superheat temperatures. The nature of results shown in Figure 4-36 was also proposed by Khalaf et al [30].

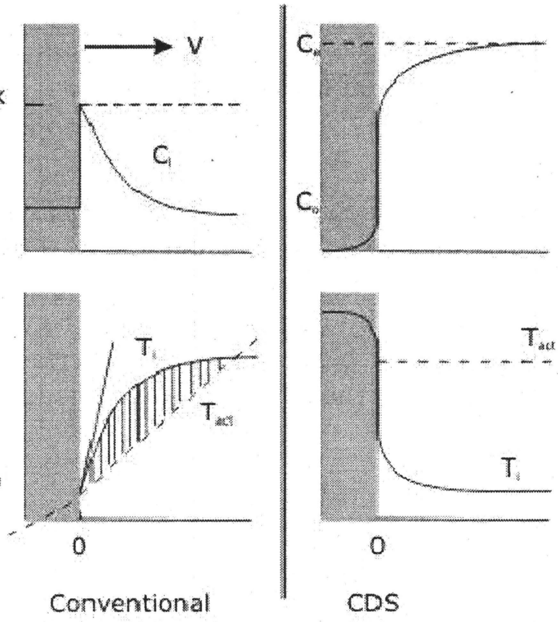

(a) (b)

Figure 4-35 Comparison of the temperature and solute distribution ahead of S/L interface for (a) conventional casting and (b) CDS [13].

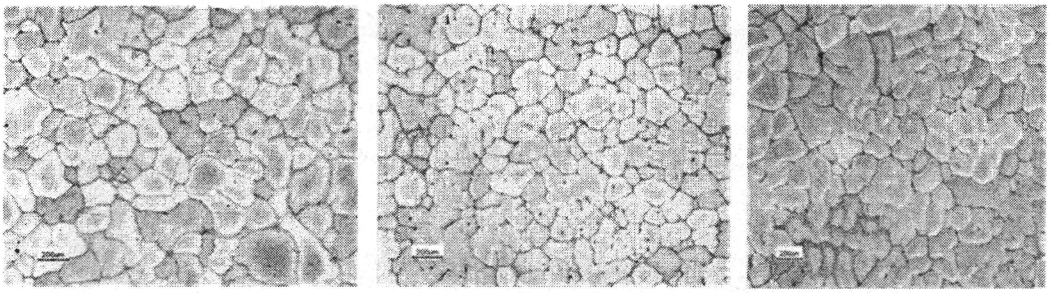

(a) (b) (c)

Figure 4-36 Microstructure changing from Non-dendritic to dendritic obtained by CDS process of Al Cu system under different superheat, a) 2°C (non-dendritic), b) 12°C (non-dendritic) and c) 22°C (dendritic) [13].

The extensive review of the prior-art has enable the identification of the missing information in the science of the CDS process, specifically the in-depth understanding of the various events in the various stages of the CDS process starting from the mixing of the two alloys to the final solidification, and the identification, quantification and optimization of the critical process and alloy parameters to effect a successful CDS process with a non-dendritic morphology of the primary Al phase in the solidified microstructure.

CHAPTER 5. EXPERIMENTS AND ANALYSIS PROCEDURES

In this chapter the laboratory and numerical experiments carried out in this study along with the methodology of the data analyses are presented in the following sub-section:

- Laboratory CDS experiments
- Interrupted quenched experiments.
- Numerical simulation experiments.
- Organics alloys system experiments.
- Microstructure analysis

5.1. LABORATORY CDS EXPERIMENTS

Controlled experiments in the laboratory were carried out to elucidate the details of the events in the various stages of the CDS process: *mixing of the two alloys, homogenization of the thermal and solute fields and solidification.* A variety of liquids such as water, milk, organic alloys and Al alloys were used in these experiments in various capacities. Each experiment was precisely designed and set up to explore, understand and verify the specific events occurring in each step of the CDS process.

5.1.1 Water-Water and Water–milk systems

The CDS starts with the mixing of two precursor alloys of different thermal masses to enable a favorable environment for copious nucleation of the primary solidifying phase and forced convection in the mixture. To better understand and visualize the mixing process between two liquids water (transparent) was used along with water and milk. The temperature and mass of the two mixing fluids were maintained as different both independently and together to better understand the controlling parameters for an efficient mixing process. The dependent parameter in these experiments was the visual interpretation of the mixing process.

5.1.1.1 Water-Water mixing

In these experiments, two thermal mass of water were taken in clean beakers and mixed together by directly pouring one of the liquid into the other and by pouring the same with the funnel wherein the mixing was initiated from the bottom of the lower thermal mass fluid. The experiments were repeated such that the higher thermal mass was poured into the lower and vice-versa using a funnel to maintain nearly the same mixing rate among experiments. To enable better visualize of the flow stream of the liquid with the higher thermal mass, a blue ink was added to the same. The objective of these experiments is to visualize the mixing processes and optimize the same for minimum bubble formation and expeditious equalization of the thermal and solute fields in the resultant mixture after the mixing process. The formation of bubbles during mixing would have to be minimized because in metallic Al alloy systems bubble would induce defects in the mixture such as oxides and dissolved hydrogen which are detrimental to the final cast product. 150ml of warm water (~40-45°C) was mixed with 25ml of water at room temperature (~18-20°C). A video camera is used to take a digital video of the mixing process and time dependent image snap shots were extracted from this video. The mass ratio between the liquids was maintained at six.

Figure 5-1 shows the schematic of the experiment setup. There were k-type four thermocouples (Ch1 to Ch4) in the experiments such that one thermocouple was in the liquid which was poured and there were three in that which received the pour to quantify the thermal field homogenization process during mixing. The experiments were repeated several times with and without the thermocouples to understand the repeatability of the process. In Figure 5-1, Ch1, Ch2 and Ch3 were installed in the container which received the pour at the depths of 8, 24 and 56mm from the bottom of the container, respectively; such that at least Ch1 was already in the liquid while the others could initially be in air.

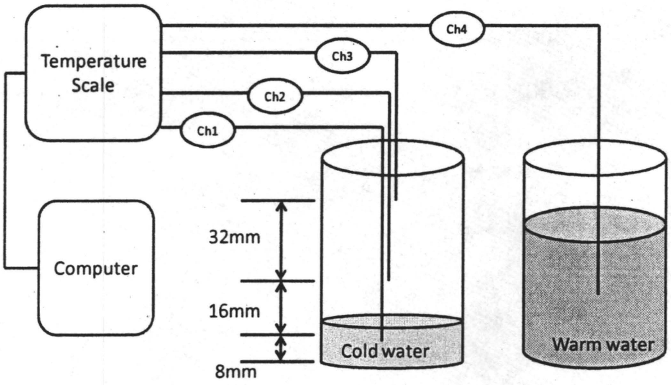

Figure 5-1: A typical schematic diagram for water-water experiments where the warm water was poured into the cold one. The beakers would be interchanged in experiments were the cold water was poured into the warm one.

5.1.1.2 Water- Milk Mixing

In the experiments with water-water mixture, the density difference between the two thermal masses was marginal and to accentuate the effect of a significant density difference between the two fluids, experiments were carried out with water and milk. Further, the results from the previous experiments as presented in the next chapter of this dissertation showed that the use of a funnel presented a more favorable mixing process. Hence, 150ml of warm water (40°C) was poured through the funnel into 25ml of cold milk (~15°C) and vice versa. The mass ratio of the two liquids was maintained at 5.8 such that the water was the higher mass.

5.1.2 *Al-Cu Alloy System*

In this study, Al-Cu system was chosen as the metallic alloy system to study the various events in the CDS process for reasons illustrated bellow:

- The solidification of this alloy system by all of conventional, SSM and CDS processes is well researched and documented [107, 108 ,19]
- The system presents a favorable temperature and compositional range of liquidus temperature such as from 660 °C for pure Al to 547 °C for the Al-33wt%Cu eutectic composition; and this enables the flexibility to choose a variety of compositions with significant difference in liquidus temperatures in the hypoeutectic alloy regime.
- The system were widely used in domestic and industrial application especially the most of 2xxx Al wrought alloys have the Al-4.5wt% Cu alloy as the basic composition. Further, these alloys have a wide range of mechanical property for various heat treatment temper conditions.

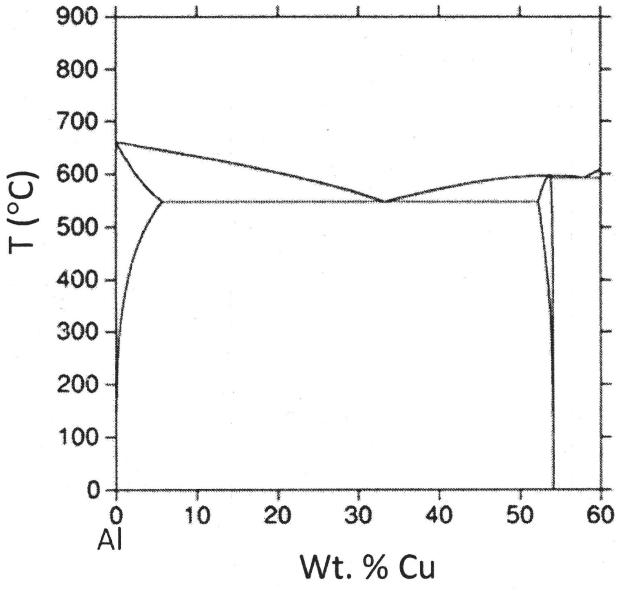

Figure 5-2: Binary phase diagram of Al-Cu alloys system with Al-33wt%Cu as the eutectic composition and 547 °C as the eutectic temperature [107].

In this study, a pure commercial Al was used as the first precursor alloy (Alloy1) the Al-33wt% Cu was the second precursor alloy (Alloy2) (Figure 5-2). Figure 5-3 (a) and (b) represent the cooling curve during solidification of Alloy1 and Alloy2 showing that the liquidus temperatures of Alloyl and Alloy2 being measured as 660°C and 545.3°C, respectively.

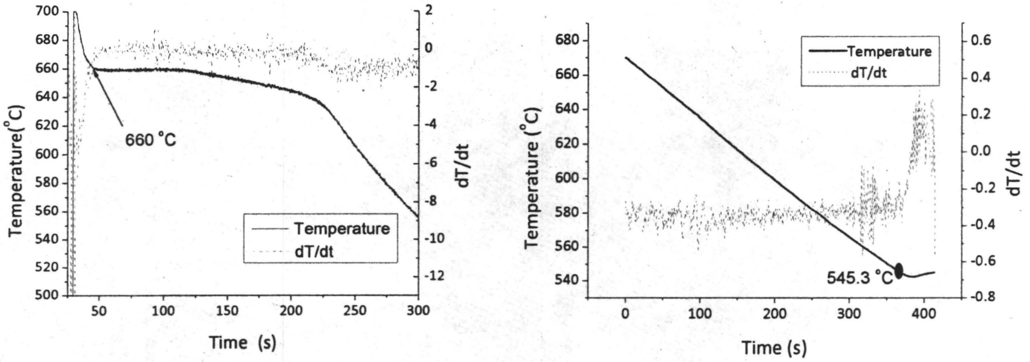

(a) (b)

Figure 5-3 Cooling curve for a) pure Al and b) Al-33wt%Cu.

5.1.2.1. CDS Experiments

Figure 5-4 (a) and (b) shows a schematic and photograph of the experimental setting-up for the laboratory CDS process, respectively, wherein the Alloy1 was taken in a crucible with a hole (9 mm diameter) at the bottom to which a funnel (9 mm diameter) was attached with a stopper blocking the hole from the inside; and Alloy 2 was taken in a second crucible which was placed directly under the funnel in the first crucible. The temperatures of Alloy1 and Alloy2 are controlled and monitored continuously by three exposed K-type thermocouples (0.62mm diameter) connected to a data acquisition system (SCXI-1100 by National Instrument[1]). When the desirable temperatures of T_1 and T_2 are reached, the stopper in the top crucible was lifted to enable Alloy1 to mix into Alloy2 in the bottom crucible.

---

[1] National Instruments, SCX 1100, USA

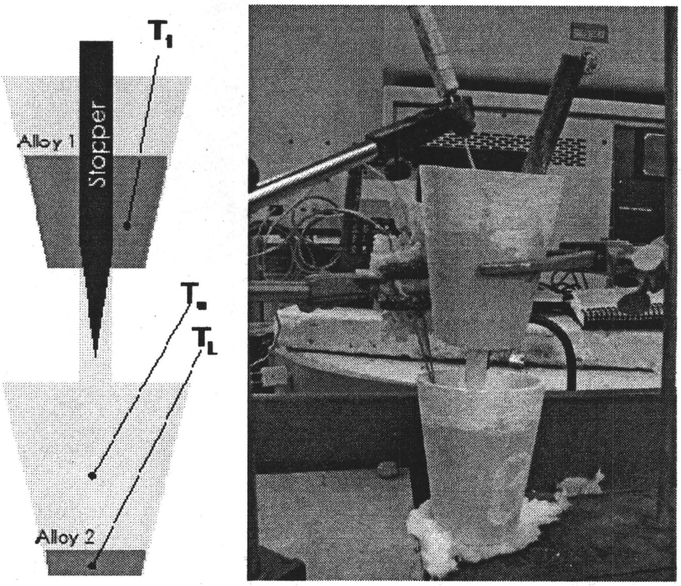

(a) (b)

Figure 5-4: Setup of laboratory experiments for the CDS process, (a) schematic and (b) photograph. Also shown are the locations of three thermocouples to control and monitor the temperatures during the process.

Two electric resistance furnaces were used to melt Alloy1 and Alloy2. Alloy2 was taken out from the furnace at a superheat of about 50°C above its liquidus temperature and the two thermocouples T_u and T_L were inserted in their respective location. The funnel and stopper were heated along with Alloy1, as well. The funnel and stopper were removed from the furnace and installed in their respective locations and the thermocouple T_1 was fitted as well as in Figure 5-4. Alloy1 was taken out of its furnace and poured in the top crucible and consequently the stopper lifted when temperature T_1 was reached for Alloy1 to mix into Alloy2. The temperatures were continuously recorded until the end of the process. The experiment was repeated several times to ensure repeatability and for two mass ratio, mr of 6 and 3 between Alloy1 and Alloy2, respectively, to obtain two respective compositions of 4.7 wt%Cu and 8 wt%Cu in Alloy3. Two mixing rates of 167 gs^{-1} and 113 gs^{-1} for the Alloy1 were employed using funnels of two different diameters of 9 mm and 6 mm, respectively. The independent variables in these experiments were T_1, T_2, mr and rate of mixing. Table 5-1 presents the design of experiments including the independent parameters and constants. The dependent parameters in these experiments were the morphology of the primary Al phase in the solidified microstructure. The mixture in these experiments was allowed to solidify in the bottom crucible without disturbing the experiment set up. A few solidified samples from the experiments in Table 5-1 were re-melted in a crucible and allowed to solidify to evaluate the liquidus temperature of the resultant alloy, Alloy3. Further in Table 5-1, the experiment designated as CONV1 was carried out by re-melting the resultant solidified alloy from experiment designated CDS2, and heated to 663 °C in the top crucible of Figure 5-4 and poured into an empty bottom crucible maintained at 555 °C

(Figure 5-4) and allowed to solidify to study the microstructure of a conventional solidification sample. Figure 5-5 (a), (b), (c) and (d) show curves of typical thermal data (temperature versus time) extracted from the three thermocouples shown in Figure 5-4, for experiments with mr = 6, mr6. Figure 5-5 (a) shows the events such as the start of mixing and end of solidification. A detailed analysis of the various events between the start of mixing and end of solidification as derived from these thermal curves would be presented in the following chapter on results.

Table 5-1: Experiment Design with independent parameters and constants for the laboratory CDS experiments.

Designation	Alloy 1			Alloy 2			Mr	Rate of mixing (gs^{-1})	Repetitions
	Mass (g)	T_1 (°C)	T_{L1} (°C)	Mass (g)	T_2 (°C)	T_{L2} (°C)			
CDS1	291.4	662	660	47.2	555.4	545	6	167	2
CDS2	290.4	665		47.1	555.4				5
CDS3	293	670		47.3	554				3
CDS4	292.1	675		47.5	555				2
CDS5	291.1	683		47.3	553				2
CDS6	291.4	668		47.2	555.4			113	2
CDS7	293	676		47.5	554				2
CDS8	292.1	680		47.3	555				2
CDS9	291.1	687		47.7	553				2
CDS10	258	662		84.4	554.8		3	167	2
CDS11	256	666		84.6	555.4				2
CDS12	259	670		84.7	554.8				2
CDS13	260	678		84.6	555.5				2
CDS14	257	687		84.4	555.4				2
CDS15	292.4	665		47.4	578.4		6		2
CONV1	Re-melt Alloy3 from CDS2 and pour into empty crucible at 555 °C to solidify								

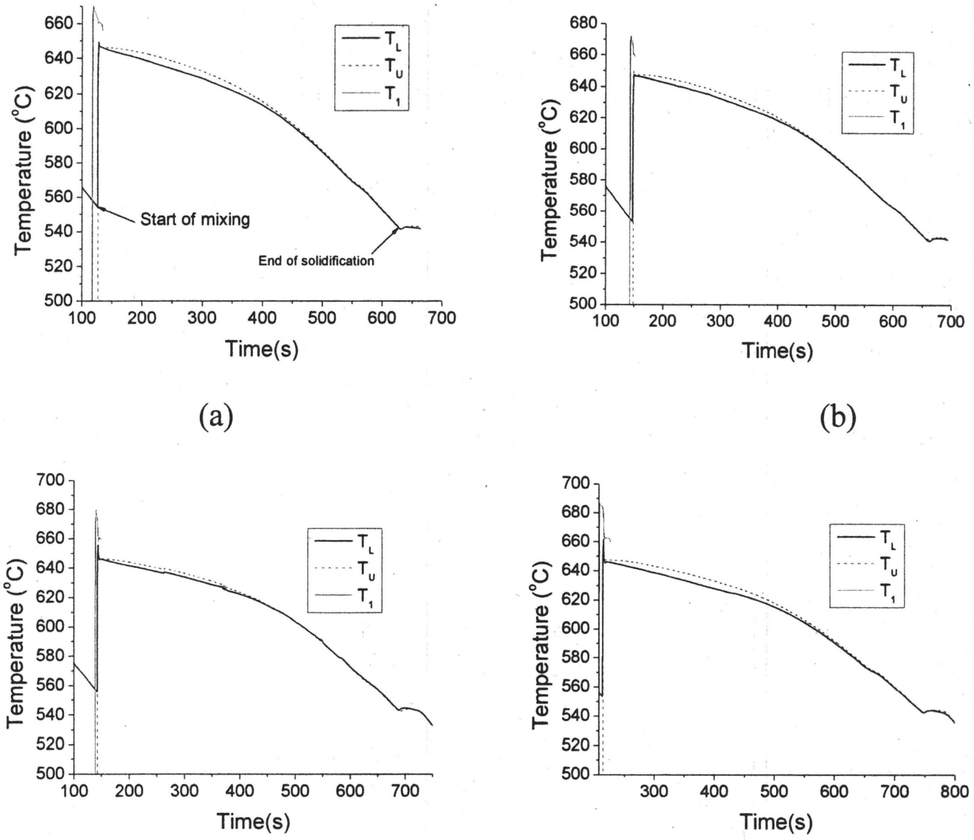

(a) (b)

(c) (d)

Figure 5-5 Typical thermal data of mr6 collected from lower(T_L) and upper (T_U) thermocouple of experiments shown in Table 5-1 (a) CDS2, (b) CDS3, (c) CDS4 and (d) CDS5.

Figure 5-6 (a) and (b) show the typical thermal data with the liquidus temperatures during solidification of the re-melted Alloys3 in both the mr6 and mr3 experiments, respectively. The two liquidus temperatures shown in Figure 5-6 (a) and (b) correspond to the equilibrium liquidus temperatures of Al-4.7wt%Cu and Al-8wt%Cu, respectively, obtained from the binary alloy phase diagram, thus confirming the validity of the design of experiments and the viability of the CDS process.

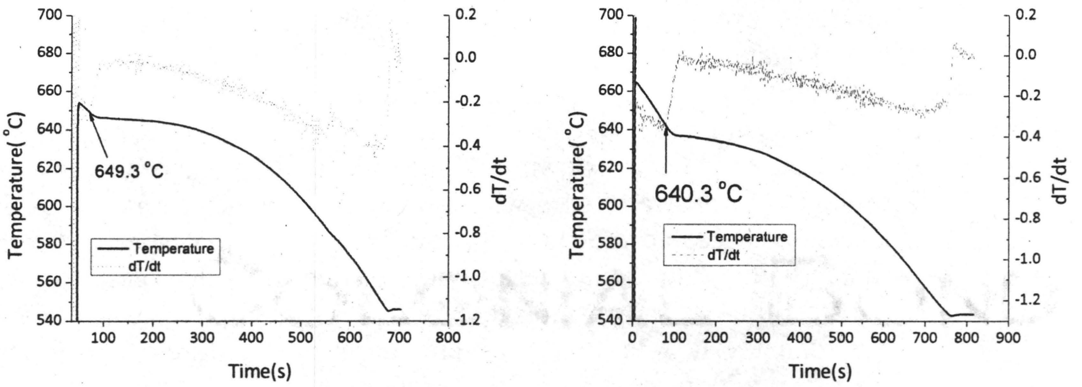

(a) (b)

Figure 5-6: Typical thermal data with liquidus temperature during solidification of the re-melted alloys in Table 5-1. (a) from experiments with mr6 aiming for Al-4.7wt%Cu as Alloy3, and (b) from experiments with mr3 aiming for Al-8wt%Cu as Alloy3.

5.2. INTERRUPTED QUENCHING EXPERIMENTS

In addition to the results obtained from the laboratory CDS experiments as presented in the following chapter of this dissertation, experiments were required to understand and provide evidence for the nucleation events and solute re-distribution during the initial stages of the CDS process. Quenching the samples by interrupting the CDS process at various initial stages was necessary and since the kinetics of the process was rapid, high quenching rates were required to successfully arrest the CDS process at various initial stages. Two types of interrupted quenching experiments were carried out as below:

- *Rapid Quenching*: Ribbon casting process for high quenching rates of over 10^4 Ks^{-1} [109]
- *Moderate Quenching*: Quenching the mixture in a solution of antifreeze liquid and dry ice, maintained at (-18 °C) for nominal quenching rates of about 10^2 Ks^{-1} [110].

5.2.1 Rapid Quenching

The Ribbon casting process equipment shown in Figure 5-7 was used in this study to quench the CDS mixture at very high quenching rate of over 10^4 K/s. A few modifications to an existing ribbon casting equipment were carried out to enable the quenching of a mixture from the CDS process. The experimental sets up with the modifications are explained below:

1. The copper wheel shown in the Figure 5-7(b) is used to quench the mixture. The wheel was rotated at 1100 r.p.m. in all the quenching experiments.
2. A long Steel tube(423mm) of 21.12mm inner diameter was fixed with one end at about 3 mm above the copper wheel and the other coming out at the top of the chamber as shown in Figure 5-7(b). The end of the tube closest to the Cu wheel was closed with steel a 5mm diameter orifice was drilled in centre to enable the flow of the mixture onto the wheel. A ceramic funnel with a 7 mm diameter of outlet orifice was fitted on the top end of the steel tube as shown in Figure 5-7(c) and the mixture was poured into this funnel. The total time between pouring the mixture into the funnel to the first liquid in contact with the wheel is about 0.3 s.
3. Induction copper coil shown in Figure 5-7(b) was used to heat the bottom of the steel tube to 700°C for all the quenching CDS experiments to prevent the effect of contact the solid steel with the mixture.

Two electric furnaces were used to melt Alloy1 and Alloy2. The funnel was heated with Alloy1 and it was first removed from the furnace and fitted in its respective location shown in Figure 5-7(c). Alloy1 and Alloy2 were taken out of their respective furnaces; and Alloy1 was mixed into Alloy2 and consequently the mixture was poured into the funnel after various time durations to enable arresting the process at various stages of mixing. The experiments were repeated several times and two mass rations in mr6 and mr3 were independently investigated with a variety of values for T_1 in each case. Table 5-2 presents design of the experiments along with the independent parameters and constants for all the interrupted quenching experiment (CDSQ1 to CDSQ10) with the ribbon casting process. The solidified samples in the form of small broken ribbons were collected in the long sealed chamber shown in Figure 5-7(a). Further, a few ribbon samples were cast with the resultant Alloy3 at a 5 °C superheat temperature above the liquidus, for both the case of mr6 (Al-4.7wt%Cu) and mr3 (Al-8wt%Cu) as shown by the experiments designations CONVQ1 and CONVQ2 in Table 5-2, respectively; and the aim of these experiments was to observe the presence or absence of any nucleation events prior to pouring the liquid (conventional) or mixture (CDS) into the funnel in the ribbon casting process. Four laboratory CDS experiments shown as CDSN1 to CDSN4 in Table 5-2, were carried out such that the alloys were mixed like described above but the mixture was allowed to solidify in the crucible and the temperature of the resultant mixture was continuously acquired through the solidification event. This enabled identification of the stages in the thermal data from which the quenching was carried out. Figure 5-8 (a) to (d) show the typical thermal curves for CDSN1 to CDSN4 experiments in Table 5-2, such that Figure 5-8(a) shown the precise location of CDSQ1 and CDSQ2, Figure 5-8(b) shows that of CDSQ3 and CDSQ4, Figure 5-8(c) shows that of CDSQ5 to CDSQ7, and Figure 5-8(d) shows the location of CDSQ8 to CDSQ10 in the CDS process. In the experiments shown in Table 5-2, the time taken from the start of mixing to the impact of the mixture on the rotating Cu wheel was evaluated in each case and superimposed on the respective data in Figure 5-8(a) and (d) to obtain the precise location of CDSQ1 to CDSQ10, respectively.

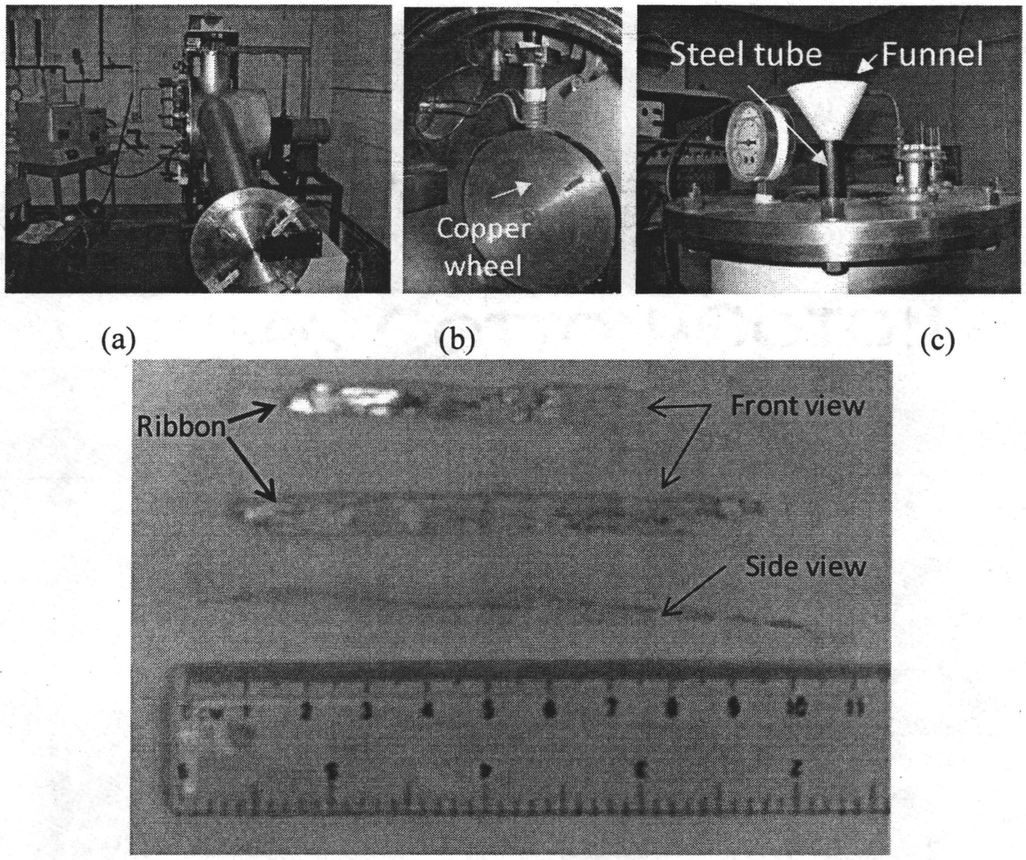

(a) (b) (c)

(d)

Figure 5-7: Photographs of equipment set-up and solidified samples for the interrupted quench experiments with the ribbon casting process. (a) Ribbon casting equipment with the two electric furnaces to melt Alloy1 and Alloy2; (b) Cu wheel, induction coil and steel tube; (c) steel tube and ceramic funnel; and (d) typical solidified ribbon samples.

Table 5-2: Experiment design with designation, independent parameters and constants for the interrupted quenching experiments with the ribbon casting process.

Designation	Alloy 1			Alloy 2			mr	Time (s)
	Mass (g)	T_1 (°C)	T_{L1} (°C)	Mass (g)	T_2 (°C)	T_{L2} (°C)		
Interrupted Quench Experiment using CDS Process								
CDSQ1	62.3	665	660	10.3	555	545	6	2.8
CDSQ2	63.1			10.5				3.3
CDSQ 3	54.6			17.1			3	2.5
CDSQ 4	54.1			17.5				3.6
CDSQ5	60.5	669		10.2			6	1
CDSQ6	60.22			10.23				2
CDSQ7	64.1			10.4				3.3
CDSQ8	55.7			16.7			3	1
CDSQ9	57.8			17.4				2.3
CDSQ10	58.1			17.14				3.5
CDSQ11	55.8	669		13.1			4.2	3
CDSN1	62.4	665		10.2			6	
CDSN2	57.9			17.2			3	
CDSN3	63.1	669		10.4			6	
CDSN4	55.7			16.9			3	
Interrupted Quench Experiment using Al-Cu Binary Alloy with Low Superheat.								
	Total mass	T_{quench}		Cu wt%		T_{L3}		
CONVQ1	73.3	656°C		4.71		649°C		
CONVQ2	73.5	645°C		8		640°C		

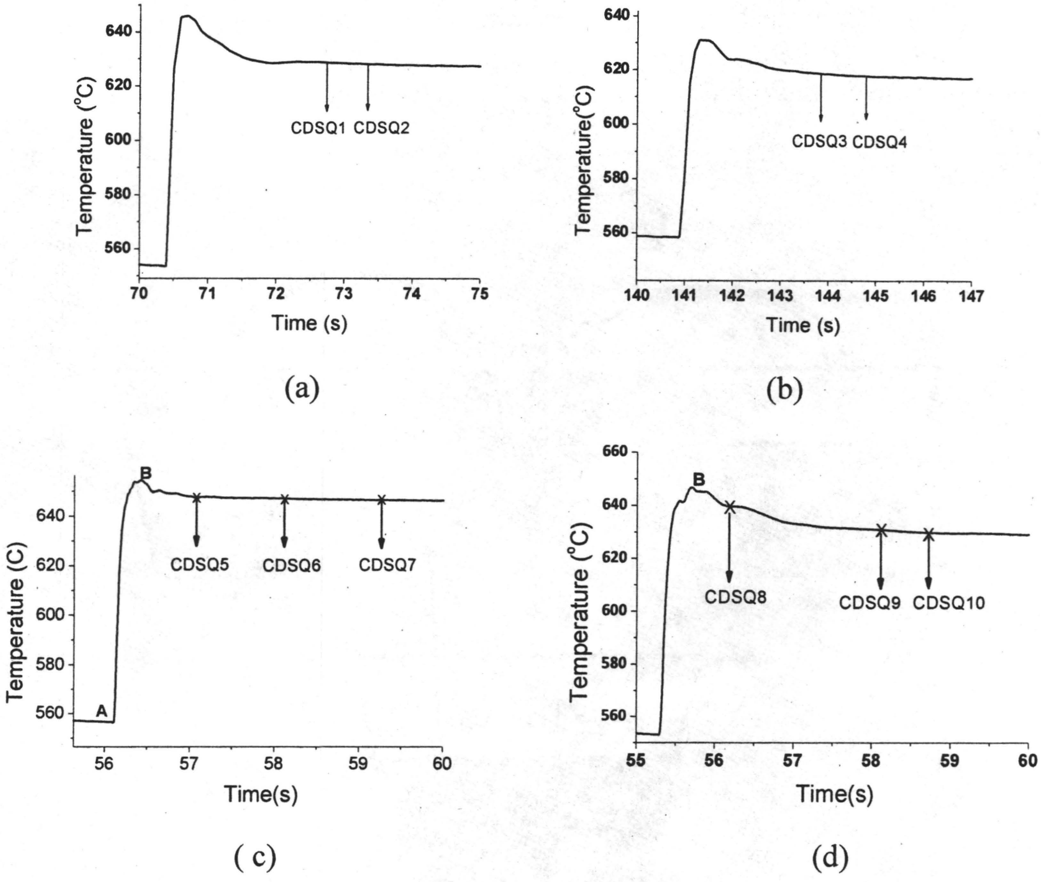

(a) (b)

(c) (d)

Figure 5-8: Typical thermal curve obtained in normal CDS experiments for the interrupted quenching experiments shown in Table 5-2; wherein the location of the quenching of each experiment is shown. (a) CDSN1 (Equivalent to CDSQ1 and CDSQ2), (b) CDSN2 (equivalent to CDSQ3 and CDSQ4), (c) CDSN3 (Equivalent to CDSQ5 to CDSQ7) and (d) CDSN4 (Equivalent to CDSQ8 to CDSQ10).

5.2.2 Moderate Quenching

One of the events that could not be captured by the rapid quenching experiments described in the previous section is the growth stage of the primary phase a few seconds after the final nucleation event in the mixture. The viscosity of the mixture is too high for it to pass through the 5 mm orifice at the bottom of the steel tube in the ribbon casting process equipment. Hence, a set of moderate quenching experiments were designed as shown by the schematic in Figure 5-9 was designed such that the mixture was directly quenched in a quenching medium made from a mixture of commercial antifreeze solution and dry ice and maintained at (-18 °C). Two experiments were carried out with the setup shown in Figure 5-9: one was a CDS process to cast Al-4.7wt% Cu alloy with Alloy1 as 290g of pure Al at 665 °C and Alloy 2 as 47 g of Al-33wt%Cu at 555 °C; and the second experiment was a conventional Al-4.7wt%Cu poured into the quenching medium from a 5 °C superheat above the liquidus temperature. Two thermocouples were used in the CDS experiments to collect the thermal data during the process such that one thermocouple was in the mixture and one in the quenching medium as shown in Figure 5-9.

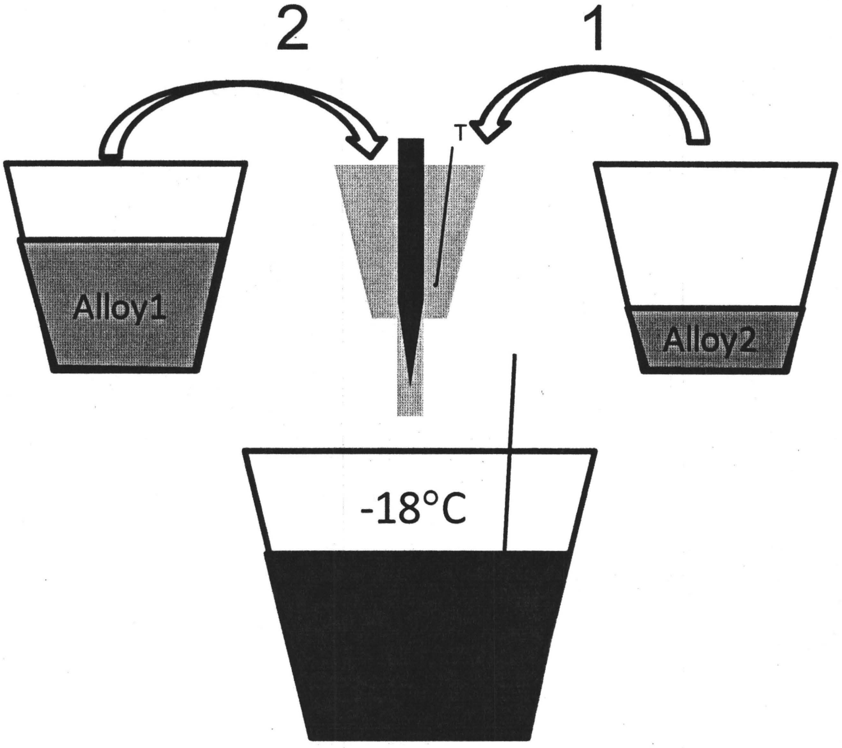

Figure 5-9: Schematic diagram of moderate quenching experiment.

5.3. NUMERICAL SIMULATION EXPERIMENTS

The results of the laboratory experiments presented the following information:

- The optimum method of mixing two fluids.
- Stages of the CDS process from analysis of the thermal data.
- Transient solute distribution in the mixture of the CDS process prior to final solidification.

Armed with these quantified data, valid numerical simulations were carried out to further investigate the following:

- Quantify the transient density distribution during the mixing process for metallic Al-Cu alloy system.

- Quantify the thermal, solute and flow field distribution in the initial stages of the CDS process to establish the environment for the growth of the nuclei during solidification.

The thermo-physical material properties of the various alloys in the Al-Cu family was derived from the thermodynamic phase diagram simulation tool, FactSage[2] and shown in Table 5-3.

Table 5-3: Thermo-physical material propeties of the alloys in Al-Cu family used in the numerical simulations.

Alloy	Property	Units	Value	Reference
Pure Al (Alloy1)	T_m	°C	660.4	Factsage
	ρ	Kg/m^3	2375	
	μ	Pa.s	0.0013	[111]
Al-33wt%Cu (Alloy2)	$L_{iquidus}$	°C	545	Factsage
	ρ	Kg/m^3	3093.8	
	μ	Pa.s	0.0027	[111]

5.3.1 Transient Density Distribution during Mixing

The transient density distribution in the macro-scale dimensions was quantified by simulating the mixing process in a commercial computational fluid dynamics software, Flow 3D[3]. The conditions in the experiment designation CDS1 of Table 5-1 was used as initial conditions for the numerical simulation. The following are the assumption in the numerical simulation:

- The densities of the liquids were a function of the solute composition in the alloy and not a function of temperature.
- Constant dynamic viscosity.
- The temperatures of Alloy1 and Alloy2 remain constant during the mixing due to the limitation of the software. The Flow 3D software can simulate either mixing two liquid to show the density distribution or one liquid to show the temperature distribution between the liquid and the environment. Since our interests were in understanding the transient density distribution between Alloy1 and Alloy2 through the mixing process, temperatures were kept constant.

---

[2] Factsage (TM) 6.1, Thermfact and GTT, Technologist-1976-2009.

[3] Flow 3D, V9.4, Flow Science Inc, USA

- The two equation K-ε model turbulent flow model [112] was used for the simulation and a no slip wall shear boundary condition was employed. Equation 5-1(a) and (b) [113,114] evaluates the Reynolds number during mixing and it was found to be 19697 for a 167 gs^{-1} mixing rate as in the simulation. This Reynolds number value would make the mixing process highly turbulent. In Equation 5-1(a) and (b), the mixing rate of Alloy1 was 167 gs^{-1}, funnel diameter, d was 9 mm, funnel area was 63.618 mm^2, density of Alloy1, ρ was 2375 $kg.m^{-3}$, minimum velocity of Alloy1 at the point of impingement with Alloy2, u was 1.1 m/s, and dynamic viscosity, μ was 1.3 mPa.s.

Equation 5-1

$$u = \frac{\dot{m}}{\rho A} \qquad (a)$$

$$Re_d = \frac{\rho\, u\, d}{\mu} \qquad (b)$$

Figure 5-10 (a), (b) and (c) show typical snapshot images of the transient density distribution in the initial, intermediate (1s) and final stages of the mixing process, respectively

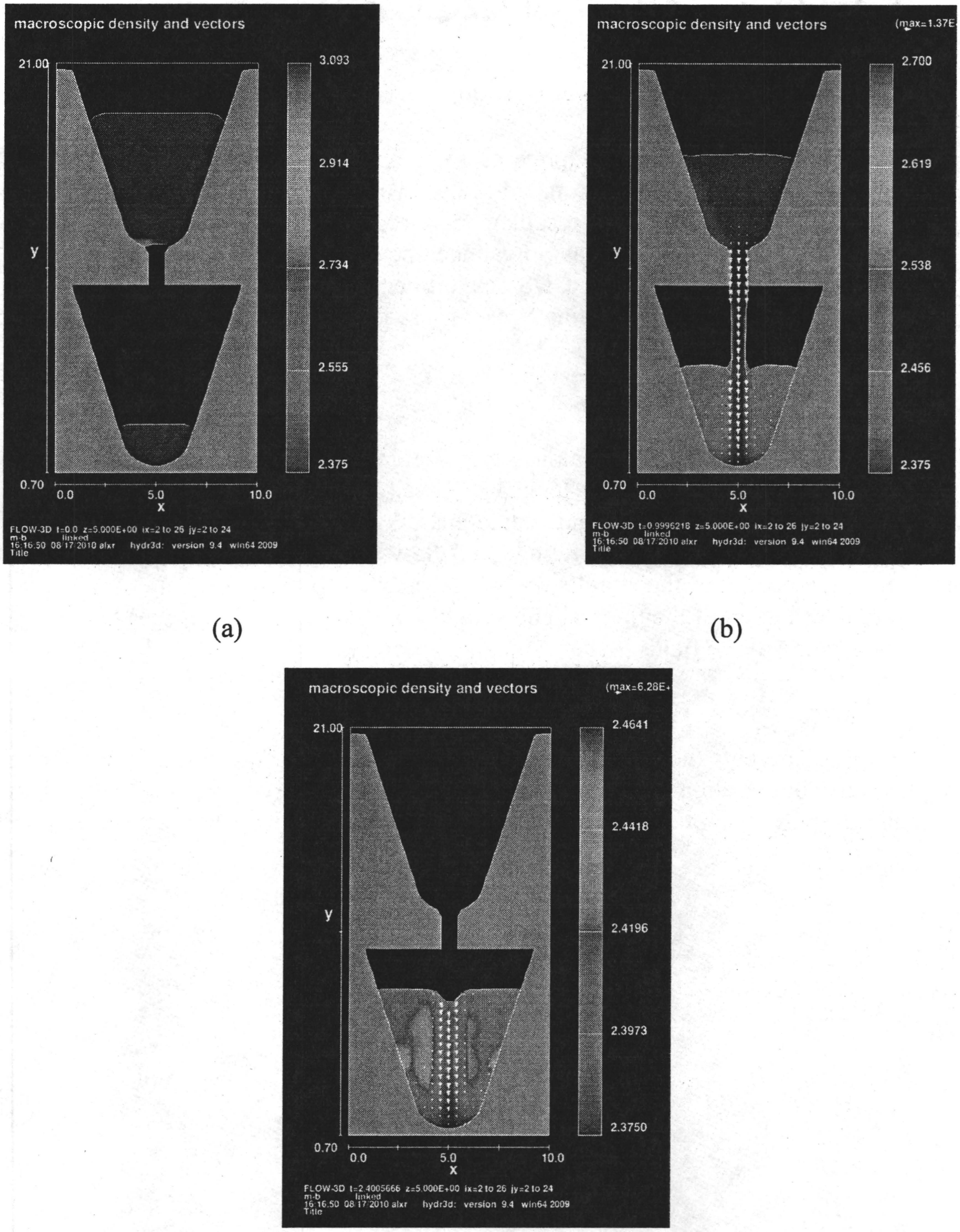

(a)

(b)

(c)

Figure 5-10: Transient density distribution from the numerical simulation of the mixing of Alloy1 into Alloy2 in the CDS process. The initial conditions were that of the experiment designated CDS1 in Table 5-1.(a) Initial condition, (b) time of mixing is 1s (c) ending of mixing. The visual scale for quantified macroscopic density (g/cc) is presented as well.

5.3.2 Numerical Model of Solute Distribution

The simulation study shown in the previous section would show the instantaneous density distribution during mixing in the macro-scale. To further study the distribution of the thermal and solute fields in the resultant mixture, a micro-scale simulation study was required along with experiment data to validate the simulation. The experiment data was obtained from the laboratory CDS experiments and the interrupted quenching experiments with the ribbon casting process; as described in Sections 5.1.2 and 5.2.1, respectively.

A computational fluid dynamics numerical model and algorithm was developed using the FORTRAN computer program language based on the finite volume method to numerically solve the energy and solute mass conservation equations. Due to the complexities involved in incorporating fluid flow in these simulations, it was omitted. However, the results of the simulation was envisioned to present a better understanding of the re-distribution of the thermal and solute fields during the last stages of mixing and homogenization of the fields in the resultant alloy mixture.

Equation 5-2 presents the energy conservation equation and Equation 5-3 represents the solute mass conservation equation used in the model. The assumptions in the model were that all transport phenomena were in one dimension and the fluid flow was negligible.

Equation 5-2

$$\frac{\partial T}{\partial t} = \alpha \frac{\partial^2 T}{\partial x^2}$$

Equation 5-3

$$\frac{\partial C}{\partial t} = D \frac{\partial^2 C}{\partial x^2}$$

The boundary conditions for the temperature field, T(x,t) in Equation 5-2 is presented below:

$$\frac{\partial T(0,t)}{\partial x} = 0$$

$$\frac{\partial T(X_T,t)}{\partial x} = 0,$$ where X_T is the half cell length.

$$T(x, 0)=\begin{cases} T_1 & \text{at } 0 \le x \le X_1 \\ T_2 & \text{at } X_1 \le x \le X_T, \end{cases}$$ where X_1 is the initial length of Alloy1

The boundary conditions for the solute (Cu) field, C(x,t) in Equation 5-3 is presented below:

$$\frac{\partial C(0,t)}{\partial x}=0$$

$$\frac{\partial C(X_T,t)}{\partial x}=0,$$ where X_T is the half cell length.

$$C(x, 0)=\begin{cases} 0 & \text{at } 0 \le x \le X_1 \\ 33 & \text{at } X_1 \le x \le X_T, \end{cases}$$ where X_1 is the initial length of Alloy 1

Figure 5-11 shows the schematic of the computing domain for the model with the boundary conditions shown at the respective boundaries. Initially, the domain has two alloys, Alloy1 and Alloy2 as sub-domains, wherein the Cu concentration in Alloy1 was 0 and that is Alloy2 was 33 to reflect the pure Al mixing with the Al-33wt%Cu alloy in the experiments, respectively. The heat flux would diffuse from Alloy1 to Alloy2 and the solute (Cu) mass will diffuse from Alloy2 to Alloy1.

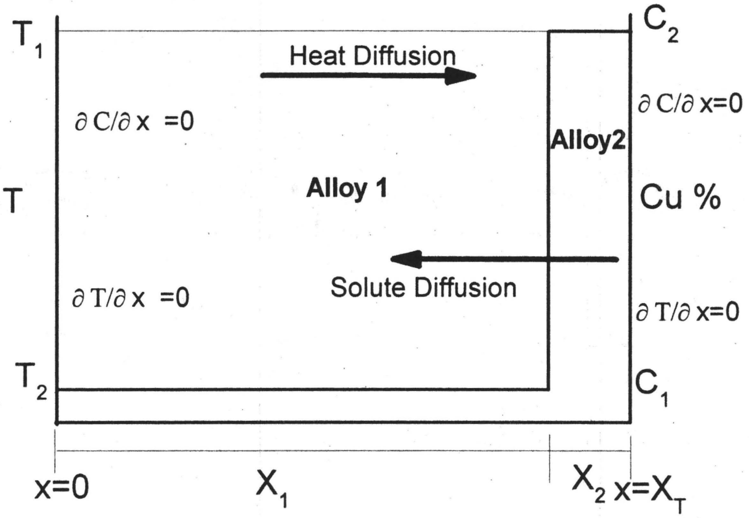

Figure 5-11 A solute model represents the boundaries and the initial condition.

The domain represents half a cell with the centre of the cell as origin and the half length of the cell as X_T. The length of Alloy1 and Alloy2 in the initial domain was X_1 and (X_T-X_1), respectively. X_1 and X_2 were evaluated by Equation 5-4 (a) and (b), respectively.

Equation 5-4

$$X_1 = X_T - X_2 \quad \text{(a)}$$

$$X_2 = X_T\left(\frac{C_0}{C_2}\right) \quad \text{(b)}$$

For the purposes of validating the numerical simulation, one set of numerical experiments were carried out with the cell dimensions, boundary conditions and initial conditions obtained from specific cells in the microstructure of samples obtained from four experiments shown in Table 5-2 namely CDSQ6 to CDSQ10.

Further, for the purposes of understanding thermal and solute re-distribution during the CDS process, in Figure 5-11, the length of the half-cell domain was 6 μm (X_T) for an initial mass ratio of 6 (mr6) and 3 μm for mr3, as obtained from the average cell size in the microstructure from the experiments, as shown in Figure 5-12 for the two mass ratios, mr3 and mr6.

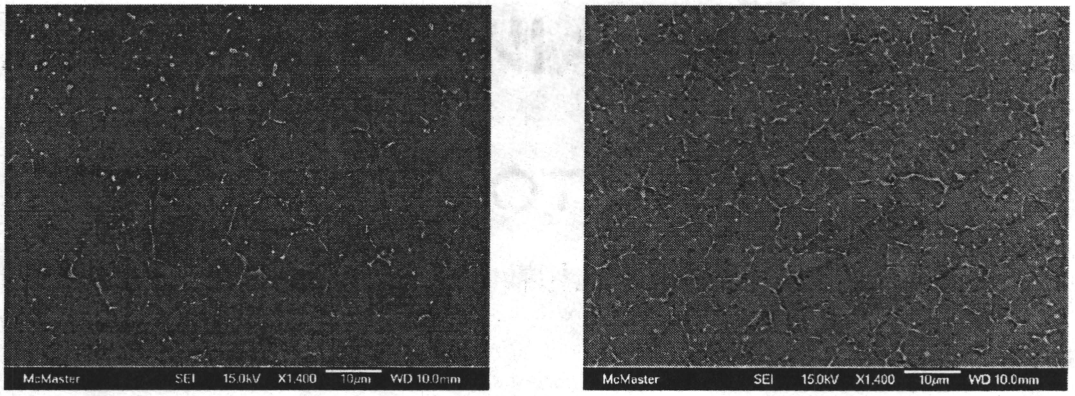

(a) (b)

Figure 5-12 Cells at the end of the mixing stage in the CDS process as obtained from a bright field image in an SEM. (a) mr6 and (b) mr3 obtained from the interrupted quenching experiments, CDSQ6 and CDSQ9 in Table 5-2.

In Equation 5-2, α was evaluated by Equation 5-5, wherein c and K_L were 1180 (J/Kg k) [13] and 95 $W.m^{-1}$ k^{-1}[115], respectively.

Equation 5-5

$$\alpha = \frac{K_L}{\rho\, c}$$

ρ was the instantaneous bulk density of the liquid mixture at any location and is a function of the instantaneous solute concentration, C as evaluated by Equation 5-6; and the liquidus temperature was evaluated from the instantaneous concentration of Cu with the expression presented in Equation 5-7. The R^2 value from the results of the regression analyses shown in Equation 5-6 and Equation 5-7 are also shown alongside the respective equations.

Equation 5-6

$$\rho = 2377.8 + 15.796\ (C) + 0.17759\ (C)^2 \qquad \rightarrow R^2 = 0.99997$$

In Equation 5-3, D was assumed to be function of the temperature as evaluated by the Arrhenius equation shown in Equation 5-8. In Equation 5-8, T is in Kelvin, D_o is Pre-exponential Factor (8.10E-07 $m^2.s^{-1}$), Q is 3.89E+04 $J.mole^{-1}$ and R is 8.31432 $J.mole^{-1}.K^{-1}$ [116].

Equation 5-7

$$T_L = 660.4 - 2.359\ (C) - 0.03094\ (C)^2 \qquad \rightarrow R^2 = 0.999$$

Equation 5-8

$$D = D_o\ exp\left[-\frac{Q}{RT}\right]$$

5.3.2.1Numerical Procedure

To ensure stability of the numerical procedure, the time step for energy transport, Equation 5-2 and Equation 5-3, was less than the value of $\frac{(\Delta X)^2}{\alpha}$, where ΔX was the dimension of one mesh. Figure 5-13 presents the flow chart for the numerical procedure adopted in the algorithm for the simulations.

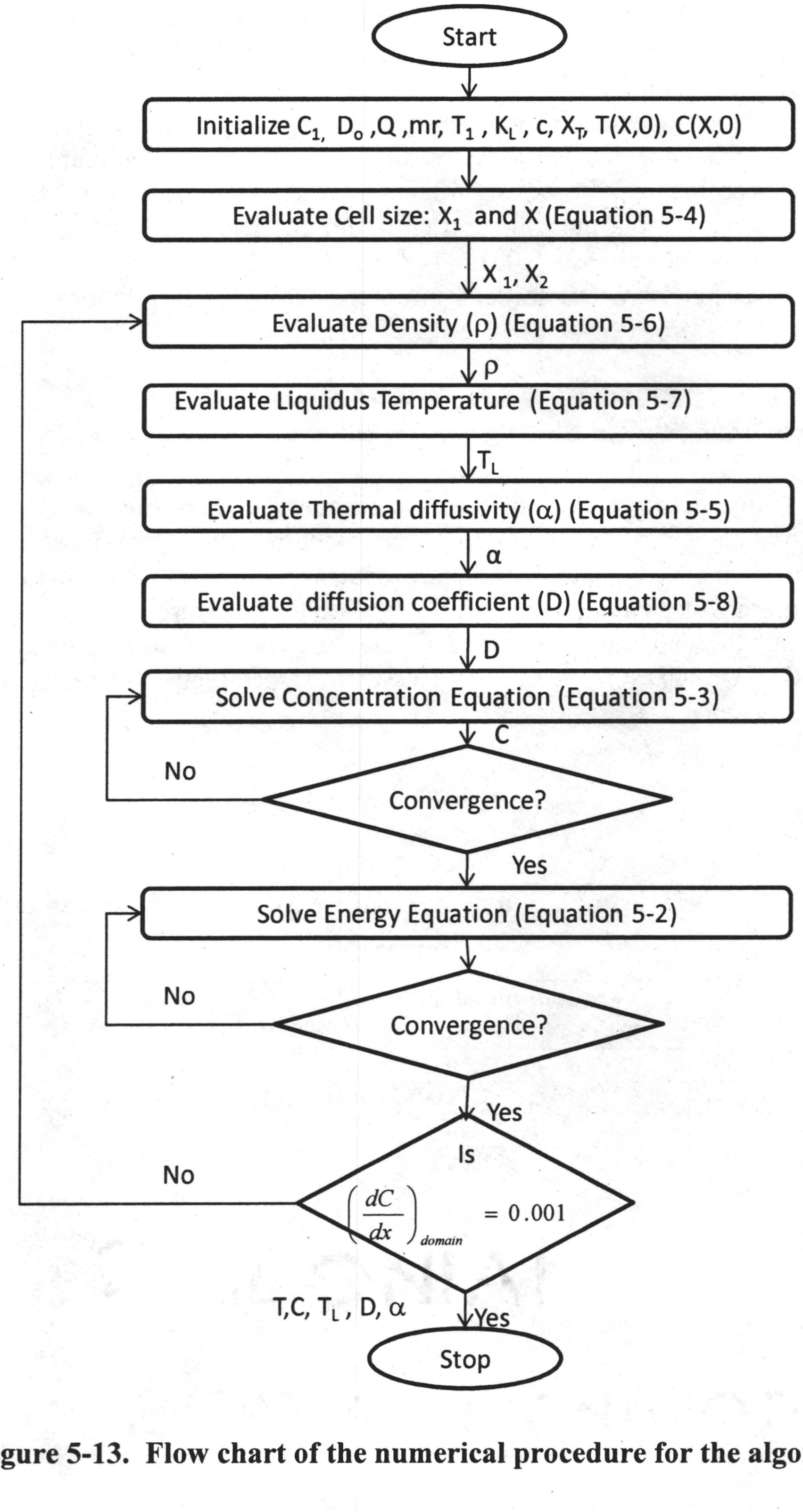

Figure 5-13. Flow chart of the numerical procedure for the algorithm.

In Figure 5-13, the density field, instantaneous liquidus temperature and diffusion coefficient were evaluated by Equation 5-6 to Equation 5-8, respectively. The concentration equation defining the transient solute re-distribution shown by Equation 5-3 was solved to obtain the instantaneous solute concentration distribution in the domain. This was followed by the solution to the energy equation shown in Equation 5-2 to obtain the instantaneous temperature distribution in the domain. Since, the temperature discussion would be significantly faster than the mass diffusion; the simulations were carried out until the concentration gradient of the solute in the domain reached a near constant value of 0.001. The results of the transient thermal and solute fields were analysed at many intermittent time steps during the simulations.

5.3.2.2Simulation Experiments

There were many numerical simulation experiments carried out to understand the transient thermal and solute fields and study the effect of critical parameters on the same. Table 5-4 shows the designations and independent parameters used in the numerical simulation experiments; wherein NS1, NS2, NS3 and NS4 were numerical simulations carried out with the cell dimensions and boundary conditions were obtained from the experiments CDSQ6, CDSQ7, CDS9 and CDSQ10, respectively, to enable validation of the numerical model.

Table 5-4: Numerical simulation experiments with designations and independent parameters.

Designation	$2X_T$ (μm)	Initial mr	C_1 Wt.%	C_2 Wt.%	C_o Wt.%	T_1 °C	T_2 °C
NS1	9	3.79	0	33	6.888	669	555
NS2	6	3.51			7.316		
NS3	7	5.46			5.1		
NS4	6	1.93			11.25		
NS5	12	6			4.714	665	
NS6					4.714	670	
NS7					4.714	680	
NS8	6	3			8.25	665	
NS9					8.25	670	
NS10					8.25	680	
NS11	12	6			4.714	665	565
NS12							580

5.4. ORGANIC ALLOY SYSTEMS

The mechanism for the various stages in the CDS process was hypothesized by the experiments and numerical models as described in Sections 5.1 to 5.3. The hypothesis along with the effect of critical process parameters were verified by carrying out laboratory experiments with Succinonitrile (SCN) based organic alloys such as SCN-Acetone (Ac), SCN-water and SCN-D-Camphor (DC). The SCN based organic alloys were chosen because these alloys form binary eutectic reaction in the phase diagram at around the room temperature regime and they are transparent which enables an ease of visualization of the CDS process. Further, the final stages of solidification after the homogenization of the thermal and solute fields could be visualized using the SCN based organic alloys.

A glass mould with a rectangular cross-section of 75 mm length and 25 mm width with a height of 3 mm was used to shape the resultant mixture. The two precursor alloys were taken in a clean Cu crucible and heated to the appropriate respective temperatures over a hot plate with a K-type thermocouple inserted in each to control and monitor the respective temperatures. The glass mould had two K-type thermocouples (for repeatability) inserted in the cavity to monitor the temperature during the solidification process. The Alloy1 was poured into Alloy2 crucible to make a mixture and subsequently the mixture cast into the pre-heated glass mould cavity. The process was allowed to take place under a stereo microscope at a set magnification level for visual recording of the event.

5.5. MICROSTRUCTURE ANALYSIS

All the microstructure analyses for the experiments described in Sections 5.1, 5.2 and 5.4 were carried out on samples sectioned from the area around the respective thermocouples in these experiments. The samples were mounted using bakelite mount, ground and polished in automatic polishing machines. Etching was carried out on some samples with freshly prepared Keller's reagent (1ml HF, 1.5ml HCL, 2.5ml HNO_3 and remainder H_2O). The microstructure analysis was carried out using the stereo; light optical and scanning electron microscopes. A stereo microscope type Nikon AZ 100M[4] was used along with an image analysis software, NIS BR 3.14. Light optical microscopy was carried out with the Nikon Eclipse LV100 microscope equipped with the type NIS BR 3.04 image acquisition system. The SEM analysis was carried out with the JEOL JSM-7000F[5] equipped with energy dispersive x-ray analysis system. Quantitative metallography on all the microstructure images was carried out using the ImageJ[6]

---

[4] Eberbach corporation, ANN Michigan.

[5] JEOL, INCA Oxford

[6] ImageJ, Image processing and Analysis in Java, 1.42q Java 1.6.0 (32 bit)

software. Since the grains in the resultant microstructure were nearly equiaxed, the grain sizes were determined by the linear intercept method as prescribed in the ASTM test method E112 [117] and using a minimum of 20 lines in one microstructure .

CHAPTER 6. RESULTS AND DISCUSSION

The various experiments and numerical simulations described in CHAPTER 5 were carried out to identify and understand specific features in the stages of the CDS process. These were carried out randomly as and when required to better understand specific features in the mechanism of the CDS process.

In this section, the events in the various stages of the CDS process would be presented in detail as derived from the evidences obtained in the various experiments and numerical simulations. This section would be broadly classified in the following topics:

- Study of the mixing process
- Mechanism of the CDS process.
- Study of the critical process parameters.
- Verification of the proposed mechanism

6.1. STUDY OF THE MIXING PROCESS

The mixing process was optimized by the experiments described in section 5.1 where in visual observation and thermal data obtained during mixing of water and water; and water and milk was used for the study.

The study was carried out for the following dependent variable criteria during the mixing process:

- Minimize bubble formation.
- Homogenization of the thermal field.
- Homogenization of the density field.

6.1.1Minimize Bubble Formation

Figure 6-1 (a), (b) and (c) shows the photographs taken during the stages in the mixing process when the warm water was mixed into the water at room temperature by direct pouring. In these photographs, the extensive bubble formation is apparent. Figure 6-1 (d), (e) and (f) show the progressive photographs during mixing when the warm water was mixing into the water at room temperature using a funnel; wherein there was negligible bubble formation due to the lack of any notable turbulence during the mixing process. During the CDS process in Al alloys, bubble formation would be detrimental to the mechanical properties of the resultant casting due to high levels of gas porosity. A funnel was used in all experiments in this project to affect a mixing process with minimum bubble formation.

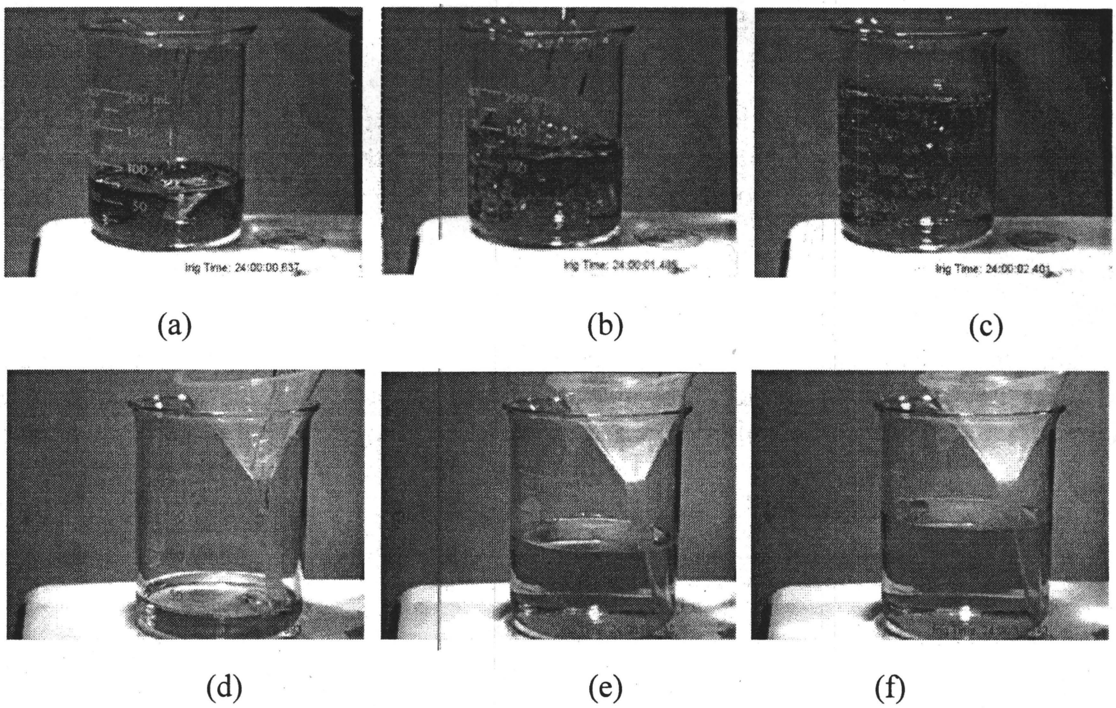

(a) (b) (c)

(d) (e) (f)

Figure 6-1 Illustration of bubble formation during water-water mixing, (a), (b) and (c) direct mixing at start, middle and end of mixing, and (d), (e) and (f) mixing through a funnel at start, middle and end of mixing.

6.1.2Homogenization of the Thermal Field

There are two methods of mixing the two precursor liquids: the larger thermal mass (temperature and mass) being mixed into the smaller and vice-versa. Temperature data from the experiments described in Section 5.1.1.1 revealed the more efficient of these two mixing processes. Figure 6-2 (a) and (b) show the temperature distribution obtained by the four thermocouples in Ch1 to Ch4 for mixing the higher thermal mass into the lower and vice-versa, respectively.

Figure 6-2 (a) shows that when the higher thermal mass is mixed into the lower one, the temperature in the mixture equalized almost instantly as shown by the negligible differences shown by thermocouples in Ch1 to Ch3 at different locations in the resultant mixture. Figure 6-2 (b) shows that when the lower thermal mass is mixed into the higher, there is thermal stratification occurs along the height of the resultant mixture as shown by the marked difference (stratification) in temperature among thermocouples in Ch1 to Ch3; thus showing that this method of mixing was inefficient for instantaneous temperature homogenization in the resultant mixture during mixing.

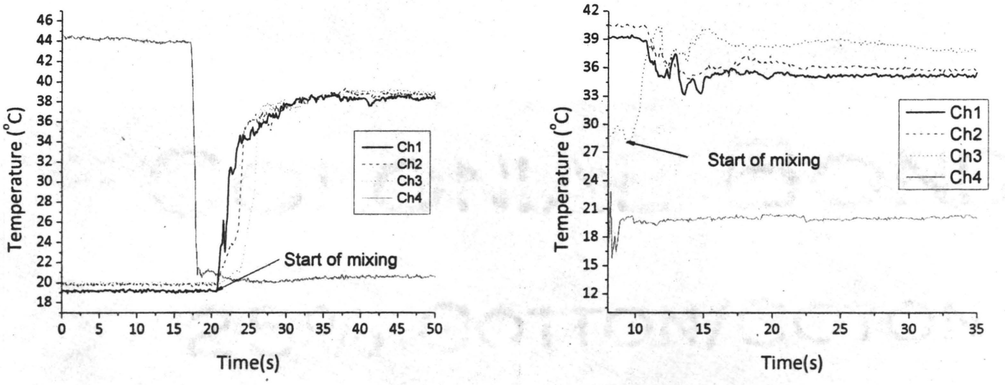

(a) (b)

Figure 6-2: Transient temperature distribution during mixing of, (a) warm water into cold water and (b) cold water into warm water, as described in Section 5.1.1.1. Ch4 shows the temperature of warm water (liquid 1) before mixing.

The results from this study showed that for a successful CDS process, the higher thermal mass should be mixed into the lower thermal mass as was practiced in all the experiments in this study. A high rate of homogenization of the thermal field is essential to achieve a stable growth of the S/L interface, decrease the undercooling of Alloy1, facilitate the copious nucleation of the primary phase in the mixture and increase the nucleation rate in the mixture during the CDS process [**104**].

6.1.3Homogenization of the Density Field

The results of the previous section showed that the mixing of the higher thermal mass into the lower proved to be more efficient. To further understand the homogenization of the density field when the two precursor liquids have a difference in density, warm water was mixed into milk at room temperature as described in Section 5.1.1.2. The water had a lower density than milk.

Figure 6-3 (a), (b) and (c) show photographs obtained with increasing time of mixing when the higher thermal mass was mixed into the lower. These photographs show that the solute (milk) homogenization is fairly rapid at all stages of mixing. Figure 6-3 (d), (e) and (f) show photographs obtained with increasing time of mixing when the lower thermal mass was mixed into the higher; wherein the stratification of the milk at the bottom of the resultant mixture could be observed at all stages of mixing and complete homogenization could not be achieved even after the end of the mixing process.

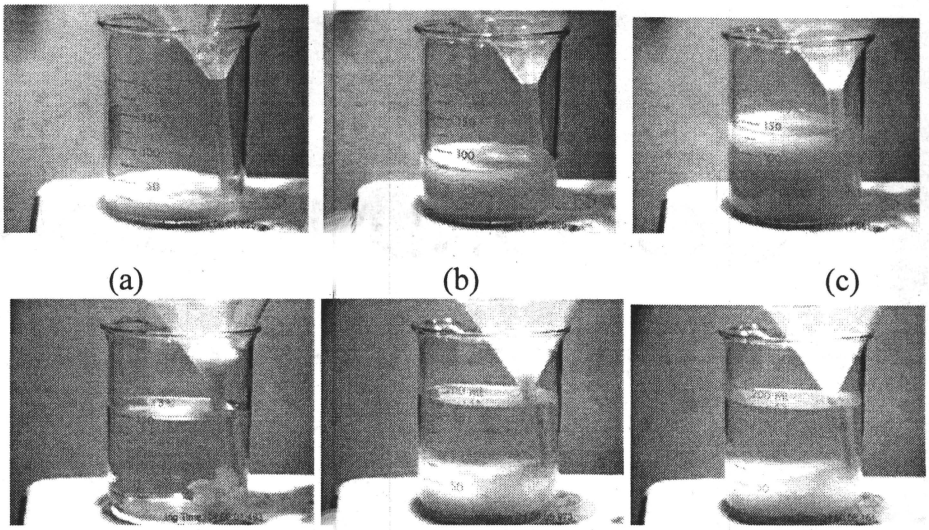

(a) (b) (c)

(d) (e) (f)

Figure 6-3: photos of mixing experiments of warm water into cold milk (a, b, c) and cold milk to warm water (d, e, f). Pouring time is (a) 3s, (b) 40s, (c) 90s, (d) 3 s, (e) 40s, and (f) 60s.

These results show that the density difference between the two precursor liquids plays a critical role during the mixing process; and mixing the higher thermal mass into the lower is critical to obtain a valid CDS process with homogeneous solute compositions across the resultant casting.

6.2. <u>MECHANISM OF THE CDS PROCESS</u>

The CDS process is aimed to achieve a cast product of an Al cast or wrought alloy with a non-dendritic morphology of the primary Al phase. Two precursor alloys of specific composition and temperature are so chosen such that when the alloy with the higher thermal mass is mixed with the lower thermal mass, a resultant mixture is obtained with the desired solute concentration to be immediately cast into a near net shaped product with a casting process which may or may not be pressure assisted. The success of the CDS process depends on optimizing the various process and alloy variables to obtain a nearly non-dendritic microstructure along with the superior properties exhibited by the alloy composition and microstructure.

To fully optimize the various process parameters such as composition and temperature of the precursor alloys, method and rate of mixing, residence time after mixing and before casting and casting parameters could be optimized only when an in-depth understanding of the events during the various stages of the process is developed. Various experiments as described in CHAPTER 5 were carried out during the course of this study to achieve such an understanding.

In this section, an elaborate description of the various events occurring in the CDS process would be hypothesized along with validation from appropriate experiment results. The CDS process could be broadly subdivided into the following stages:

- Mixing Stage
- Re-Distribution of Thermal and Solute Fields, and Nucleation
- Growth of Stable Nuclei

Figure 6-4 presents a schematic of the thermal data obtained during the CDS process starting from the mixing of the alloys during segment AB to the final solidification past the point D.

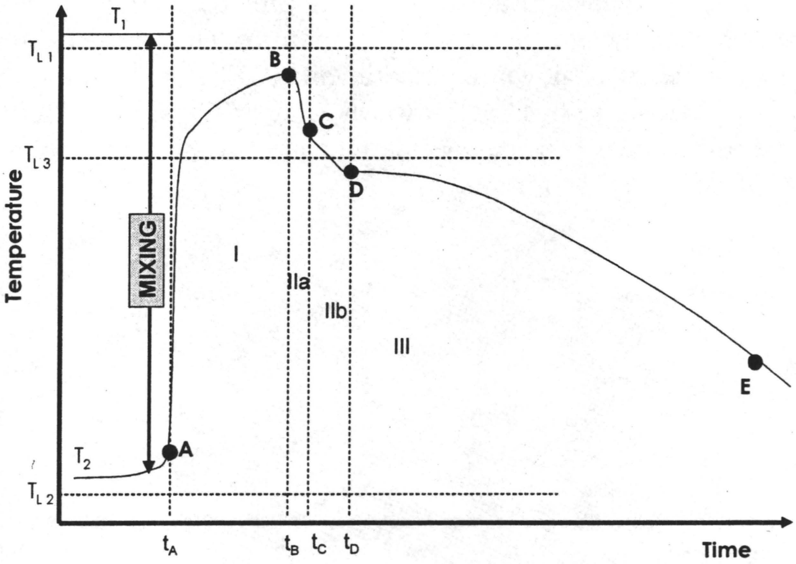

Figure 6-4: Schematic of the typical thermal profile observed in the CDS process. There are three stages starting from the mixing of the alloys during segment AB the solidification in segment DE.

The schematic in Figure 6-4 was obtained from a critical examination of the various thermal curves obtained from the experiments described in Table 5-1. The three stages of the CDS process described above were derived from the examination of the thermal data along with the microstructural analysis. The segment AB (Stage I) denotes the stage of mechanically mixing the Alloy1 at T_1 into Alloy2 at T_2 to form a resultant mixture of

Alloy3. The segment BCD (Stage II: (a) and (b)) denotes the stage of re-distribution of the thermal and solute fields in the resultant mixture and the final nucleation event and solidification of Alloy3 takes place at and after point D, respectively.

Figure 6-5 presents typical experiment data for the CDS2 to CDS5 as described in Table 5-1 using the experiment set up shown in Figure 5-4; wherein a mass ratio of mr6 and mixing rate of 167 gs^{-1} were adopted. Figure 6-6 presents typical experiment data for the CDS6 to CDS9 as described in Table 5-1 ; where in a mass ratio of mr6 and mixing rate of 113 g/s were adopted. Figure 6-5 and Figure 6-6 show the location of the points A, B, C and D shown in Figure 6-4, denoting the existence and location of the three stages in each experiment condition. The location of point C denotes the near equalization of the temperature in the resultant mixture of Alloy3 after mixing. The point A is determined by the sharp increase in the initial temperature T_2 of Alloy2 as measured by the thermocouple T_L in Figure 5-4, the point B is measured by the highest temperature recorded by thermocouple T_L, the point C is measured by the intersection of the temperatures measured by thermocouples T_U and T_L in Figure 5-4, and the point D is measured by the sharp change in the slope of the time derivative of the temperature T_L denoting the large final nucleation event in the mixture. The existence of the three stages in the CDS process was also shown for experiments CDS 10 to CDS14 using a mass ratio of mr3 and mixing rate of 167 gs^{-1} as shown in Figure 6-7; wherein the location of point C could not be ascertained because the thermocouple T_u (Figure 5-4) was not used in experiments CDS10 to CDS14 for mr3.

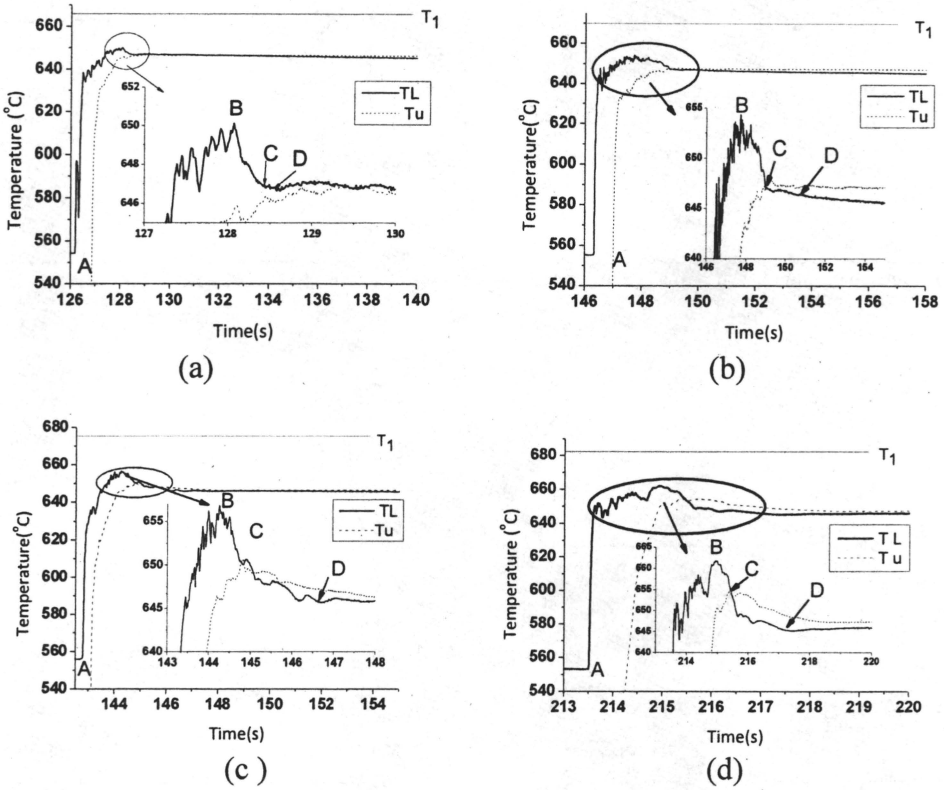

(a) (b)

(c) (d)

Figure 6-5: Typical thermal curves of mr6 and 167gs^{-1} mixing rate show points A,B,C and D in CDS process from experiments shown in Table 5-1: Experiment Design with independent parameters and constants for the laboratory CDS experiments. Table 5-1. (a)CDS2, (b)CDS3, (c) CDS4 and (d) CDS5.

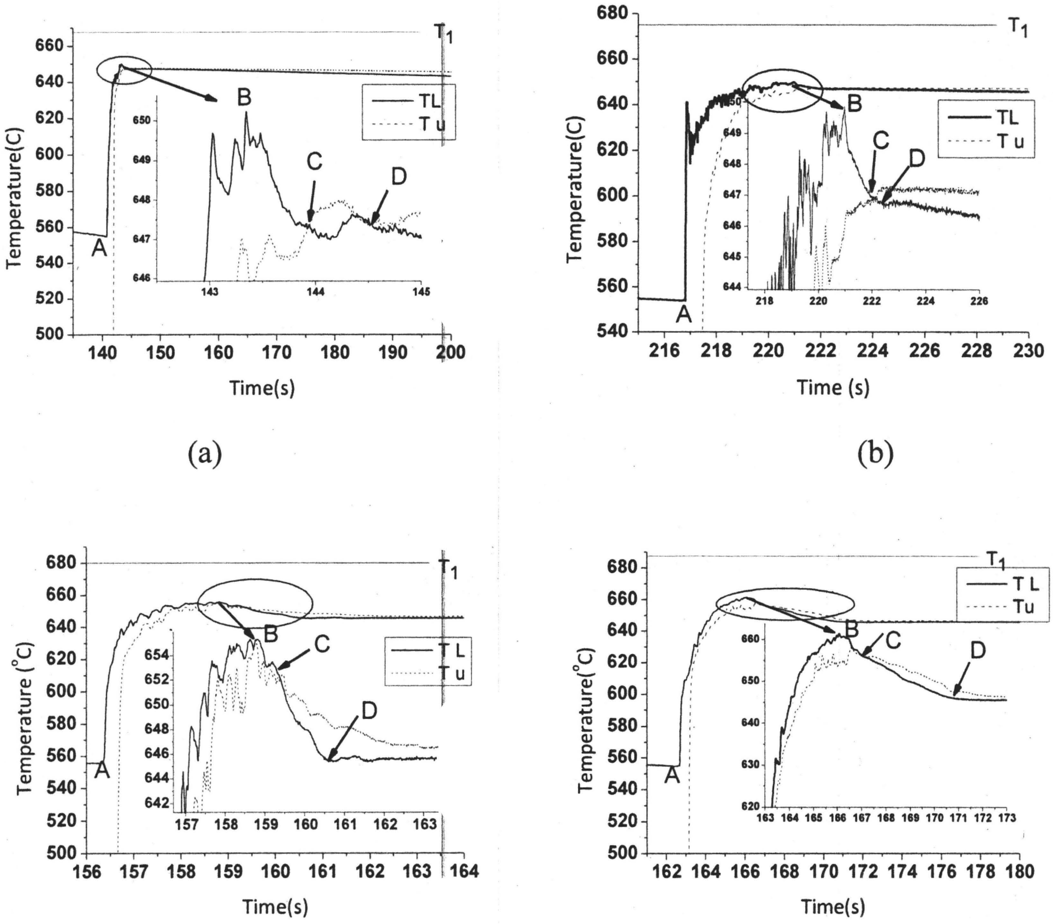

(a) (b)

(c) (d)

Figure 6-6: Typical thermal curves of mr6 and 113 gs^{-1} mixing rate show points A,B,C and D in the CDS process from experiments shown in Table 5-1. Table 5-1 (a)CDS6, (b)CDS7, (c) CDS8 and (d) CDS9.

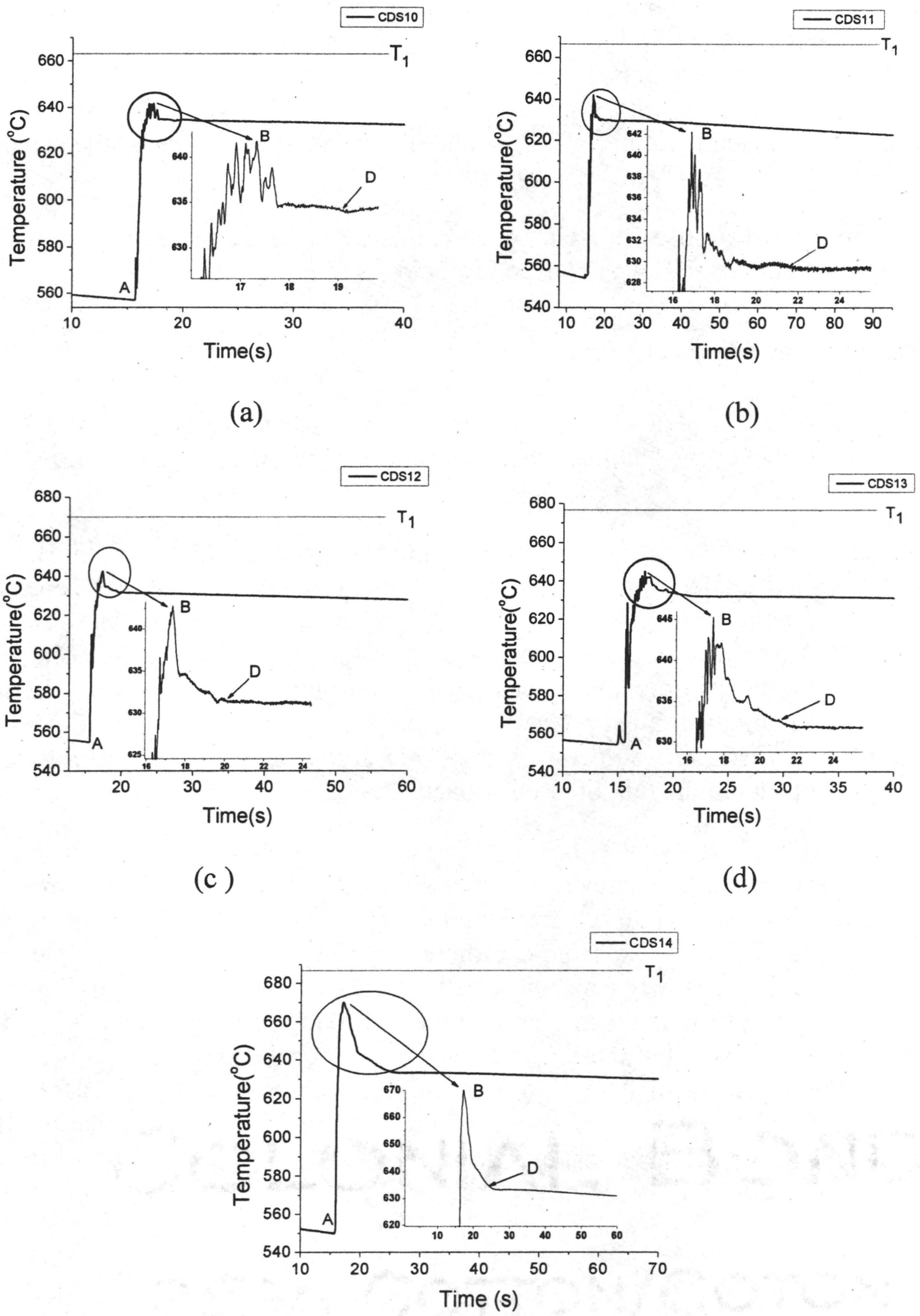

(a)

(b)

(c)

(d)

(e)

Figure 6-7: Typical thermal curves for mr3 and 167 gs^{-1} mixing are showing the three stages of the CDS process with points A.B and D from experiments shown in Table 5-1. (a) CDS10, (b) CDS11, (c) CDS12, (d) CDS13 and (e) CDS14.

The results show in Figure 6-5 to Figure 6-7 validates the existence of the three stages in the CDS process as shown in Figure 6-4. The location of the points B, C and D depend on the alloy and process parameters such as the mass ratio of the two precursor alloys, superheat of Alloy1 above its liquidus temperature (T_1-T_{L1}), the superheat of Alloy2 above its liquidus temperature (T_2-T_{L2}) and the difference between their respective liquidus temperature (T_{L1}-T_{L2}).

The following sub-sections would elaborate on the details of the events in the three stages marked by segment AB, BCD and DE in Figure 6-4.

6.2.1 Mixing Stage – *Segment AB*

Alloy1 was mixed into Alloy2; the nucleation of the primary phase of Al takes place from Alloy1. The events taking place during the mixing stage in segment AB are presented below:

Event (1) *Start of the mechanical mixing* at point A and end around point B.
Event (2) *Heat added to the system from Alloy1* (enthalpy of Alloy1) depending on the thermal mass of Alloy1.
Event (3) *Nucleation of primary phase of Al takes place from Alloy1.* The enthalpy of fusion from the nucleation event would be released into the mixture during the mixing process.
Event (4) *Re-distribution of the thermal and solute fields* by diffusion/convection occurs in the mixture in the macro-scale.

The mechanical mixing (Event 1) begins at point A and ends around point B as shown in Figure 6-4. The Reynolds number, Re_d as evaluated in Section 5.3.1 was in excess of 4000 for both the mixing rate experiments of 167 gs^{-1} and 113 gs^{-1}; showing that the mechanical mixing process was quite turbulent. The time taken to completely pour Alloy1 into Alloy2 was nearly constant for all experiments at a specific mixing rate. For the rate of 167 gs^{-1} of mixing, the average time of mixing was 1.7s and that for the 113 gs^{-1} of mixing was 2.6s. Figure 6-8 (a) and (b) shows the temperature of point B, T_B, as a function of the superheat of Alloy1 over its liquidus temperature (T_1-T_{L1}) for a mixing rate of 167 gs^{-1} and 113 gs^{-1}, respectively; wherein it could be observed that the location of point B depends on the superheat of Alloy1.

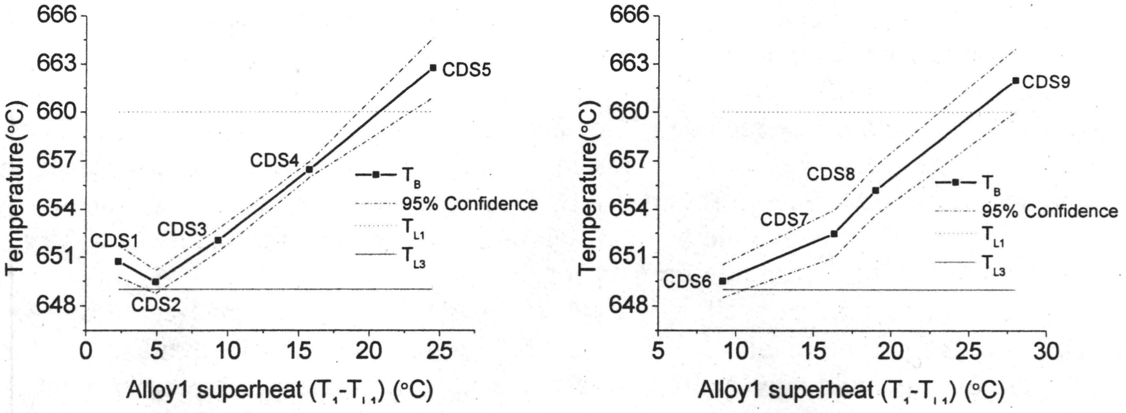

(a) (b)

Figure 6-8: Temperature at point B, T_B, as a function of superheat of Alloy1 above its liquidus temperature (T_1-T_{L1}); for the various experiments shown in Table 5-1. (a) CDS1 to CDS5 with mr6 and mixing rate of 167 gs^{-1} and (b) CDS6 to CDS9 with mr6 and mixing rate of 113 gs^{-1}. Also, shown are the liquidus temperatures T_{L1} and T_{L3}, and the 95% confidence interval for the data.

The value of T_B depends on four parameters: time of mixing Alloy1 into Alloy2, heat added into the resultant mixture from the enthalpy of Alloy1, heat added to the mixture by the heat of fusion resulting from the nucleation events of primary Al during mixing and heat loss to the environment from the resultant mixture. The time of mixing of Alloy1 into Alloy2 is fairly constant for a specific mixing rate and the heat loss to the environment could be assumed as nearly constant since the amount of the resultant alloy is fairly constant for all the experiments in Table 5-1 and the ambient temperature was nearly constant as well. Hence, the variation in the value of T_B would primarily be due to the variation in the heat added to the mixture during mixing from the enthalpy of Alloy1 and the nucleation reaction, alike. If there were no nucleation events of the primary Al phase from Alloy1 in the resultant mixture during the segment AB, then the higher initial temperatures of Alloy1, T_1 would have higher enthalpy values; hence, T_B should increase with higher values of T_1 (higher enthalpy of Alloy1). If there are nucleation events in the resultant mixture during mixing, then enthalpy of fusion would be released into the mixture from these events and thereby increase the heat content of the mixture, thereby, increasing the value of T_B. The higher the number of nucleation events, the higher would be T_B; and the amount of nucleation events would increase when the temperature T_1 decreases for a constant value of T_2 because the lower superheat of Alloy1 would result in a higher number of nucleation events for the same rate of heat extraction by Alloy2 during mixing. In Figure 6-8(a) for the higher mixing rate, the value of T_B decreases between the superheat temperatures of 2 and 5 °C because of the copious nucleation events at the lower superheat adding heat of fusion to the mixture to result in a higher value of T_B. After the superheat of 5 °C, the value of T_B steadily increases due to the high enthalpy of Aloy1 with increasing superheat temperatures and nominal nucleation events. In Figure 6-8(b), the smaller funnel diameter to effect a lower mixing rate of the alloys prevented use of superheat temperature Alloy1 lesser than 7 °C due to the higher surface tension and viscous forces preventing the melt of Alloy1 to flow through the small orifice of the funnel. Hence, the initial decrease in T_B, as observed in Figure 6-8(a) could not be recorded. However, the lower mixing rate also shows a steady increase in the value of T_B with increasing superheat temperatures of Alloy1. If there were no nucleation events in segment AB, T_B would show a direct proportionality with respect to (T_{L1} - T_1), and would not show an initial inverse proportionality as observed in Figure 6-8(a). A similar trend of proportionality between T_B and (T_{L1} - T_1) was observed for the mass ratio mr3 as well. Figure 6-9 shows the typical thermal curve during the CDS process for experiments CDS1 to CDS5 (Table 5-1); where the trend shown for T_B in Figure 6-8 (a) could be visually observed and further, the temperature after point B (as shown by the magnified section of the thermal curve in Figure 6-9) is highest for CDS1 (lowest T_1) and progressively decreases as T_1 increases from CDS2 to CDS5 showing that the recalescence from the release of the enthalpy of fusion is highest in CDS1 with lowest T_1 and continuously increases with increasing T_1 between CDS2 and CDS5. In Figure 6-10 shows the same thermal curve shown in Figure 6-9 except that the magnified section is on events prior to point B to show that the rate of temperature increase is lower for lower superheat of Alloy1 (T_1-T_{L1}), because of the larger enthalpy of fusion released from the increased nucleation events at lower alloy superheat temperatures.

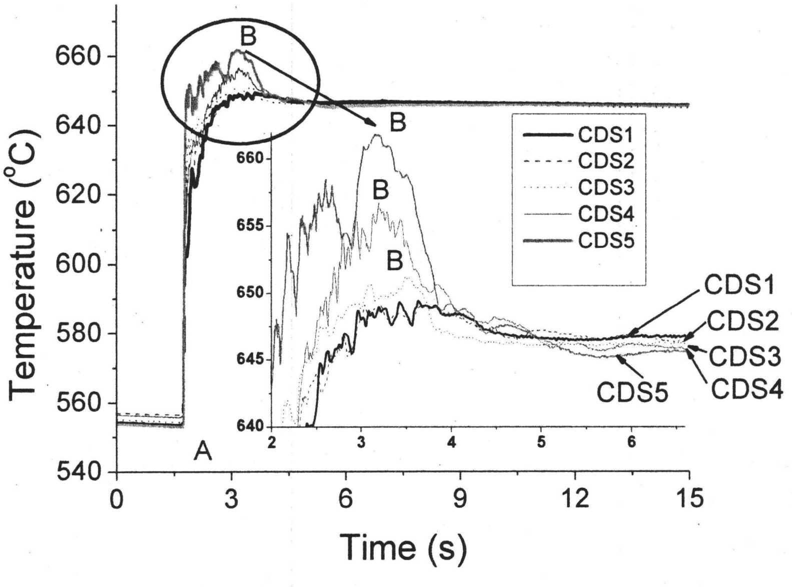

Figure 6-9: Thermal data of CDS experiments for mr6 at a mixing rate of 167 gs^{-1}.

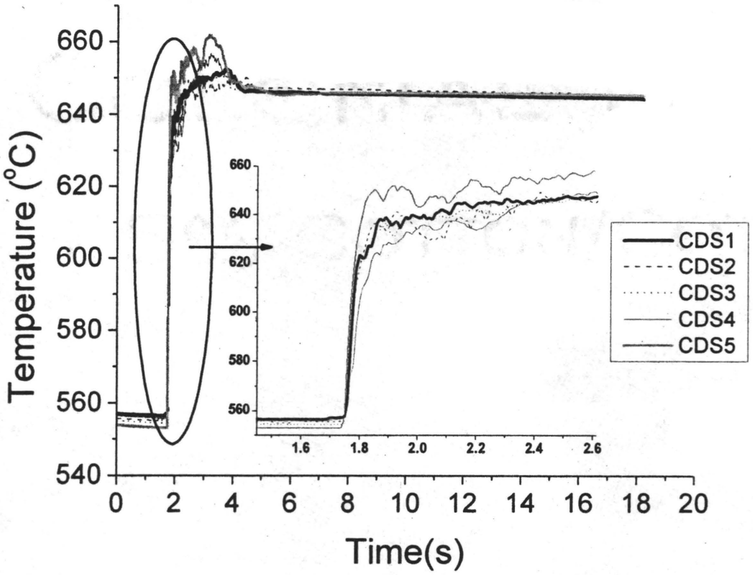

Figure 6-10 Typical thermal data of CDS process experiments involved in Table 5-1 of mr6 at various T_1 and mixing rate of 167 gs^{-1}.

The above-mentioned discussion along with the results shown in Figure 6-8 and Figure 6-9 provide the evidence of copious nucleation events occurring during the mixing process shown by segment AB in Figure 6-4. However, there are three alloys playing an active role during process: Alloy1, Alloy2 and Alloy3; and the source of the primary Al phase nucleating during mixing would have to be from one of these sources. The thermal data from the laboratory CDS experiments described in Section 5.1.2.1 along with samples from the rapid interrupted quenching experiments with the ribbon casting equipment as described Section 5.2.1, were analyzed to determine the source of the primary Al nucleation during mixing.

Figure 6-11 shows a plot developed from the thermal data for the experiments CDS1 to CDS5 and the instantaneous rate of mixing during each experiment. The instantaneous rate of mixing was evaluated during the mixing process from the start at point A to the end at point B; and a plot between the changes in the Cu concentration in the resultant mixture as a function of time of mixing was generated. This plot was compared to the thermal data between temperature and time of mixing and a new plot between Cu concentration and temperature was generated as show in Figure 6-11.

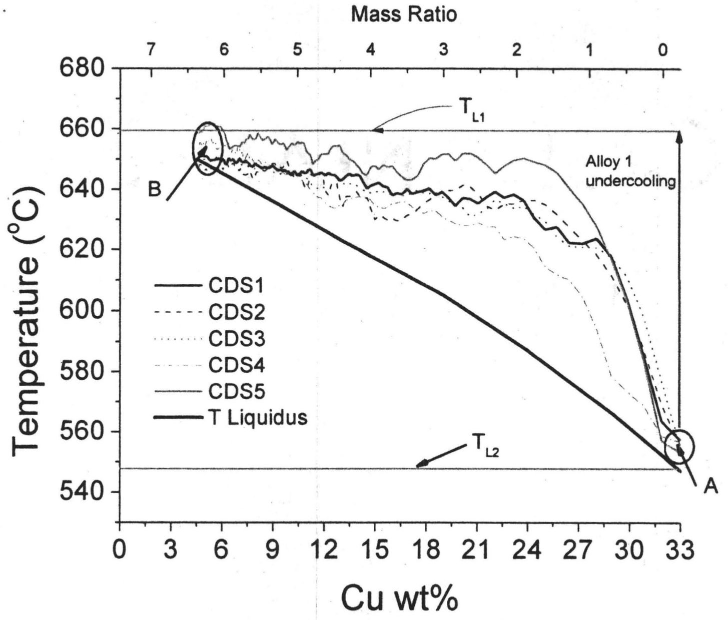

Figure 6-11 The thermal data of CDS experiments superimposed on the rate of change of Cu concentration and instantaneous liquidus temperature of the mixture.

An additional abscissa was added to Figure 6-11 to illustrate the changes in mass ratio as a function of temperature, as well. In Figure 6-11, the temperature data between the start of mixing at point A and the end of mixing at point B is shown for the various values of T_1; and during any stage of the mixing process the temperature of the resultant mixture is lower than the liquidus temperature of Alloy1, T_{L1} and higher than that for Alloy3, T_{L3}. Further, during the mixing process, the Cu concentration does not equalize in the melt and stream of Alloy1 would be broken into smaller drops in the resultant mixture as would be validated by results subsequently in this section. These drops of Alloy1 would reside in an significantly undercooled environment at all times effecting in the nucleation of the primary Al phase from the distributed drops of Alloy1 in the resultant mixture [24]. The mixture temperature at any stage of mixing in Figure 6-11 is higher than the liquidus temperature of Alloy2, T_{L2} and hence, there would not be any nucleation of the primary phase from Alloy2. Similarly, there would not be any nucleation from Alloy3 as well because the Cu (solute) of the resultant mixture would not have equalized to obtain a homogeneous Alloy3 and further, the mixture temperature is higher than T_{L3} at all stages of the mixing process. Since, the phase diagram of the Al-Cu system is simple binary as shown in Figure 5-2 between 0 and about 50 wt% Cu, the only nucleation phase in any Cu concentration in this range would be that of the primary Al phase at the respective liquidus temperature.

To further validate that the nucleation of the primary Al phase during mixing takes place from Alloy1, the samples from the interrupted rapid quenching experiments with the ribbon casting equipment described in Section 5.2.1 and Table 5-2 were analyzed.

Figure 6-12 shows typical low magnification microstructure of the surface of the quenched ribbons for the various experiments shown in Table 5-2: CDSQ1 to CDSQ10; and CONVQ1 and CCONVQ2. All the samples quenched after the initial mixing in the CDS process: CDSQ1 to CDSQ10 showed distinct nucleation of the primary Al phase as exhibited by the existence of blocky particles of Al in the microstructure. In samples quenched from a conventional Al-4.7 wt% Cu alloy maintained at a 5 °C above the liquidus temperature (CONVQ1 and CONVQ2) did not show any evidence of such blocky Al phase particle showing the absence of a significant nucleation and growth event prior to the quenching or during the quenching process. Further, the results of CONVQ1 and CONVQ2 in Figure 6-12 also confirm that the nucleation and growth of any primary phase during quenching is not evident and hence, it would be assumed with reasonable confidence that the nucleation and growth of primary Al phase show in samples from CDSQ1 to CDSQ10 occurred prior to quenching during the mixing stage.

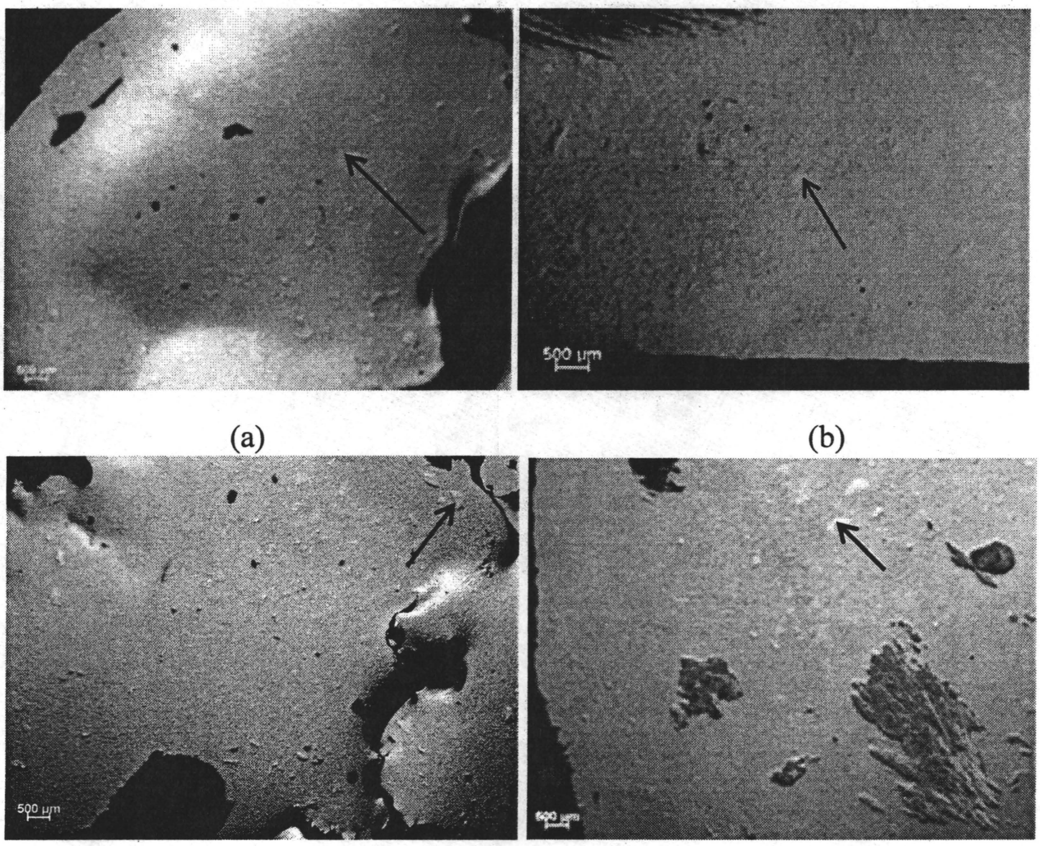

(a) (b)

(c) (d)

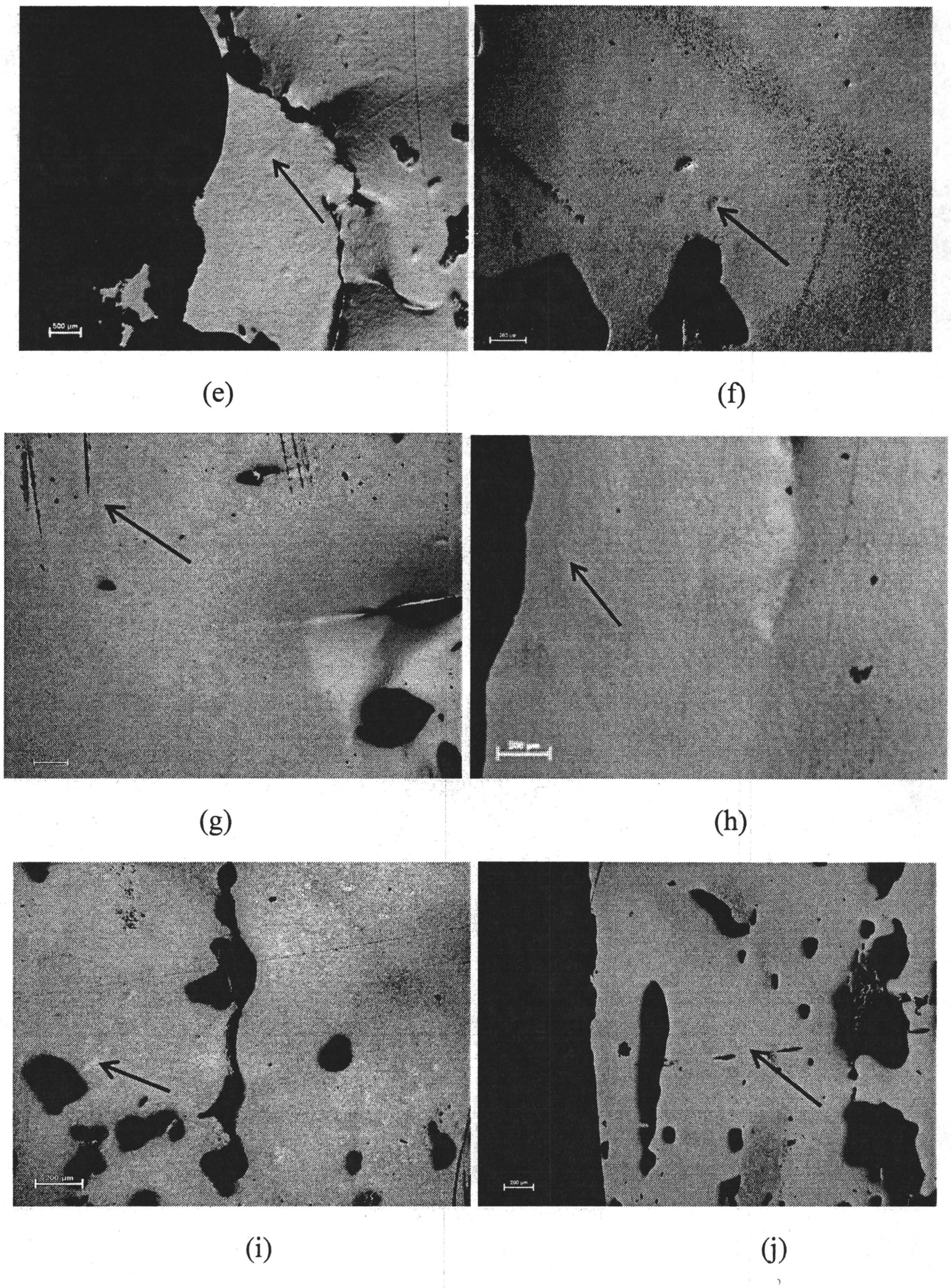

(e) (f)

(g) (h)

(i) (j)

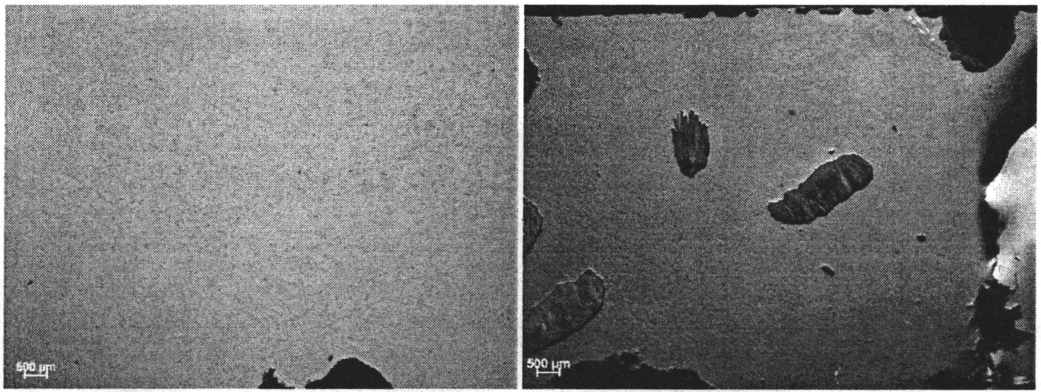

(k) (l)

Figure 6-12 Typical low magnification microstructure obtained from the surface of the rapid quench ribbon (Table 5-2) from an optical stereo microscope. (a) CDSQ1 (mr6), (b) CDSQ2 (mr6), (c) CDSQ3(mr3), (d). CDSQ4 (mr3) (e) CDSQ5 (mr6), (f), (g) CDSQ6 (mr6), (h) CDSQ7 (mr6), (i) CDSQ8 (mr3), (j) CDSQ9 (mr3), (k) CDSQ10 (mr3) CONVQ1 (mr6), (l) CONVQ2 (mr3). The arrows in the microstructure show the blocky Al phase particle; and the blocky dark and rugged particles are the loose bakelite used in sample mounting compound.

Further, Figure 6-13(a) and (b) show the microstructure of typical blocky Al phase particle that nucleated and grew during the mixing stage as shown in Figure 6-12, for the samples from the CDSQ1 and CDSQ3 show in Table 5-2, respectively. The microstructures in Figure 6-13 are the bright field secondary electron images obtained in a SEM and the Figure 6-13 (c) and (d) show the line scan profile obtained using energy dispersive x-ray analysis for the lines drawn across the microstructure in Figure 6-13 (a) and (b), respectively. The composition of Cu at any location in the blocky Al phase particle is nearly zero, thus, confirming that these phase particles nucleated from the Alloy1. If they were to nucleate from Alloy2 or Alloy3, there would be a segregation of Cu across the primary Al phase and the average composition would reflect the respective Cu concentration as dictated by the phase diagram.

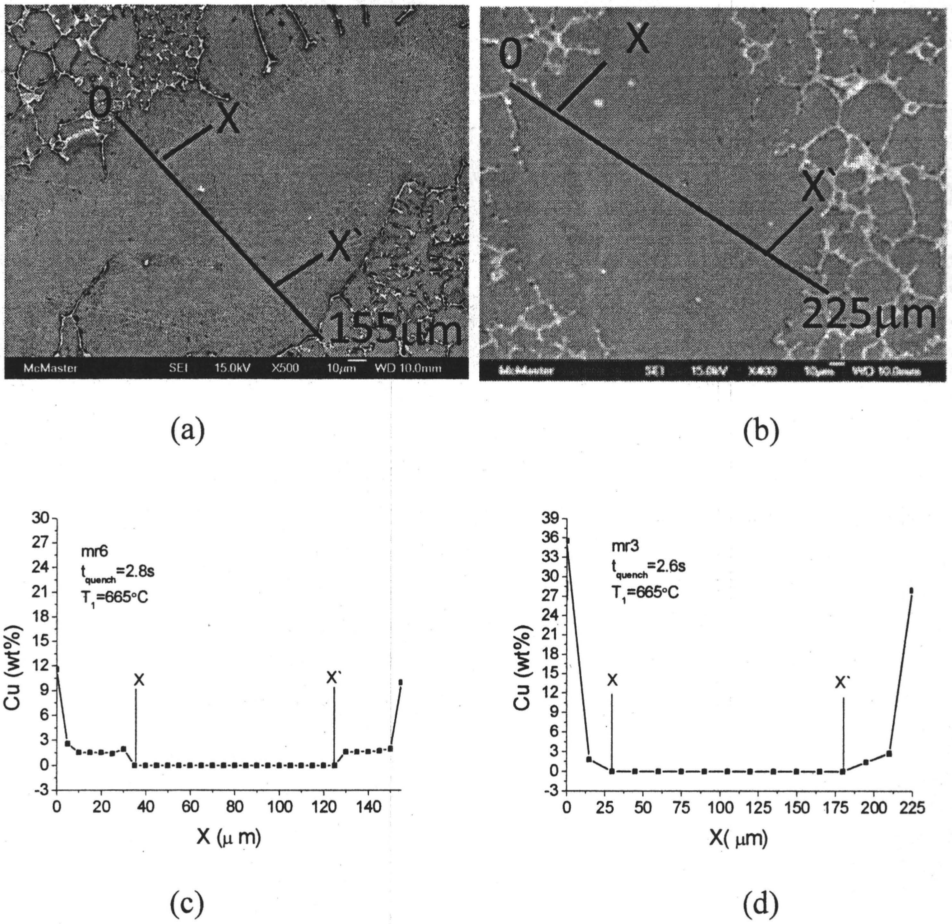

(a) (b)

(c) (d)

Figure 6-13 Typical secondary electron images taken in an SEM and typical line-scan data of solute (Cu) concentration taken across the primary nucleated phase. (a) SEM image for CDSQ1 (mr6), (b) SEM image for CDSQ3 (mr3), (c) Cu concentration for CDSQ1 and (d) Cu concentration for CDSQ3.

The results shown in Figure 6-8 to Figure 6-13 validates the claim that the primary Al phase from Alloy1 undergoes copious nucleation during the mixing stage between points A and B in Figure 6-4.

In above-mentioned discussion, it was mentioned that the stream of Alloy1 mixing with Alloy2 would breakdown and distribute as several smaller drops of Alloy1 in the resultant mixture causing the favorable environment for copious nucleation of the primary Al phase from Alloy1. The results of experiments with water (with blue ink) mixing with water and the numerical simulations to understand the transient density distribution during mixing were analyzed to arrive at this conclusion.

Figure 6-14 shows two snapshot photographs obtained from the digital video recording obtained during the mixing of water with blue ink poured through a funnel at about 167 gs^{-1} into a beaker with water as described in Section 5.1.1.1. This figure shows the break-up of the stream of water with ink (shown by circles in Figure 6-14) as it enters the resultant mixture and the distribution of the broken phase in the resultant mixture.

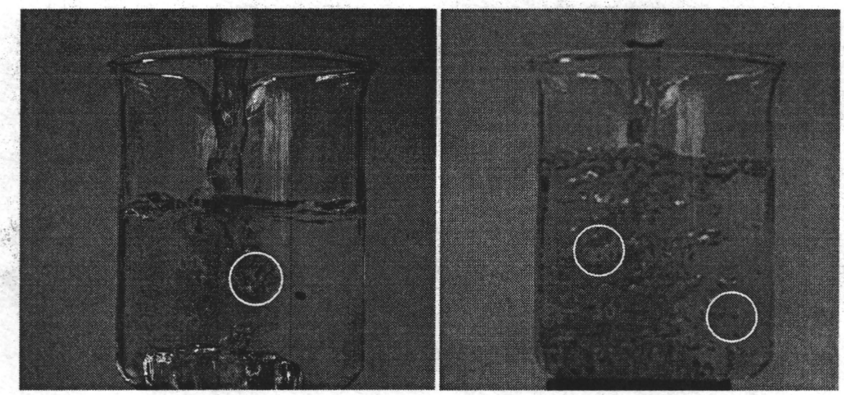

(a) (b)

Figure 6-14 Snapshot photographs taken during the mixing of Water with blue ink with water to show the progressive break-up of the stream of water with blue ink in the resultant mixture. (a) after 0.7s and (b) after 1.3s.

Figure 6-15 shows the snapshot images (after 0.2, 0.5, 1 and 1.5 s into the mixing process and around point B at 2.4s of transient density distribution obtained from the numerical simulations described in Section 5.3.1. The setup of the simulation mirrored that of the laboratory CDS experiment, CDS1 (Table 5-1) shown in Figure 6-9, to ensure a valid interpretation of the results. Figure 6-15 show that the stream of Alloy1 instantaneously effects a marked gradient in the density distribution of the resultant mixture showing that the stream would have to break down to re-distribute in the mixture throughout the mixing process. Further, Figure 6-15 (e) shows that there is a significant density gradient between 2.375 g/cc (pure Al) and 2.464 g/cc (Al – 5.15 wt% Cu) in the resultant mixture at around point B suggesting that the thermal and solute fields do not homogenize at the end of the mixing stage denoted by AB in Figure 6-4.

The results and analysis of Figure 6-14 and Figure 6-15 show that, during the mixing process, the stream of Alloy1 would break-up and distribute as separate packets of liquid in the resultant mixture at a significantly undercooled temperature with respect to T_{L1}, resulting in a favourable environment for the copious nucleation of the primary Al phase from Alloy1 during mixing.

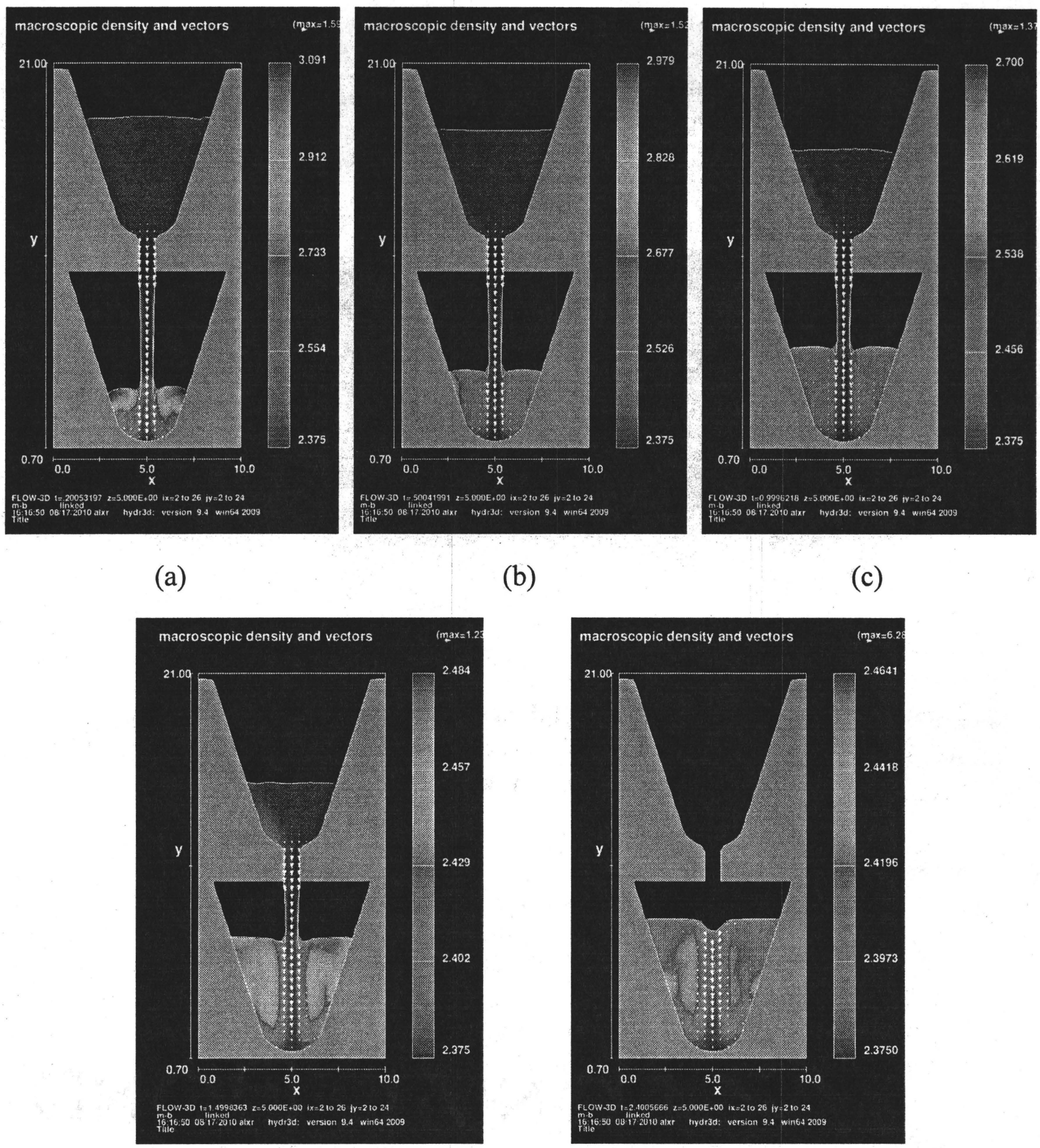

(a) (b) (c)

(d) (e)

Figure 6-15; Snapshot images of transient density distribution obtained from the numerical simulation experiments described in Section 5.3.1 to show that the stream of Alloy1 would break-up during the mixing process. (a) to (d) after 0.2, 0.5, 1, 1.5 s of mixing, respectively, (e) around point B for CDS1 at 2.4 s.

There were two mixing rates of 167 gs^{-1} and 113 gs^{-1} adopted in the laboratory CDS experiments described in Section 5.1.2.1 and Table 5-1. The extent of break-up of the stream of Alloy1 mixing into Alloy2 would depend on the rate of mixing and a greater break-up of the stream of Alloy1 would result in a higher number and distribution of the packets of liquid of Alloy1 in the resultant mixture, resulting in a higher number of nucleation events which is more favorable for a successful CDS process. The Weber number, N_{we} is described as the ratio between the inertial forces to the surface tension of the liquid [118]; and this number described the propensity of the break-up of a flowing stream into packets of liquid. The higher the value of N_{we}, the higher is the propensity of break-up of the stream. Equation 6-1 presents the equation to evaluate N_{we}; wherein ρ, L, u and σ are the bulk liquid density, characteristic length, velocity of the stream and surface tension of the liquid, respectively. The characteristic length is the diameter of the stream

Equation 6-1

$$N_{we} = \frac{\rho\, L\, u^2}{\sigma}$$

Table 6-1 shows the values of N_{we} for the two mixing rates; wherein N_{we} is markedly greater for the lower mixing rate of 113 $g.s^{-1}$ than that for the higher rate of 167 $g.s^{-1}$. These results suggest that the stream of Alloy1 mixed with a lower mixing rate would break-down more than that with the higher mixing rate and result in higher number and distribution of packets of Alloy1 in the resultant mixture there by effecting higher number of nucleation events during mixing in the CDS process with the lower mixing rate.

Table 6-1: Weber number, N_{we} evaluated for the Alloy1 (pure Al) for two rate of mixing (167 and 113 gs^{-1}).

Alloy	Mixing Rate ($g.s^{-1}$)	u ($m.s^{-1}$)	L (m)	ρ ($kg.m^{-3}$)	σ ($N.m^{-1}$)	N_{we}
Alloy1 (Pure Al)	167	1.1	9E-3	2375 [111]	0.868 [22]	30
	113	1.68	6E-3			46.4

If the preceding argument of higher number of nucleation events for a slower mixing rate is valid then there would be a larger amount of enthalpy of fusion released during the mixing process in the lower mixing rate condition. Figure 6-16 (a) to (c) shows the typical thermal data obtained from the laboratory CDS experiments shown in Table 5-1 of Section 5.1.2.1; wherein the individual plots compare the thermal data in the segment AB for the two respective rates of mixing for experiments with mr6. Figure 6-16 (d) shows the plot of the time taken for segment AB, t_{AB} as a function of the superheat temperature of Alloy1, (T_1-T_{L1}), similar to that shown in Figure 6-8. For a given value of T_1, T_2 and mass ratio of the CDS process, the value of t_{AB} is higher for the lower rate of mixing of 113 $g.s^{-1}$ as compared to the higher rate of 167 $g.s^{-1}$, showing that the increased amount of the enthalpy of fusion released from the higher number of nucleation events in the case of the lower mixing rate resulted in the higher value of t_{AB}. In Figure 6-16 (a) to (c) the lower rate of increase in temperature between points A and B for the lower rate of mixing shows that there is more heat added (enthalpy of fusion) to the mixture from the higher number of nucleation events.

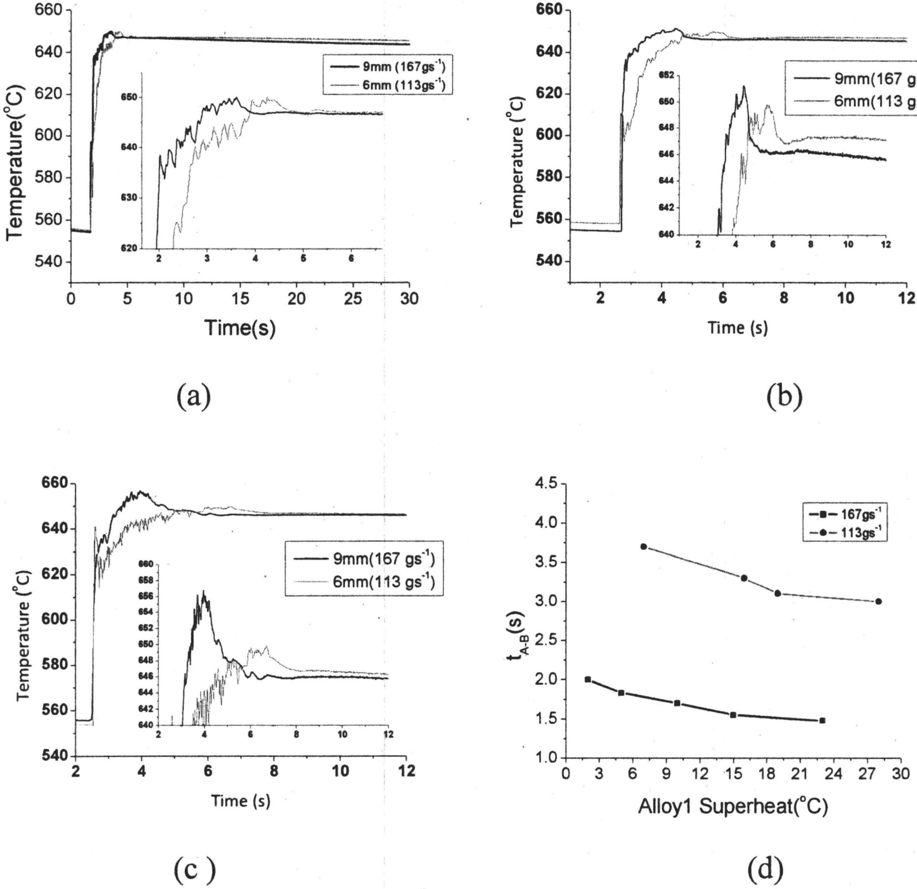

(a) (b)

(c) (d)

Figure 6-16: Typical thermal curve from the laboratory CDS experiments in Table 5-1 of Section 5.1.2.1 for a mass ratio of mr6 to compare the effect of the two rates of mixing. (a) CDS1 vs CDS6, (b) CDS4 vs CDS7, (c) CDS5 vs CDS8 and (d) plot of t_{AB} as a function of superheat temperature of Alloy1, (T_1-T_{L1}) from (a) to (c).

The results presented in this section on the events occurring during the mixing stage shown by segment AB in Figure 6-4 of the CDS process could be summarized as follow:

- Nucleation event takes place in the resultant mixture.
- The primary Al phase from Alloy1 nucleates in the mixture.
- Absence of homogenization of the thermal and solute fields.
- Increased number of nucleation events at the lower mixing rate.

6.2.2 Re-Distribution of Thermal and Solute Fields, and Nucleation - *Segment BCD*

In the CDS process, the thermal and solute fields at the end of the mixing stage (point B) results in a unique and favorable re-distribution of these fields in the segment BCD in Figure 6-4 and sets the stage for the solidification of Alloy3 with a non-dendritic morphology of the primary phase. In this section, the unique re-distribution of the thermal and solute fields would be presented, discussed and validated with experiment results.

The following five events occur in the resultant mixture of Alloy3 in the segment BCD of Figure 6-4, the events have been numbered continuously from the events during the mixing stage described in Section 6.2.2. The Event 4 in the mixing stage continues on into segment BCD and hence this event is listed again in this section as the first event.

Event (4) *Re-distribution of thermal and solute fields* in the macro-scale
Event (5) *Formation of cells* in the micro-scale with lower Cu concentration on the middle of the cell and higher Cu concentration in the cell boundaries.
Event (6) *Re-distribution of thermal and solute fields inside cells* in micro-scale.
Event (7) *Nucleation of primary Al phase inside cells.*
Event (8) *Final nucleation event* at point D from the pockets of liquids with nearly homogeneous Cu concentration.

The following sub-section would describe the above-mentioned events in greater detail.

6.2.2.1 Redistribution of Thermal and Solute Fields in Macro-Scale

This stage (Segment BCD) has been designated as stage II in Figure 6-4; wherein the re-distribution of the thermal field would be nearly complete in stage IIa (Segment BC) and that of the solute field in stage IIa and IIb combined (Segment BC and CD).

The temperature filed would re-distribute at a faster rate than the solute field due to the significantly higher value of the thermal diffusivity as compared to the diffusivity of the solute mass. The temperature field in the resultant mixture would equalize at some point between the points B and D; and denoted as point C in Figure 6-4. The location of point C is not very critical for a successful CDS process and it is satisfactory as long as it exists between points B and D. The location of point C depends on a number of independent parameters such as the initial mass ratio of mixing, rate of mixing, geometry of the crucible in which the alloys are mixed, initial temperatures of the precursor alloys. It is noteworthy to mention that the temperature field inside the resultant mixture of Alloy3 at around point B (end of mixing stage) is such that the temperature at the bottom is higher than that in the top as observed in Figure 6-5 and Figure 6-6. Figure 6-17 shows the typical thermal curves for the laboratory CDS experiments with mr6: CDS2 to CDS5 (Table 5-1). In Figure 6-17, it can be observed that the temperature of point C decreases with decreasing superheat temperatures of Alloy1 (T_1); in other words, the location of point C moves away from point B and towards point D as T_1 decreases because the equalization temperature between the two thermocouples measuring the temperature at the bottom and top of the mixture would be higher for higher initial difference in the temperatures of the precursor alloys.

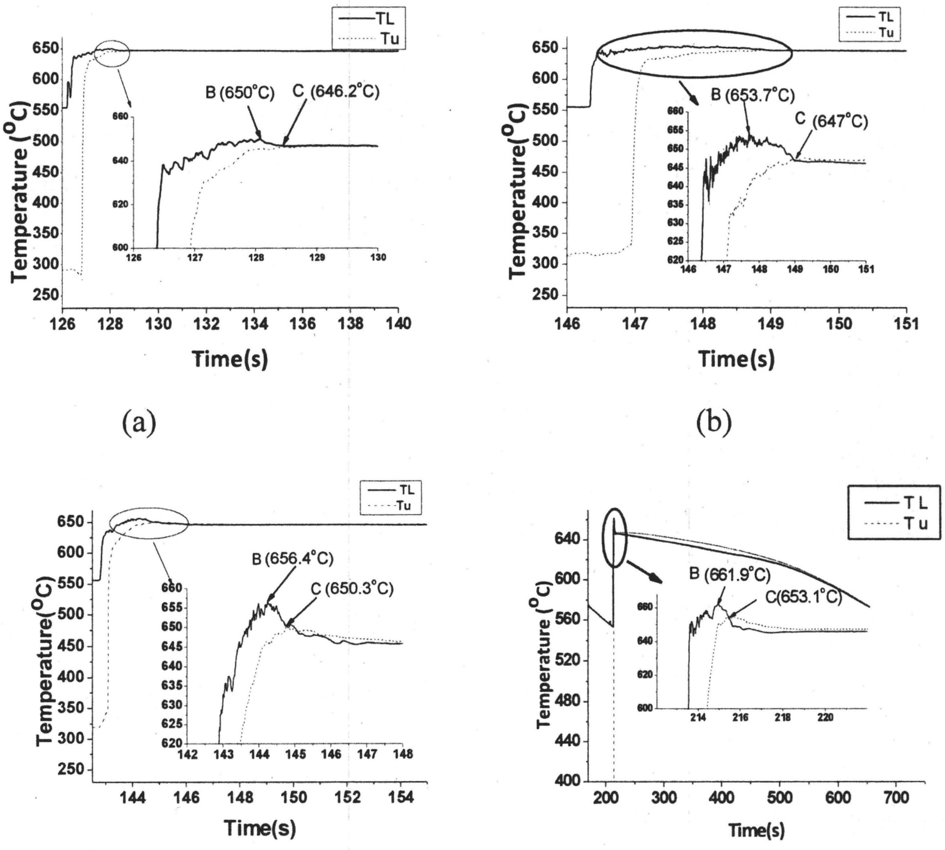

(a)

(b)

(c)

(d)

Figure 6-17 Typical thermal curves for laboratory CDS experiments of mr6 with a mixing rate of 167 gs^{-1} showing the effect of T_1 for Alloy1 on the equalization of temperature between points B and C. (a) T_1 = 665 °C, (b) T_1 = 670 °C, (c) T_1 = 675 °C and (d) T_1 = 683 °C.

The solute field would take longer to equalize in the mixture and typically the equalization of the solute field would take place near point D.

Figure 6-18 represents an image of the 2D simulation quantified by flow 3D software showing, that between point B and C, the density at the bottom of the mixture is lower than that at the top. Figure 6-18 (a) and (b) are snapshot images taken after 2.8 s and 3.3 s from the start of the mixing process, respectively; the point B was around 2.4 s. The density gradient of the solute after 2.8 s, as shown by Figure 6-18 (a), is between 2.394 and 2.4529 g/cc which is equivalent to a solute gradient of 1.15 and 4.7 wt% Cu, respectively. This is less than the gradient observed at point B of between 0 and 5.15 wt% Cu as shown in Figure 6-15 (e)

The Cu concentrates at the top of the mixture and gradually distributes toward the bottom. Thus one could predict from the figure that the temperature at the bottom of the crucible would be greater than that at the top since an alloy at lower Cu concentration settles at the bottom. The density distribution after mixing also suggests that the largest amount of nucleation event occurs at the bottom and lowest at the top with a continuous gradient of nucleation event form the bottom to the top. It follows that; the enthalpy of fusion released would be highest at the bottom and lowest at the top with a continuous gradient of release from the bottom to the top. These results confirm the results deduced from the thermal data shown in Figure 6-9and Figure 6-10.

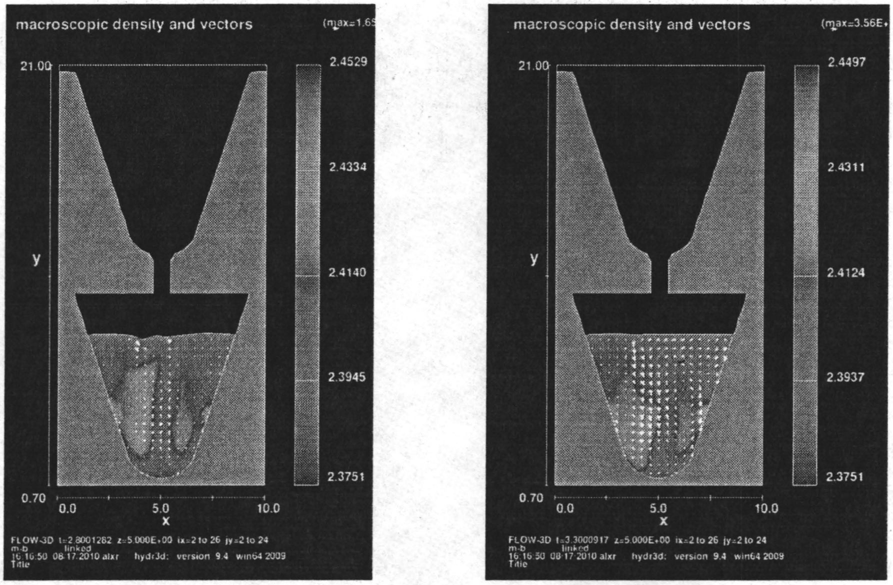

(a) (b)

Figure 6-18 Transient density distribution from the numerical simulation of the mixing of Alloy1 into Alloy2 in the CDS process after ending of mixing. (a) after 2.8s of mixing and (b) after 3.3s. The visual scale for quantified macroscopic density (g/cc) is presented as well.

6.2.2.2 Formation of Cells in the Micro-Scale

During the residence time in Segment BCD shown in Figure 6-4, cells in the micro-scale form inside the resultant mixture of Alloy3 and these cells are akin to the Bernard cells and described in Section 4.3. The cells form due to the difference in the density, temperature and surface tension between Alloy1 and Alloy2. The Alloy1 predominantly form the inside of the cells and Alloy2 forms the boundary.

The results from the interrupted rapid quenching experiments of the ribbon casting equipment as described in Section 5.2.1 and Table 5-2 showed ample evidence to support the proposal of cell formation. Typical there are three distinctly unique areas in the microstructure of samples quenched from a location in segment BCD; namely, *Area1, Area2 and Area3*. Figure 6-19 show typical microstructure of samples obtained with an optical microscope from the interrupted rapid quenching experiments described in Section 5.2.1 and Table 5-2 for CDSQ1 and CDSQ3 experiments showing the three areas in the microstructure. The Area1 is the large phase of primary Al phase nucleated during the mixing stage as described in Section 6.2.1, Area2 is composed of the cells formed in Segment BCD which are akin to the Bernard cells as described in Section 4.3 and Area 3 forms at the later stages of segment BCD when small pockets of liquid with homogeneous Cu concentration form.

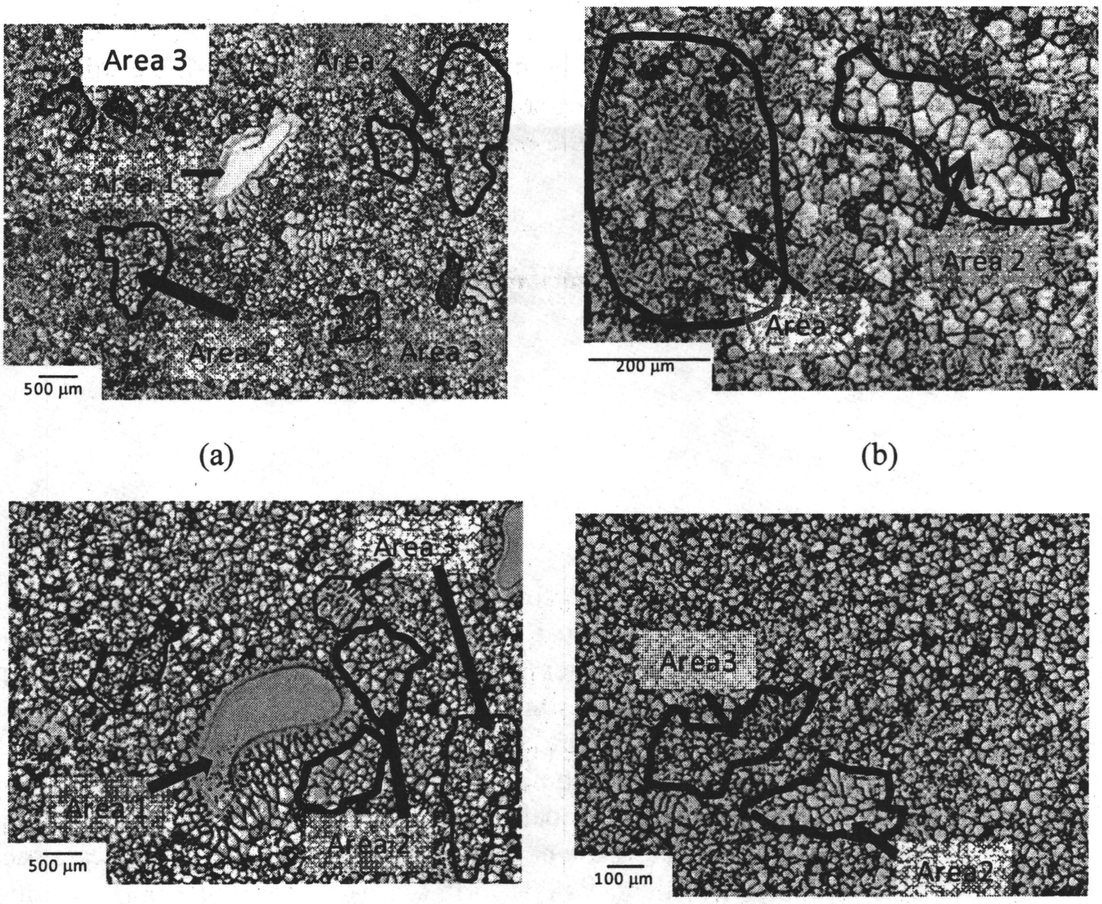

(a) (b)

(c) (d)

Figure 6-19: Typical optical micrographs showing the three typical and unique areas in the microstructure of samples quenching the segment BCD of Figure 6-4; namely, Area1, Area2 and Area3. (a) and (b) CDSQ1; and (c) and (d)CDSQ3.

In this section, the Area2 and Area3 would be presented and discussed in greater detail.

When Alloy1 with a higher thermal mass and lower density mix with Alloy2 with a lower thermal mass and higher density, an analysis of the Peclet Number, N_{Pe} would broadly define the re-distribution of both the thermal and solute fields in the resultant mixture. The expressions for N_{Pe} for the thermal and solute fields are presented in Equation 6-2 (a) and (b), respectively; and defined by the ratio of the rate of advection of a physical quantity by the flow to the rate of diffusion of the same quantity driven by an appropriate gradient. In other words, if the value of N_{Pe} is high (>>1), then the mixing process is dominated by the rate of advection; wherein the temperature or solute mass would move in the mixture along with the flow of the matrix material and result in a blended mixture with would not be fully homogenized in the micro-scale. Conversely, if the value is small (≤ 1) then the mixing process would be mixed and homogenized in the micro-scale because the diffusion of temperature and/or solute mass due to the gradient would occur simultaneously with the diffusion phenomenon.

Equation 6-2

$$N_{\mathrm{Pe}} = \frac{L\,u}{\alpha} \qquad \text{(a)}$$

$$N_{Pe} = \frac{L\,u}{D} \qquad \text{(b)}$$

presents the evaluated values of the N_{Pe} for both the thermal and solute fields for the laboratory CDS experiment with the two respective mixing rates adopted; wherein the former is in the order of 10^2 and the latter 10^6 (Table 6-2). Both the values of thermal and solute Peclet numbers are high suggesting that the mixture would blend in the macro-scale with marked gradients in temperature and solute mass in the micro-scale. Hence, a temperatures measured by the two thermocouples in the laboratory CDS experiments shown in Figure 5-4 would measure an equalized temperature at around point C in Figure 6-4 but there would be a significant gradient in the temperature in the micro-scale such as the centre and the boundaries of the cells that form the Area2 in Figure 6-19. Similarly, the numerical simulation results for density distribution show a nearly equalized solute concentration in the bulk mixture but there would be a significant gradient of the solute concentration between the boundary and centre of the cells (micro-scale) forming Area2 in Figure 6-19.

Table 6-2 Peclet number for thermal and solute diffusion at beginning of mixing

Mixing Rate (Kg/s)	L (m)	ρ (Kg/m^3)	u (m/s)	$(N_{Pe})_{Thermal}$	$(N_{Pe})_{Solute}$
0.167	0.009	2375	1.1	355	1.85E+06
0.113	0.006	2375	1.68	365	2.97E+06

The preceding results and discussion on the Peclet Number in the CDS process suggests that at the end of the mixing stage (point B), the temperature and solute fields would be nearly blended in the entire resultant mixture of Alloy3, however, there would exist significant gradients of temperature and solute in the micro-scale in the cells forming Area2 of the microstructure.

As described in Section 6.2.2, the cells that form Area2 in Figure 6-19 is such that the alloy with the lower surface tension forms the body of the cell and that with the higher surface tension would form the cell boundaries. Figure 6-20 shows that Alloy1 (pure Al) with a lower surface tension and form the bulk of the cells in Area2 and Alloy2 (Al-33Cu) with a higher surface tension would form the cell boundaries.

The individual cells in Area2 form with a large gradient of Cu concentration from the boundaries to the centre of the cell. This would result the re-distribution of the Cu solute with each cell driven by natural convection in the liquid and diffusion of the mass. The contribution to solute re-distribution by natural convection would be significantly higher than that by the diffusion mechanism because of the significantly large temperature (density) gradient between the cell boundary and centre, as well. Figure 6-21 shows line scan data of Cu concentration obtained from the energy dispersive x-ray analysis carried out in an SEM for several individual cells in Area2 for several cell sizes in samples obtained from the experiments CDSQ1 to CDSQ10 shown in Table 5-2. The abscissa for plots in Figure 6-21 were in dimensionless distance with the respective cell sizes in the legends to enable better visual comparison of the data with each cell. Figure 6-21 shows that the average composition of Cu inside the cells do not depend on the cell size for each experiment condition because the re-distribution of the Cu mass inside the cells are controlled by the natural convection rather than the mass diffusion process and hence, the size of the cell do not affect the re-distribution since the Cu mass is carried by advection throughout the entire cell resulting in a near uniform concentration in the bulk of the cell for each experiment condition. Further, there is difference in the Cu concentration on the boundaries of the cell for various cell sizes in each experiment condition, independently because of two reasons: the thickness of the boundary of alloy with higher Cu content during the formation of the cell would vary and the mass conservation would typically dictate the smaller cells would generally have a higher Cu content at the boundaries if the Cu in the centre bulk were to be the same.

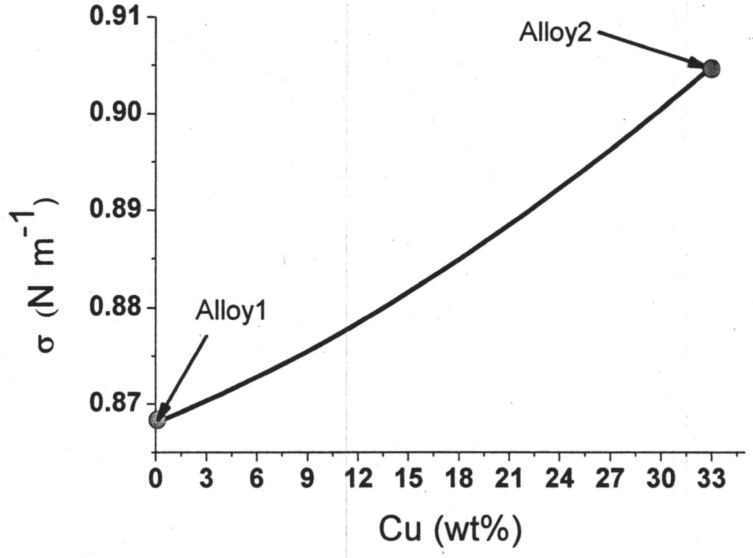

Figure 6-20 Plot of Surface tension as a function of Cu concentration for the Al-Cu binary alloy [22].

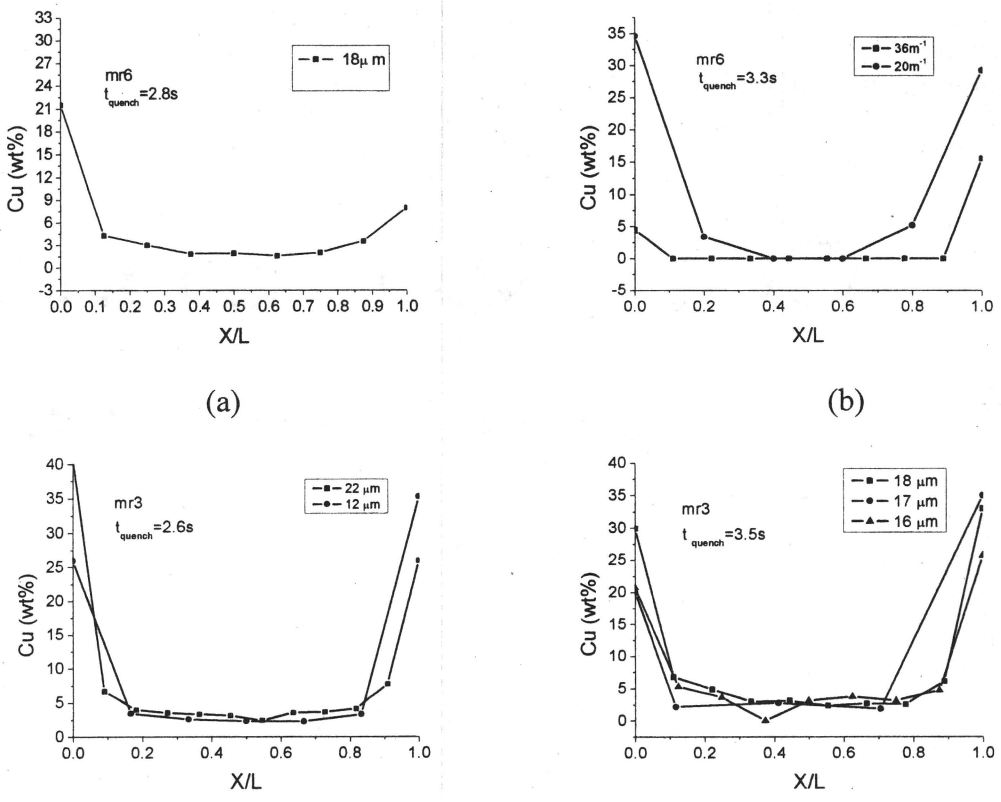

(a) (b)

(c) (d)

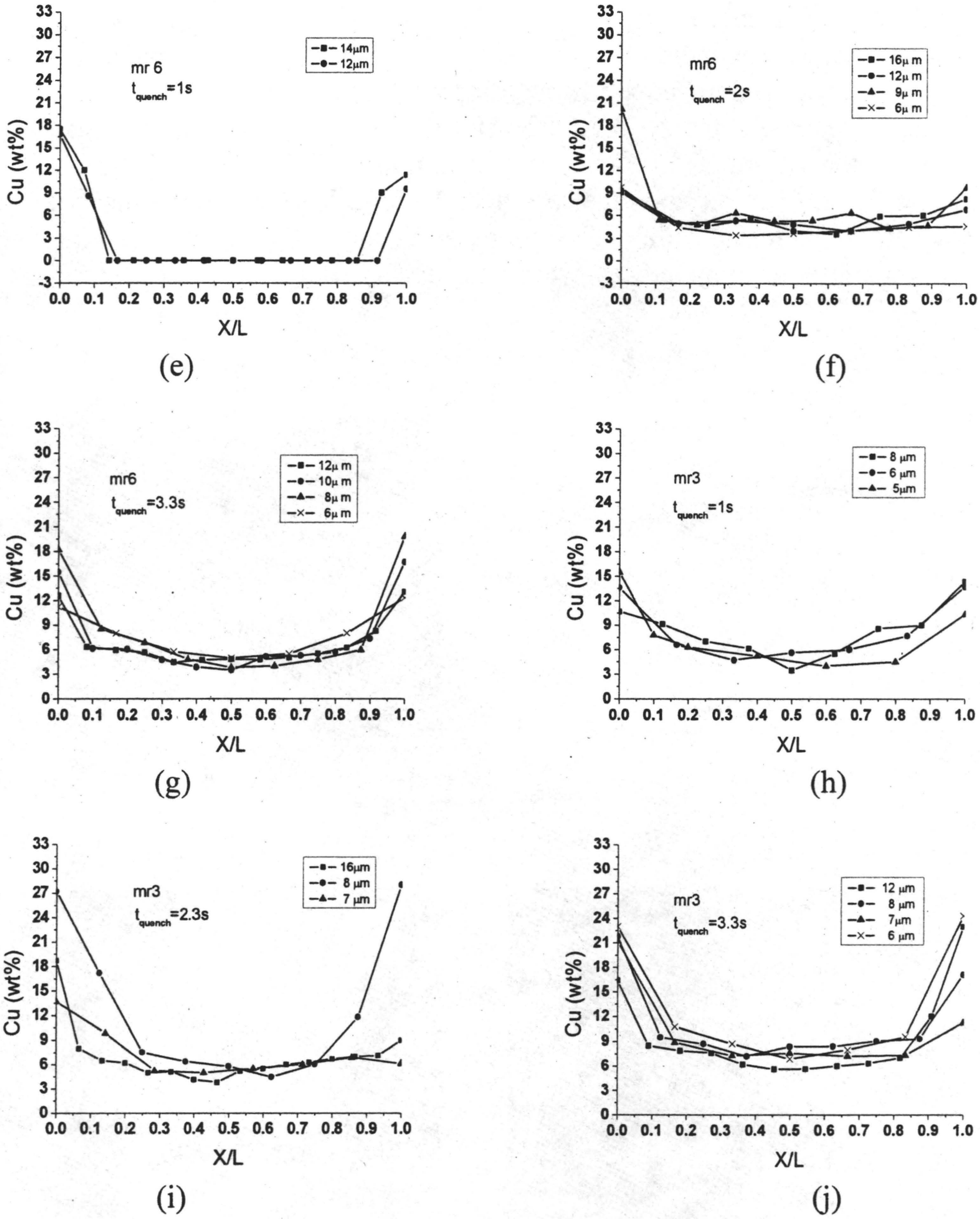

(e) (f)

(g) (h)

(i) (j)

Figure 6-21: Line scan data of Cu concentration from energy dispersive x-ray analysis in an SEM for random lines drawn across individual cells (various size) in Area2 in samples from the various experiments shown in Table 5-2. (a) to (j) CDSQ1 to CDSQ10, respectively. The abscissa in the plots were dimensionless distances to enable visual comparison of data.

The size of the cells in Area2 would depend on the initial mass ratio in the CDS process. Figure 6-22 (a) shows the quantified data for the cell size as a function of the initial mass ratios for experiments in Table 5-2; wherein the average cell size increases with increasing mass ratio because at lower mass ratios, the amount of Alloy2 with the higher surface tension is higher causing the evolution of smaller cells with a larger gradient of Cu concentration within them. Figure 6-22 (b) to (d) shows the typical microstructure obtained from optical microscope for the samples with mr3, mr4.5 and mr6, respectively, showing an increasing cell size in Area2 with increasing mass ratio. The size of the cell in Area2 and the resultant difference in the gradient of Cu concentration within them would significantly affect the nucleation and solidification inside the cells and the resultant microstructure of the CDS process; further, this would also influence the optimization of the parameters as would be discussed in subsequent sections of this chapter.

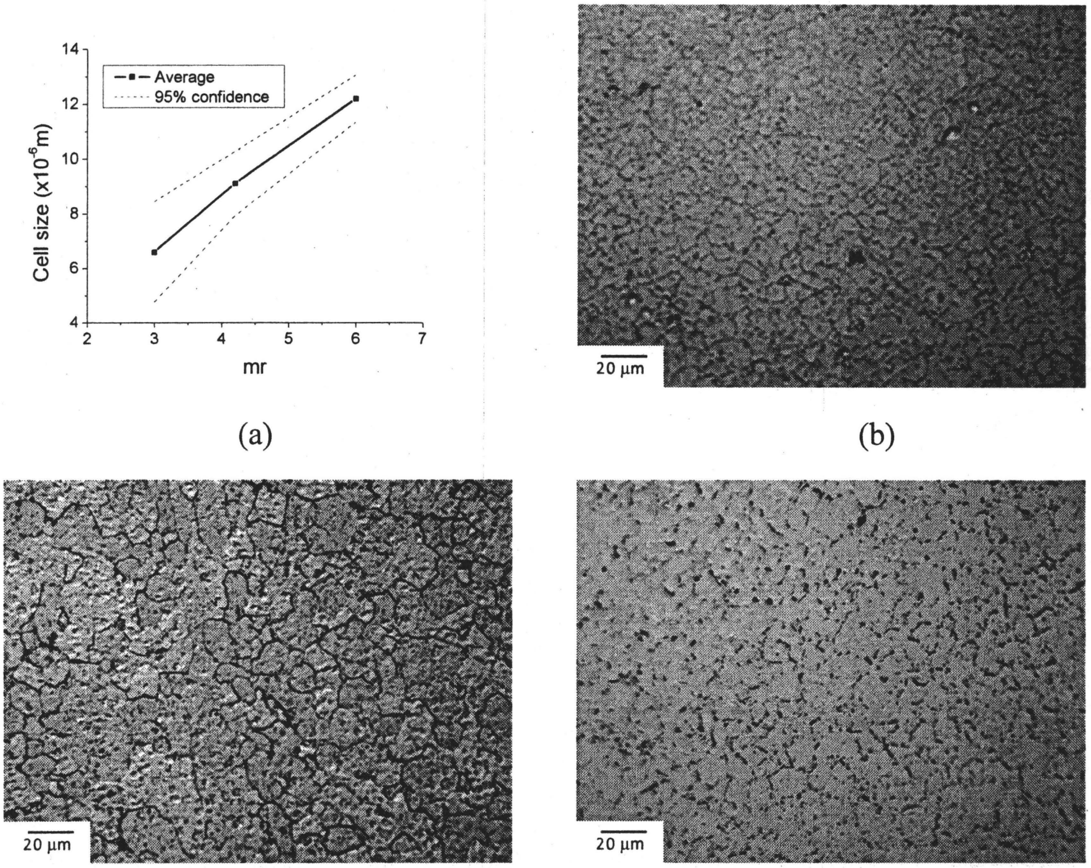

(a) (b)

(c) (d)

Figure 6-22: Quantified size of cells forming Area2 in samples from the three different initial mass ratios and a constant T_1 of 669 °C for experiments shown in Table 5-2. (a) average data with 95% confidence intervals, (b) mr3 (CDSQ9), (c) mr4.3 (CDSQ11) and (d) mr6 (CDSQ6).

Figure 6-23 shows the profile of the Cu concentration within the cells obtained from the line scan data in the SEM showing the higher gradient of Cu concentration inside the cell for the lower mass ratio of mr3 for cell with the same size in each of the two mass ratios. Also, the figure shows that with increasing time the gradient of Cu concentration decreases with the cell but the difference in the gradient still exists for the two different mass ratios because of the higher amount of initial Cu at the cell boundaries in the case of lower initial mass ratio, mr3.

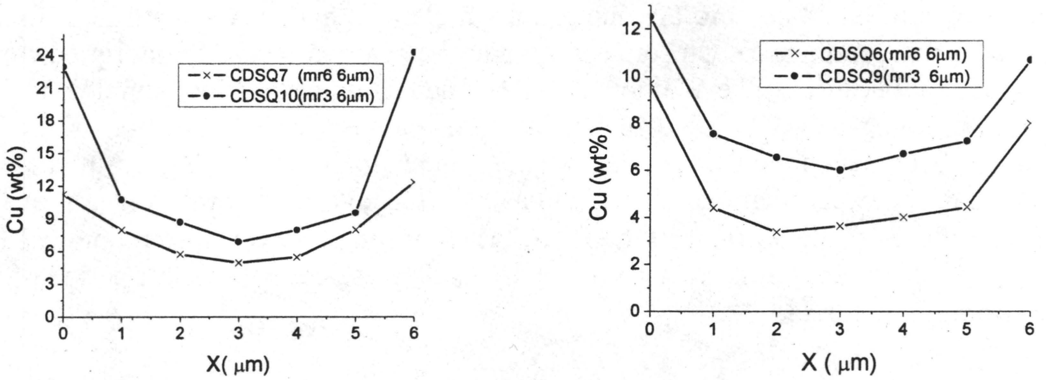

(a) (b)

Figure 6-23: Typical profile of Cu concentration with a cell for the two mass ratios, mr6 and mr6 showing that the gradient of Cu concentration is higher in the higher mass ration for the same size of the cells in each mass ratio. (a) quenched after 2 s and (b) quenched after 3.3 s

Numerical simulations were carried out to better understand the re-distribution of the thermal and solute fields inside the cells forming the Area2 in the samples obtained from the interrupted rapid quenching experiments. Further, these simulations enabled a better understanding of the nucleation event inside these cells that would lead to the solidification of the same.

Since, incorporating the natural convection phenomenon in the numerical simulations would be a tedious and time consuming process, it was perceived to be beyond the scope of this project and hence only the thermal and solute mass diffusion processes were modeled inside the cells. The results may not accurately reflect the phenomena of re-distribution of the thermal and solute fields inside the cells, but would present a better understanding of the interplay between these fields in the cell to effect a nucleation process and enable the prediction of the same to propose a strong hypothesis of the solidification phenomenon inside the cells forming the Area2.

Figure 6-24 shows a comparison of the Cu concentration inside the cells forming Area2 in the microstructure of samples from the rapid interrupted quenching experiments in Table 5-2 with those obtained in the numerical simulations experiments shown in Table 5-4. Figure 6-24 (a) and (b) were from the NS1 with CDSQ6 and NS2 with CDSQ7 experiments, respectively, with a mass ratio of mr6 and a quenching time (t_{quench}) of 2 and 3.3 s, respectively. Figure 6-24 (c) and (d) were from the NS3 with CDSQ9 and NS4 with CDSQ10 experiments, respectively, with a mass ratio of mr3 and a quenching time (t_{quench}) of 2.3 and 3.3 s, respectively. The images from an SEM of the actual cells obtained from the respective experiments used for the validation are shown in Figure 6-24. The profile obtained in the numerical simulations match well with that from the experiment data, further, the Cu concentration at the centre of cells is under predicted by the simulation because of the additional effect of advection caused by natural convection the cells enabling a higher build of Cu in these regions. Since diffusion is the only transport phenomenon in the simulation, the solute gradients are higher in the same compared to the experiment results which have a high advection. Since the size of these cells are between 6 and 9 μm, the kinetics of the diffusion process is also pronounced and results in a significant re-distribution of solute inside these cells in a short period of time as shown in Figure 6-24.

Figure 6-24 shows that the numerical model is valid and that our understanding of the formation of the cells in Area2 of the microstructure (Figure 6-19) and the subsequent re-distribution of the thermal and solute fields inside these individual cells are valid. Further simulations of the numerical model were carried out for a specific cell size (section 5.3.2) for two mass rations of mr6 and mr3 and three initial temperatures of Alloy1 (T_l) for each of the mass ratios to better understand the interplay between the transient re-distribution of the thermal and solute fields inside the cells.

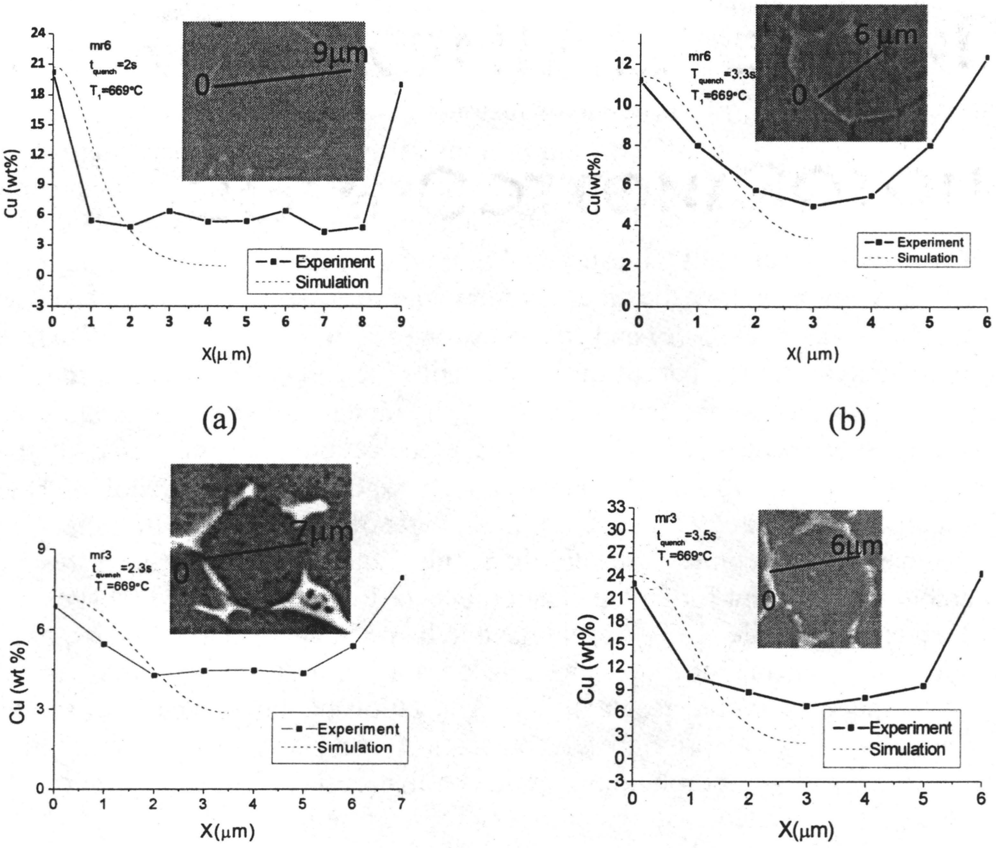

(a) (b)

(c) (d)

Figure 6-24: `Comparison of the profiles of Cu (solute) concentration inside the cells forming Area2 obtained from the numerical simulations experiments shown in Table 5-4 of Section 5.3.2 and line scan data on samples from the interrupted quenching experiments shown in Table 5-2 of Section 5.2.1. The boundary and initial conditions from specific cells obtained from experiments were used for the numerical simulations to enable validation of the same. The SEM image of the specific cells used for each experiment is shown along with the respective Cu concentration profiles. (a) NS1 and CDSQ6 (mr6 and t_{quench} = 2s), (b) NS2 and CDSQ7 (mr6 and t_{quench} = 3.3s), (c) NS 3 and CDSQ9 (mr3 and t_{quench} = 2.3s), (b) NS 4 and CDSQ10 (mr6 and t_{quench} = 3.5s).

Figure 6-25 shows the result of the numerical simulations showing the thermal and solute re-distribution inside a typical cell of about 12 μm size from the Area2 of a CDS process with mr6. Figure 6-25 (a) to (l) shows the results of various conditions such as two levels of mass ratio and three levels of T_1 for two time periods of simulations wherein the two time periods of simulation were identical for all the respective experiment condition. The shaded regions in Figure 6-25 (a) to (l) represent the region of undercooling of the liquid temperature below the respective liquidus temperature. The set-up, description and procedure of the simulation process were presented in Section 5.3.2.1. For experiments with mr6 in Figure 6-25 (a) to (f), the diffusion of mass and temperature is such that for the lower value of T_1 = 665 °C, certain regions in the cell would perpetually present a distinct undercooling in the liquid below the instantaneous transient liquidus temperature as shown in Figure 6-25 (a) and (b), which would lead to a highly favourable situation for a nucleation event in the cell. Further in Figure 6-25 (a) and (b), the amount of liquid with an undercooling below the liquidus temperature increases with time spent in the Segment BCD. Figure 6-25 (c) and (d) shows the profiles for T_1 = 670 °C wherein the extent of undercooling for a part of the liquid inside the cell is less than that in the case of T_1=665 °C and further, as the time progresses, the undercooling in temperature decrease presenting a less favourable environment for the nucleation of a solid phase. Figure 6-25 (e) and (f) shows the profiles for T_1 = 680 °C wherein the undercooling below the liquidus temperature decreases with time in all parts of the cell and with longer time, the actual temperature becomes greater than the liquidus temperature presented an unfavourable environment for any nucleation event. Figure 6-25 (a) to (f) shows that for mr6, the superheat of Alloy1 (T_1) would have to be maintained at a low value to enable a favourable environment for nucleation inside the cells forming Area2 and higher superheat temperature would result in homogenization of the thermal and solute fields inside the cells in Area2 prior to any nucleation event and result in a solidification (dendritic primary phase morphology) similar to that observed in a conventional casting process with a homogeneous alloy composition , thus defeating the purpose of the CDS process. Figure 6-25 (g) and (h) shows the profiles within the cells for experiments with mr3 and T_1 = 665 °C; wherein a significant undercooling below the respective liquidus temperature maintained for a significant portion of liquid inside the cell at both the times of simulation suggesting that a highly favourable for nucleation exists with the cells in Area2 for the nucleation event of a solid phase. In Figure 6-25 (i) and (j), for mr3 and T_1 = 670 °C, the extent of undercooling below the respective liquidus temperature is less than that observed for T_1 = 665 in Figure 6-25 (g) and (h), but a reasonable favourable environment for the nucleation event still exists within the cells. Further in Figure 6-25 (k) and (l), with mr3 and T_1 = 680 °C, the extent of undercooling further reduces to almost being non-existent resulting in a non-possibility of a nucleation event of a solid phase. Comparing the extent of undercooling below the liquidus temperature for the two cases of mr6 (Figure 6-25 (a) to (f)) and mr3 (Figure 6-25 (g) to (l)), once could observe that the mr3 conditions present a more favourable environment of nucleation event of a solid phase than the mr6 condition and further, a larger range of initial temperature of Alloy1 (T_1) would be permissible with the lower mass ratio to enable a viable CDS process and this would prove useful in a commercial casting environment. However, the volume of liquid with the favourable undercooling for nucleation would have a higher concentration of Cu in the case of mr3 than in mr6 experiments as observed in Figure 6-25 and it shall be further explained in the next section on the growth of these nuclei, that the lower mass ratio presents a less favourable environment for the continued stable growth of the solid/liquid interface which is required to attain a more non-dendritic morphology of the primary Al phase in the final solidified structure.

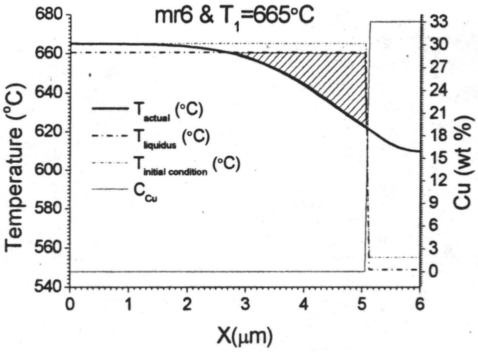
mr6 & T$_1$=665°C
Temperature (°C)
Cu (wt %)
X(μm)
T$_{actual}$ (°C)
T$_{liquidus}$ (°C)
T$_{initial\ condition}$ (°C)
C$_{Cu}$
540
560
580
600
620
640
660
680
0
3
6
9
12
15
18
21
24
27
30
33
0
1
2
3
4
5
6

(a)

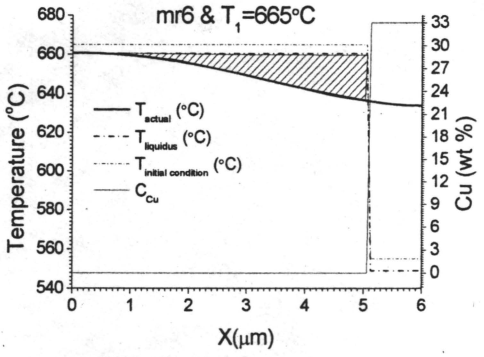
mr6 & T$_1$=665°C
Temperature (°C)
Cu (wt %)
X(μm)
T$_{actual}$ (°C)
T$_{liquidus}$ (°C)
T$_{initial\ condition}$ (°C)
C$_{Cu}$
540
560
580
600
620
640
660
680
0
3
6
9
12
15
18
21
24
27
30
33
0
1
2
3
4
5
6

(b)

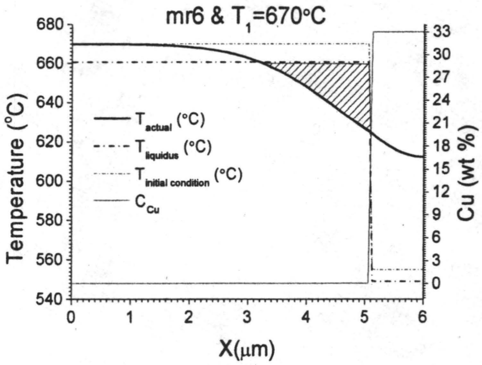
mr6 & T$_1$=670°C
Temperature (°C)
Cu (wt %)
X(μm)
T$_{actual}$ (°C)
T$_{liquidus}$ (°C)
T$_{initial\ condition}$ (°C)
C$_{Cu}$
540
560
580
600
620
640
660
680
0
3
6
9
12
15
18
21
24
27
30
33
0
1
2
3
4
5
6

(c)

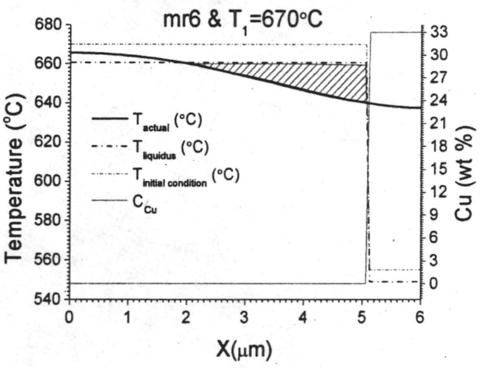
mr6 & T$_1$=670°C
Temperature (°C)
Cu (wt %)
X(μm)
T$_{actual}$ (°C)
T$_{liquidus}$ (°C)
T$_{initial\ condition}$ (°C)
C$_{Cu}$
540
560
580
600
620
640
660
680
0
3
6
9
12
15
18
21
24
27
30
33
0
1
2
3
4
5
6

(d)

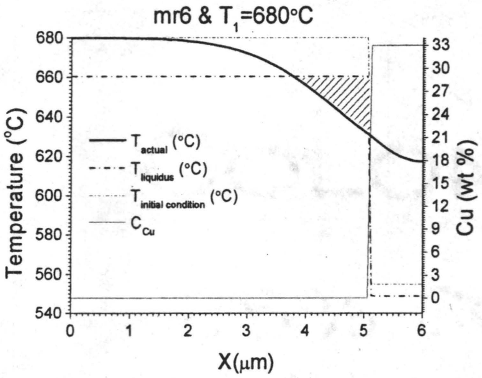
mr6 & T$_1$=680°C
Temperature (°C)
Cu (wt %)
X(μm)
T$_{actual}$ (°C)
T$_{liquidus}$ (°C)
T$_{initial\ condition}$ (°C)
C$_{Cu}$
540
560
580
600
620
640
660
680
0
3
6
9
12
15
18
21
24
27
30
33
0
1
2
3
4
5
6

(e)

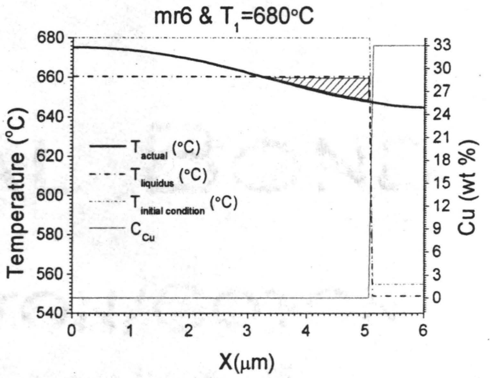
mr6 & T$_1$=680°C
Temperature (°C)
Cu (wt %)
X(μm)
T$_{actual}$ (°C)
T$_{liquidus}$ (°C)
T$_{initial\ condition}$ (°C)
C$_{Cu}$
540
560
580
600
620
640
660
680
0
3
6
9
12
15
18
21
24
27
30
33
0
1
2
3
4
5
6

(f)

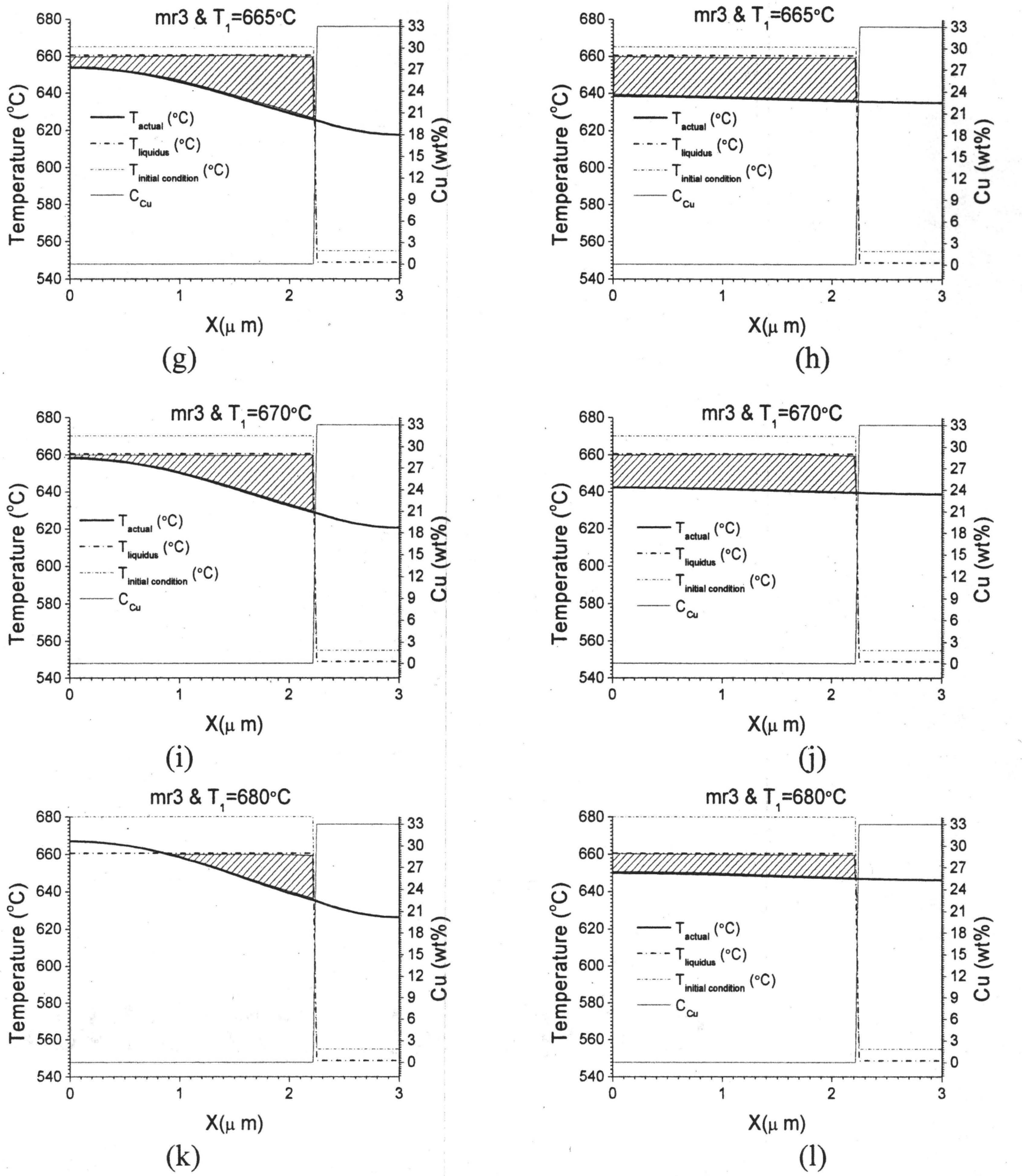

mr3 & T_1=665°C

mr3 & T_1=665°C

mr3 & T_1=670°C

mr3 & T_1=670°C

mr3 & T_1=680°C

mr3 & T_1=680°C

(g) (h) (i) (j) (k) (l)

Figure 6-25: Results of the numerical simulation experiments presented in Table 5-4 of Section 5.3.2.2 showing the transient profiles for the actual liquid temperature (T_{actual}) , liquidus temperature ($T_{liquidus}$) and concentration of Cu (C_{Cu}) for two values of initial mass ratios of mr6 and mr3,three value of T_1 for each mass ratio, and two simulation time steps for each value of T_1. (a) and (b) NS5 at two progressive time steps, (c) and (d) NS6 at two progressive time steps, (e) and (f) NS7 at two progressive time steps, (g) and (h) NS8 at two progressive time steps, (i) and (j) NS9 at two progressive time steps, (k) and (l) NS10 at two progressive time steps.

6.2.2.3Final Nucleation Event (Point D)

During the thermal and solute re-distribution in the segment BCD (Figure 6-4) two areas form in the liquid mixture of the resultant mixture, namely Area2 and Area3, as shown in Figure 6-19; wherein Area2 is the formation of cells caused by the significant difference in the surface tension and density of the two precursor alloys and Area3 is described by pockets of liquid wherein the diffusion and advection has caused a near-homogenized thermal and solute fields resulting in an alloy liquid with a nearly constant composition and temperature. The composition, amount and distribution of the liquid pockets forming Area3 would strongly depend on the amount of nucleation during mixing forming Area1; and the number and distribution of the cells forming Area2 in the microstructure. The Area3 observed in the microstructure of samples obtained from the rapid quenching experiments with the ribbon casting equipment were compared with that of the samples obtained in the same experiments with an initial alloy of homogeneous composition and temperature akin to Alloy3 as described by the experiments in Table 5-2 of section 5.2.1. Figure 6-26 shows such as comparison with typical microstructure of from an optical microscope of Area3 in samples from CDSQ1 experiments compared with that from CONVQ1 and CDSQ3 experiments compared with that from CONVQ2, respectively; showing that the microstructure of Area3 in the CDS process is mostly identical to the bulk microstructure obtained from the respective conventional alloy samples suggesting that the composition of the liquid pockets forming Area3 was nearly homogeneous prior to the quenching phenomenon.

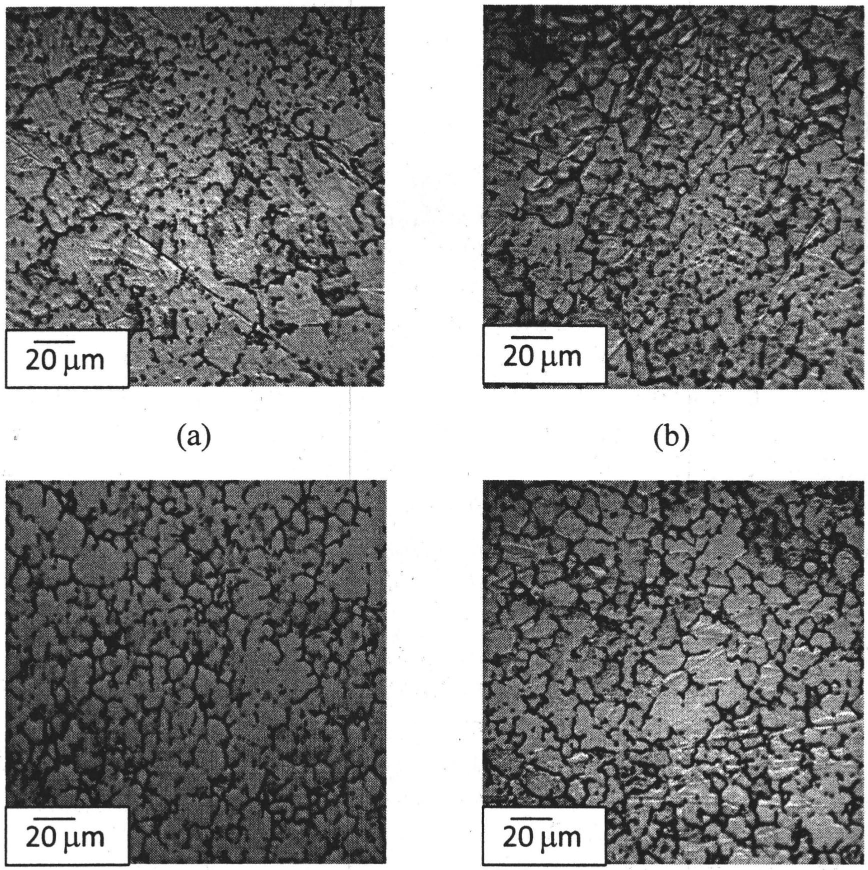

(a) (b)

(c) (d)

Figure 6-26: Typical microstructure of samples from the rapid interrupted quenching experiments as obtained from an optical microscope comparing the morphology of the grains between the CDS and conventional processes for certain experiments shown in Table 5-2. (a) CDSQ1 (mr6 and T_1=665 °C), (b) CONVQ1 (Al-4.7 wt%Cu), (c) CDSQ3 (mr3 and T_1=665 °C) and (d) CONVQ2 (Al-8 wt%Cu).

The results and discussion presented in this section on the re-distribution of the thermal and solute fields and nucleation events in Segment BCD of Figure 6-4 of the CDS process could be summarized as follows:

- The thermal fields re-distribute and nearly equalize in the macro-scale bulk liquid prior at the early stages of the segment BCD as denoted by point C.
- Three distinct and unique areas form in the liquid mixture during this Segment BCD, namely, Area1 described by the growing primary Al solid phase nucleated from Alloy1 during the mixing stage as denoted by Segment AB, Area2 described by the polygonal cells akin to Bernard cells formed due to the significant difference in the surface tension, density and temperature of the two precursor

liquids co-existing in the mixture in the micro-scale, and Area3 described by the pockets of liquids in which the thermal and solute fields have nearly homogenized due to advection and diffusion processes.

- The nucleation of solid in Area1 takes place during the mixing stage denoted by Segment AB, the nucleation of solid in Area2 takes place during the re-distribution of thermal and solute fields inside the polygonal cells forming this area at some time in Segment BCD and the final nucleation of solid takes place from the liquid forming Area3 at Point D.

6.2.3 Growth of Stable Nuclei

There are three distinctly different nucleation events during the CDS process, one in each of the three areas in the resultant mixture as shown in Figure 6-19: Area1, Area2 and Area3. The transient thermal and solute environment during the growth of the solid/liquid interface is unique and different for the nuclei in three area of the mixture.

In this section, results and discussion on the growth of a stable nuclei in the three areas of the mixture would be presented as the following sub-sections:

- Growth in Area1
- Growth in Area2
- Growth in Area3

6.2.3.1 Growth in Area1

The nucleation in Area1 is that of the primary Al phase from the Alloy1 during the mixing stage. Pockets of liquids are dissipated in the resultant mixture during mixing into a liquid which is at a significant undercooling below the liquidus temperature of Alloy1 as shown by Figure 6-11 during Segment AB. The undercooling effects a nucleation event in these pockets of Alloy1 liquid which would subsequently begin to grow. The environment faced by these nuclei is unique and shown by the schematic of the transient temperature and Cu concentration profiles ahead of the growing solid/liquid (S/L) interface of a typical nuclei in Area1 in Figure 6-27 for progressive time steps during growth, respectively. In Figure 6-27, the progressive time steps are shown by the numbers 1, 2 and 3 for the respective profiles of liquidus temperature (T_L), actual temperature (T_{actual}) and Cu concentration (C_{Cu}); and the extent of undercooling of the actual temperature below the respective liquidus temperature at any location ends at the point denoted by ξ in the domain ahead of the growing S/L interface. In Figure 6-27, at any time step, the Cu concentration in the liquid increases ahead of the boundary of the liquid Al droplet, of pure Al concentration, into the liquid due to the high Cu concentration of the resultant alloy mixture. This Cu profile would define the profile of T_L and these two profiles would change with time due to the transfer of the Cu solute towards the growing nuclei caused by diffusion and advection; resulting in a gradual decrease of the pure Al boundary in the liquid pocket. The profile of T_{actual} would also changes with increasing time steps due to the heat extraction from the growing nuclei caused by the low temperature of the mixture. The intersection point of the T_L and T_{actual} ahead of the S/L interface denoted by ξ in Figure 6-27 denotes the extent of undercooling of liquid below the liquidus temperature. The interplay between the solute transport towards and heat flux away from the S/L interface would result in relative movement of the point ξ towards the S/L interface causing a decreasing undercooled environment of the liquid ahead of the interface and resulting in an increasingly stable growth of the S/L interface. The nuclei would initially face a liquid at a lower temperature than the liquidus temperature which would initially be the melting point of pure Al (T_m). The gradient of the actual liquid temperature ahead of the S/L interface would continue to decrease but the liquidus temperature would still be at T_m due to the slower mass transport than temperature transport. There would be an initial perturbation of the S/L interface during growth showing tendencies of instability in the growth. However, the decreasing temperature gradient in the liquid ahead of the S/L interface will decrease the extent of instability of this interface because the extent of undercooling decreases as shown by the point ξ in the time steps 1 and 2 in Figure 6-27. Hence, the growth of primary Al phase forming Area1 would be nearly stable with a marginally perturbed interface and the perturbation increases with increasing rates of heat extraction from the S/L interface (increasing cooling rate of the casting). At increasing time steps, in Figure 6-27, the point ξ would relatively move closer to the S/L interface and when these two intersect, the growth with cease and form the morphology of the primary Al phase forming Area1 in the solidified microstructure. In Figure 6-27, the point of intersection between the S/L interface and point ξ is denoted by the profiles for time step f; assuming the worst case scenarios that the actual temperature of the liquid would equalize prior to the cessation of the growth. Further, around the time when the growth of primary Al phase forming Area1 would cease, the Area2 and/or Area3 would form around the growing S/L interface and further eliminate the undercooling sooner than time step f in the liquid (the point ξ reaches the S/L interface location). Figure 6-28 (a) to (c) shows typical secondary electron image microstructures from an SEM and the respective line scan profiles of the Cu concentration across the primary Al grain forming Area1 in samples obtained from the interrupted quenching experiments: CDSQ1, CDSQ2 and CDSQ3, respectively, as shown in Table 5-2. The profiles show that the Cu concentration is nearly zero in the middle of the grain due to the nucleation from the pure Al in Alloy1 and growth in the droplets of pure Al, and towards the outer regions of the grain, the Cu concentration gradually increases until the end of solidification of the grain effected by the loss of undercooling in the liquid ahead of the growing S/L interface as explained in the previous paragraph with Figure 6-27. The Cu profile shown in the schematic of Figure 6-27 for the time step f from the S/L interface to the boundary defined by the point ξ for this time step would match the one in the line scan profile obtained from Area1 in Figure 6-28 (a) to (c).

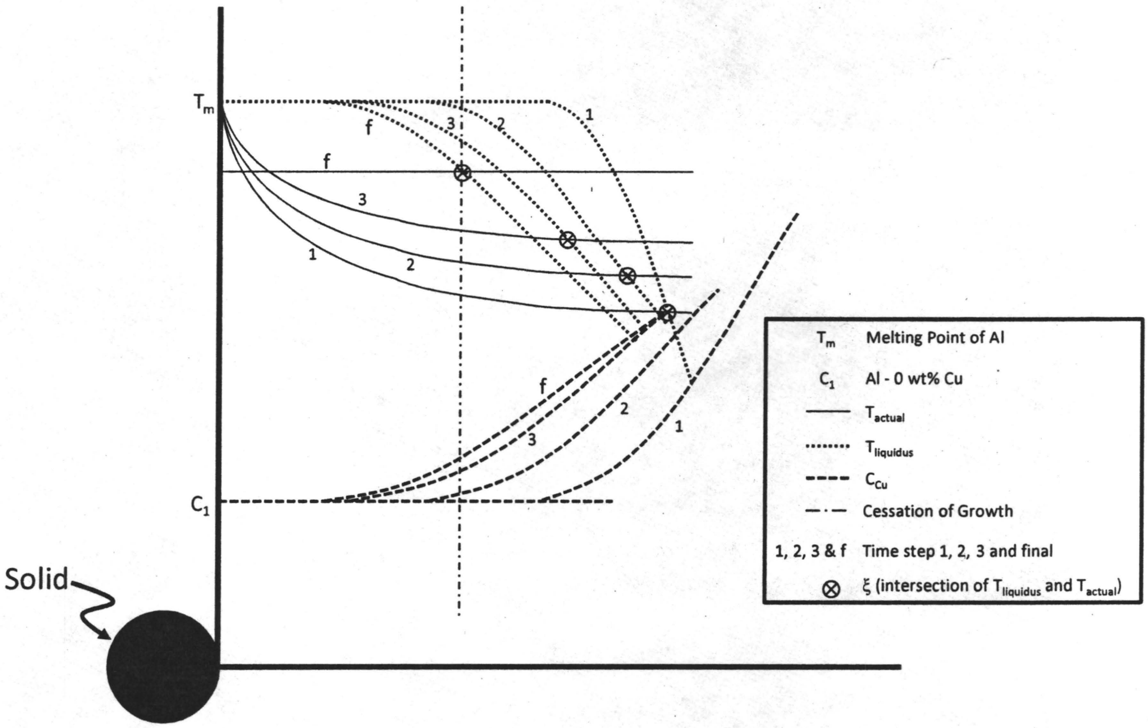

Figure 6-27: Schematic of the transient temperature and Cu concentration profiles ahead of the growing nuclei in Area1. Notations 1, 2, 3 and f show progressive snapshot profiles with increasing time steps for the actual liquid temperature, liquidus temperature and concentration of solute (Cu), respectively. The point ξ marks the instantaneous location in the liquid ahead of the solid/liquid interface until which an undercooling exists in the actual temperature below the respective liquidus temperature.

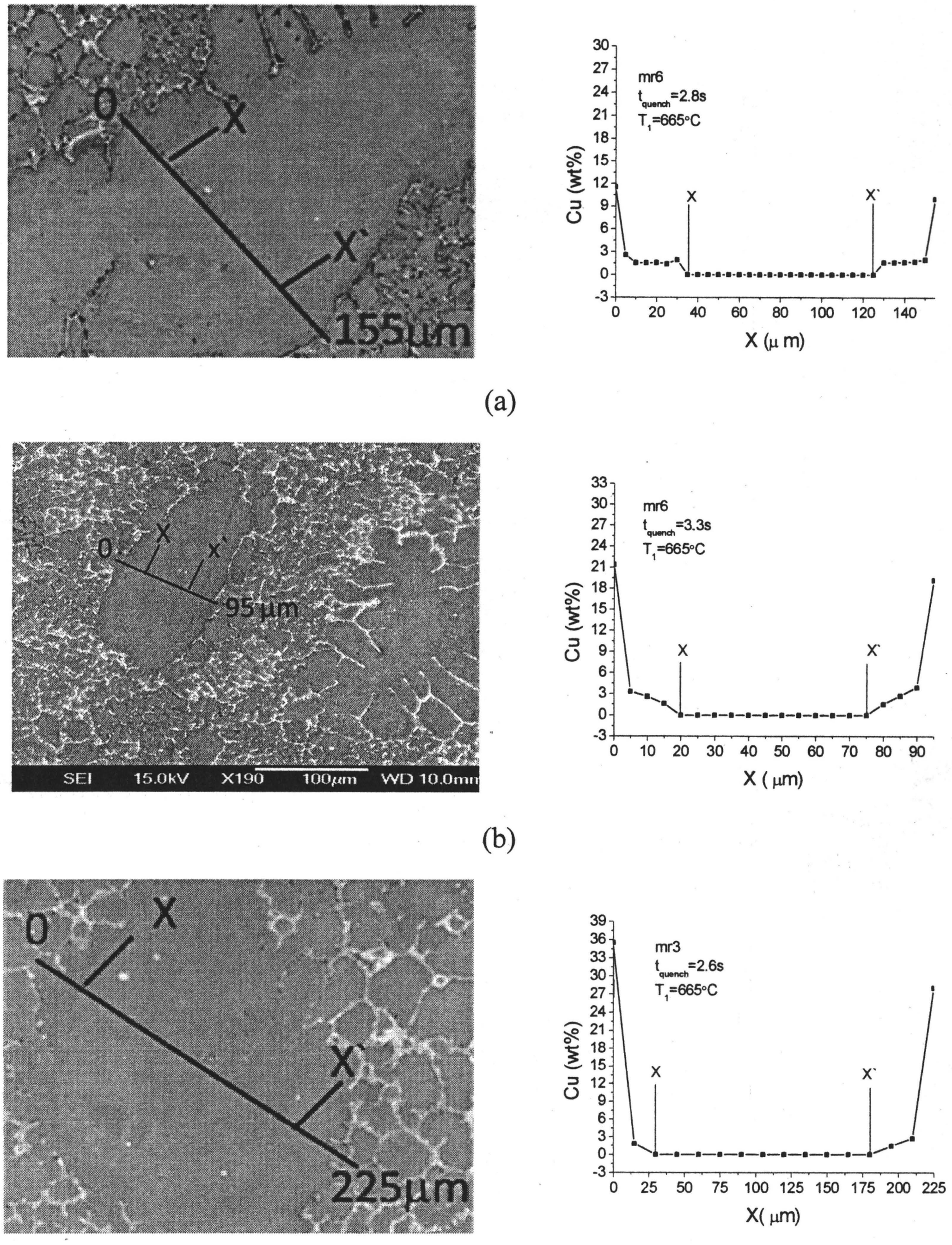

Figure 6-28: Typical secondary electron image microstructures from an SEM and profiles of Cu concentration inside the grain of primary Al phase forming Area1 as obtained from samples form the interrupted rapid quenching experiments. (a) CDSQ1 (mr6, T_1=665 °C and t_{quench} = 2.8 s), (b) CDSQ2 (mr6, T_1=665 °C and t_{quench} = 3.3 s), and (c) CDSQ3 (mr3, T_1=665 °C and t_{quench} = 2.5 s).

The growth of the nuclei forming Arae1 in the microstructure is unique in that the S/L interface grows in the direction of the heat flux; and further the solute transport is towards the S/L interface and the heat flux is away from the same into the liquid ahead of the interface. Such thermal and solute re-distribution directions are exactly opposite to those observed in conventional solidification processes.

6.2.3.2Growth in Area2

Figure 6-25 shows the snapshots of the thermal and solute field re-distribution profiles in a typical cell forming Area2 of the microstructure in two time steps of numerical simulation. As discussed in the previous section, the environment for a nucleation event (undercooling of liquid) inside these cells would be more favourable with decreasing superheat temperatures of Alloy1 (T_1), and in this section, the results and discussion on the growth of a stable nuclei inside these cells shall be presented.

As an example, in Figure 6-25 (a), the nucleation event could occur inside the cell forming Area2 at any location past the point of intersection of the liquidus and actual liquid temperatures (around the 3 μm mark). Assuming the nucleation occurs at an arbitrary location in this undercooled region, Figure 6-29 presents a schematic of the transient profiles for the actual liquid temperature (T_{actual}), liquidus temperature ($T_{liquidus}$) and concentration of solute (C_{Cu}) in the half of the cell forming Area2. Symmetry in thermal and solute fields would dictate that the other half of the cell has identical profiles as well. In Figure 6-29, the profiles denoted by N represent a hypothetical condition for the thermal and solute field at the instant of the nucleation event. The S/L interface of the growing nuclei would reject solute and limited diffusion of this solute into the liquid has been assumed. The profiles denoted by the numbers 1 and 2 represent two snap shots of the three profiles at two increasing time steps of the growth process.

In the regime marked “LEFT” in Figure 6-29, the change in the profile of C_{Cu} would be marginal because the nucleation event would restrict the diffusion of the solute Cu to this regime; and reflecting in a marginal change in the gradient of $T_{liquidus}$ as shown by the profiles 1 and 2 for these parameters, respectively. However, the value of T_{actual} would continue to drop significantly due to the heat extracted from the middle of the cell to the outside. Typically, the S/L interface facing “LEFT” would grow at a very slow rate until the gradient of T_{actual} becomes significantly less than the gradient of $T_{liquidus}$ at the interface location and beyond this time, the S/L interface may begin to show perturbations leading to an unstable growth. However, a typical cell in Area2 would be about 10 to 20 μm, in diameter and hence, these perturbation that would eventually arise in the regime marked “LEFT” would not lead to a breakdown of the S/L interface into a dendritic morphology but rather solidify with a near stable interface morphology.

In the regime marked “RIGHT” in Figure 6-29, the changes in the Cu profile from the S/L interface into the liquid is shown by the progressive time steps denoted by number 1 and 2; wherein the rejection of the solute Cu at the S/L interface would result in an initial decrease of C_{Cu} and then would increase due to the diffusion of Cu from the boundary of the cells in towards the S/L interface. This effect is shown clearly by the profiles marked as 2 in Figure 6-29 for the "RIGHT" regime. With progressive time steps during growth, the undercooling in the liquid ahead of the S/L interface marked by the region bounded by the profile of $T_{liquidus}$ and that of T_{actual} decreases as could be observed by the larger region for time step 1 than for 2. Further the growth region would be in the order of a few microns (~60 μm) and this coupled with a decreasing level of undercooling in the liquid would result in a stable growth of the S/L interface in the "Right" regime.

The direction of bulk solute and temperature transport in the regime marked "RIGHT" in Figure 6-29 would be towards and away from the S/L interface; and exactly opposite to those observed in a conventional solidification process.

In sum, the morphology of the growing interface from the nucleation events in the cells forming Area2 would be nearly stable and the stability would increase with increasing initial size of the cells for a given initial mass ratio of the precursor alloy. Further, the earlier the incidence of a nucleation event in the cells, the more non-dendritic would be the morphology of the primary Al phase from these cells. A lower value of the initial temperature of Alloy1 (T_1) would result in a more favourable environment for an early nucleation event inside the cells in Area2 as shown by the numerical simulation results in Figure 6-25.

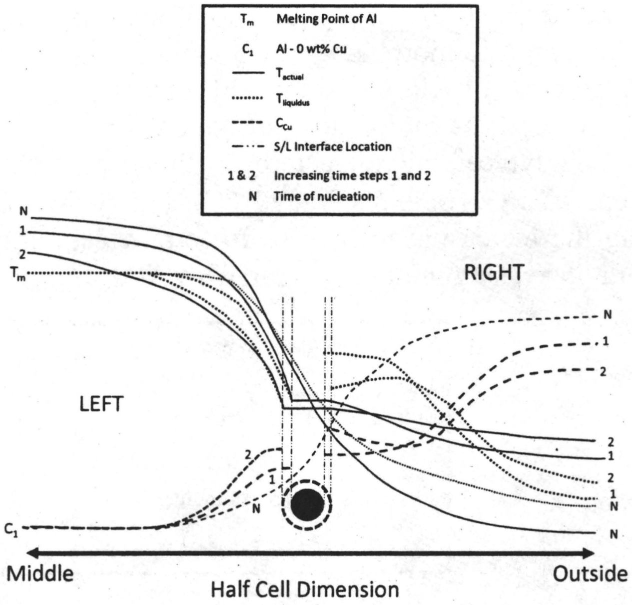

Figure 6-29: Schematic of the transient temperature and Cu concentration profiles ahead of the growing nuclei inside a typical cell forming Area2. Notations 1 and 2 show progressive snapshot profiles with increasing time steps for the actual liquid temperature, liquidus temperature and concentration of solute (Cu), respectively. The profiles denoted by the letter N stands for the condition at with the hypothetical nucleation event occurred in an arbitrary location of the undercooled section of the liquid.

6.2.3.3Growth in Area3

As discussed in Section 6.2.2.3, the Area3 would have nearly homogeneous temperature and concentration of Cu. A nucleation event in this area as denoted by Point D in Figure 6-4, would result in the growth akin to the theoretical analysis on an equiaxed growth in an isothermal liquid [119]. Figure 6-30 shows a schematic diagram representing the transient profiles of the actual liquid temperature (T_{actual}), liquidus temperature (T_L) and concentration of solute (C_{Cu}) for two progressively increasing time steps of 1 and 2 during the growth of a nuclei in the liquid forming Area3. The release of the latent heat of fusion at the S/L interface would result in a negative temperature gradient in the liquid and the growth would reject Cu at the interface causing a negative gradient of C_{Cu}, as well. The undercooling in the liquid bounded by the instantaneous $T_{liquidus}$ and T_{actual} would result in an unstable growth of the S/L interface leading to its breakdown into a dendritic morphology. However, the size of Area3 is in the order of a few microns (~50 μm) and hence, the solute (Cu) build up caused by the limited diffusion of Cu into the liquid and away from the S/L interface would slow down the growth and the extent of instability and break down of the interface. The resultant microstructure of the primary Al phase in Area3 would be either rosette shaped in small sizes of Area3 and dendritic in larger sizes of the area. Further, increasing number of nucleation events in Area3 would decrease the extent of dendritic morphology of the primary Al in these areas. Further, increasing initial temperature of Alloy1 (T_1) would result in increasing instability of the growing interface and a dendritic morphology of the primary Al phase in Area3. Figure 6-31 (a) and (b) shows typical microstructures with Area3 from the samples in the laboratory experiments CDS3 (mr6 & T_1=670 °C) and (CDS5 (mr6 & T_1=683 °C), respectively showing the increasing tendencies to form a dendritic morphology by the primary Al phase with increasing initial temperature of Alloy1 (T_1).

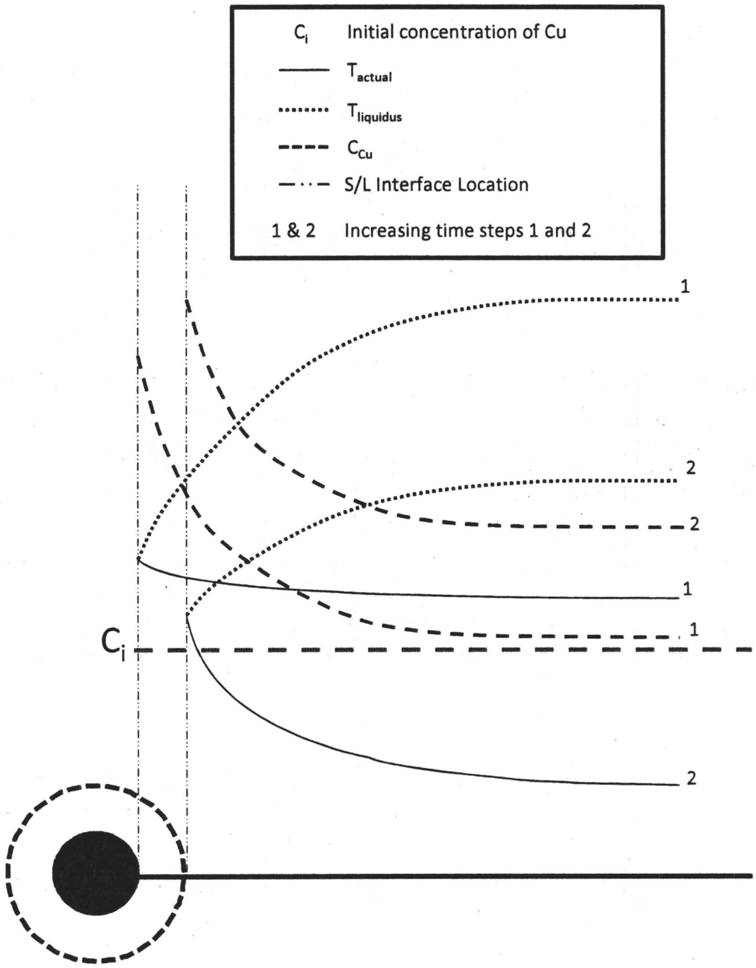

Figure 6-30: Schematic of the transient temperature and Cu concentration profiles ahead of the growing nuclei in the liquid forming Area3. Notations 1 and 2 show progressive snapshot profiles with increasing time steps for the actual liquid temperature, liquidus temperature and concentration of solute (Cu), respectively.

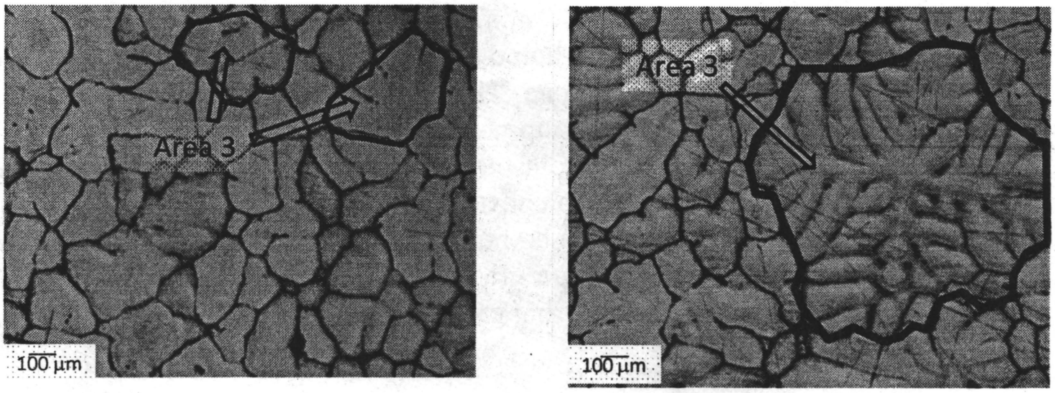

Figure 6-31: Typical microstructures from an optical microscope of (a) CDS3 (mr6 & T_1=670 °C) and (b) CDS4 (mr6 & T_1=683 °C); showing the increase in instability of the grain in Area3 forming a more dendritic morphology with increasing initial temperatures of Alloy1 (T_1).

6.2.3.4Growth Stability in CDS

In a good CDS process, the bulk of the liquid in the segment BCD shown in Figure 6-4 would have cells forming Area2 as shown in Figure 6-19. The stability of the S/L interface instantaneously after the nucleation event in these cells was discussed in Section 6.2.3.2. A further analysis of the growth of the S/L interface past the point D in Figure 6-4 is critical to fully understand the stability of the interface during the final stages of solidification. Analysis of microstructure of samples obtained from interrupted quenching experiments with a moderate rate of quenching described in Section 5.2.2 to evaluate the re-distribution of the solute ahead of a growing S/L interface during the solidification stage past the point D in Figure 6-4. Figure 6-32 (a) and (b) show a comparison of the Cu concentration at a growing typical S/L interface from grains in Area2 as obtained by line scan analysis in an SEM for the CDS and conventional solidification processes, respectively; showing that the typical Cu concentration in the liquid at the S/L interface of a CDS solidification is significantly lower than that in a conventional process because the nucleation in Area2 takes place at a significant undercooled temperature below the liquidus temperature and the solute Cu diffuses into the growing interface due to the positive concentration gradient of Cu ahead of the interface into the liquid. Hence, the solute build up during growth of the grains from this area would have less Cu rejected at the S/L interface than in the conventional solidification process wherein the Cu rejection would be typically governed by a relationship such as the Scheil-Gulliver expression [54]. To better explain the solidification of grains in the CDS process, Figure 6-33 has been presented; wherein the initial cells in the liquid forming Area2 are represented by the grey polygons with the boundary of high Cu concentration and the enclosure with a low concentration. Nucleation in the cells need not typically take place in all the cells and the black circles in Figure 6-33 show some random nucleation event; and the black lines show the typical S/L interface from these nucleation events in the bulk liquid at a time well after point D in Figure 6-4. The solidified grains forming Area2 would be typically solidify from many initial cells (10 to 20 cells) in the liquid during Segment BCD and the grains would grow simultaneously along with each other. The grains would have low Cu concentration during initial growth and the Cu build up ahead of the S/L interface would be mainly contributed by the transport of mass from the liquid between the grains to the growing interface by advection or diffusion. In a conventional process, the solidifying primary Al dendrites would grow freely into a bulk liquid melt with a negative gradient of Cu concentration and a negative temperature gradient resulting in a predictable build-up of Cu concentration at the S/L interface during growth.

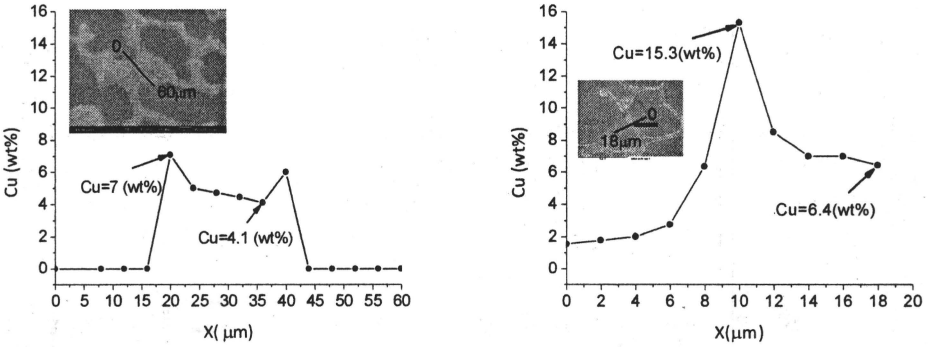

(a) (b)

Figure 6-32 Distribution of Cu concentration around the growing S/L interface in grains from Area2 (Figure 6-19) obtained by line scan data in an SEM for a CDS and conventional solidification processes, examined on samples quenched after point D in Figure 6-4 as explained in Section 5.2.2 (a) CDS process and (b) conventional solidification.

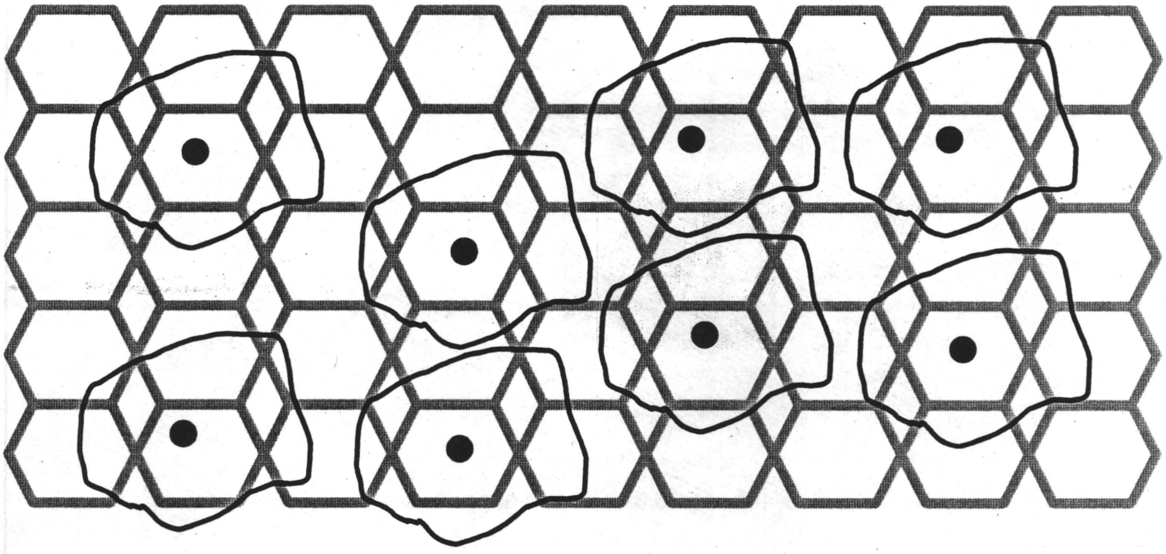

Figure 6-33: Schematic of the growth of grains forming Area2 in a CDS process. The initial cells in the liquid are represented by the thick grey lines where the grey areas are the liquid with high Cu content and white region enclosed are liquid with low Cu content. The black circles represent a few nucleation events in certain cells and the black lines show a typical S/L interface growing in the liquid past point D in Figure 6-4.

Figure 6-34 shows the relationship among fraction solid (F_s), liquid temperature and Cu concentration from the simulation of the conventional solidification process for Al- 4.7 wt%Cu alloy with the non-equilibrium Scheil-Gulliver assumption using a phase diagram simulation tool, Pandat[7]. The image in the inset of Figure 6-34 was obtained from a sample quenching to interrupt the conventional solidification process for an Al-4.7 wt%Cu alloy; from which the fraction solid was quantitatively evaluated as 0.75. Figure 6-34 shows that the Cu concentration in the liquid at the S/L interface during growth for a F_s of 0.75 would be about 15 wt% which validates the value of 15.3 obtained in Figure 6-32 (b) from the a grain in the sample shown in the inset of Figure 6-34.

---

[7] PANDAT^{TM} version 8.1, Computherm LLC, Madison, w1 53719, USA

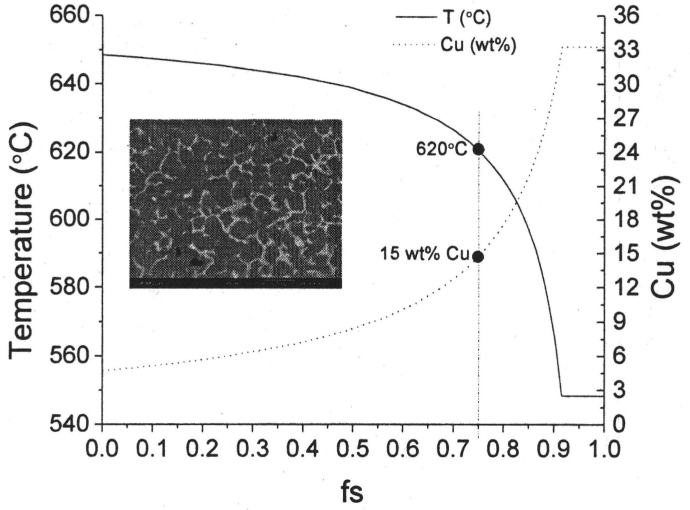

Figure 6-34: Relationship among fraction solid (f_s), temperature of liquid and concentration of Cu during conventional solidification with the non-equilibrium Scheil-Gulliver assumption [54]. The inset is an image of microstructure from an SEM from a sample quenched to interrupt the solidification process in a conventional Al-4.7 wt% Cu alloy to calculate the instantaneous fraction solid.

During the growth of the grains forming Area2 in a CDS process, the Cu concentration gradient would be positive, in the liquid ahead of the S/L interface and with time this gradient will decrease and become negative at which time, the further growth of the grain would be akin to that in a conventional solidification process. The MS criteria described in Section 4.4.1, would apply to evaluate the stability of the S/L interface in a CDS process only after the time when the gradient of Cu concentration ahead of the S/L interface becomes less than or equal to zero. In a conventional solidification process, this gradient is always less than zero.

Figure 6-35 shows the graphical representation of the stability criteria shown in Equation 4-9 of CHAPTER 4 for the MS criteria describing the stability of the S/L interface. The parameters listed in Table 6-3 were used to evaluate the Equation 4-9 and obtain the Figure 6-35. In Figure 6-35, the value of $\left(\frac{G_L}{V}\right)_{critical}$ for the various concentration of Cu in the liquid at the S/L interface (C_L) during the solidification process is shown by the black line. For a given value of C_L, if the solidification conditions places the value of $\left(\frac{G_L}{V}\right)$ above the black line in Figure 6-35, the S/L interface would be more stable and if below the line, the interface would be unstable. The data from Figure 6-32 was used to evaluate the critical values for both the CDS and the conventional solidification process for specific respective values of C_L. The critical value, $\left(\frac{G_L}{V}\right)_{critical}$ for the CDS solidification was less than that for the conventional process, suggesting that the probability of a stable S/L interface is higher for the CDS process. During solidification, the interface is initially stable for both the CDS and conventional processes, however, with time, and thermal and solute re-distribution ahead of the S/L interface the instability sets in earlier in the conventional process when compared to the CDS process suggesting that the probability of obtaining a non-dendritic morphology of the primary Al phase in the CDS process is significantly higher than that in a conventional solidification process.

Table 6-3 Parameters used to determine the stability of the S/L interface using Equation 4-9.

Parameter	Unit	Value	Reference
L_V	J/m^3	4.18 E8	[13]
K_L	W/m k	95	[115]
K_S	W/m k	200	[13]
m_L	^{o}C/wt%Cu	-3.4	[13]
D_L	m^2/s	3E-9	[13]

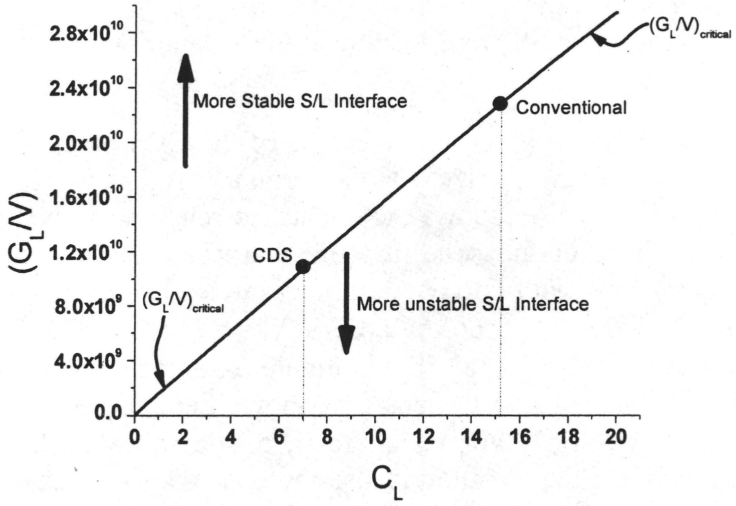

Figure 6-35 Comparison in stability of S/L interface of grown grain between CDS process and Conventional casting

6.3. STUDY OF CRITICAL PROCESS PARAMETERS

The critical parameters that would affect the CDS process, specifically the evolution of a non-dendritic morphology of the primary Al phase were identified as shown below:

- Temperature of Alloy1 (T_1)
- Temperature of Alloy2 (T_2)
- Mass Ratio of Mixing
- Rate of mixing (Alloy1 into Alloy2)

The dependent parameter in the study of the critical parameters was the morphology and grain size of the primary Al phase in the solidified microstructure of a sample in a laboratory CDS experiment described in Section 5.1.2.1.

6.3.1Temperature of Alloy1 (T_1)

The role of T_1 in affect the nucleation and growth of the primary Al phase in all the three unique area in the liquid (Figure 6-19) have been shown by the results and discussion of Section 6.2. The following summarizes the effect of increasing the value of T_1 in the CDS process:

- Decreases the number of nucleation event during the mixing process (Segment AB in Figure 6-4)
- Increases the diffusion coefficient of Cu resulting in:
    - a more unstable growth of the grain in Area1 tending to dendritic morphology
    - a more unstable growth of the grains in Area2 tending to dendritic morphology
    - larger size of Area3 leading to more dendritic morphology in the solidified microstructure

The effect of the changes in T_1 on the events of the CDS process would be reflected in the morphology and grain size of the primary Al phase in the final solidified microstructure. Figure 6-36 shows the quantified relationship between T_1 and the grain size of the Al phase in the solidified microstructure of the samples from the CDS laboratory experiments with mr6 and a mixing rate of 167 gs^{-1} as described in Table 5-1 of Section 5.1.2.1 CDS1 (T_1 = 662 °C), CDS2 (T_1 = 665 °C), CDS3 (T_1 = 670 °C), CDS4 (T_1 = 675 °C) and CDS5 (T_1=683 °C. In Figure 6-36, the 95% confidence interval of the grain size is also shown and the abscissa shows the superheat temperature above the liquidus of Alloy1 (T_1-T_{L1}). For a small range of superheat temperatures of 2 to 7 °C the grain size is small and the variation is also low. As the superheat temperature of Alloy1 increases the grain size increases significantly; and the grain size for the conventional casting laboratory experiment, CONV1 was evaluated to be 1532 μm which is bigger than a superheat temperature of about 20 °C or more. Figure 6-37 shows the typical microstructures of the samples used for the grain size assessment in Figure 6-36. Figure 6-37 shows that apart from the increase in the grain size with increasing values of T_1, the morphology of the primary Al phase also tends to more dendritic as the value of T_1 increases. From Figure 6-36 and Figure 6-37, it could be summarized that (T_1-T_{L1}) $\leq$ 10 °C would be suitable for a successful CDS process with a predominantly non-dendritic morphology of the primary Al phase.

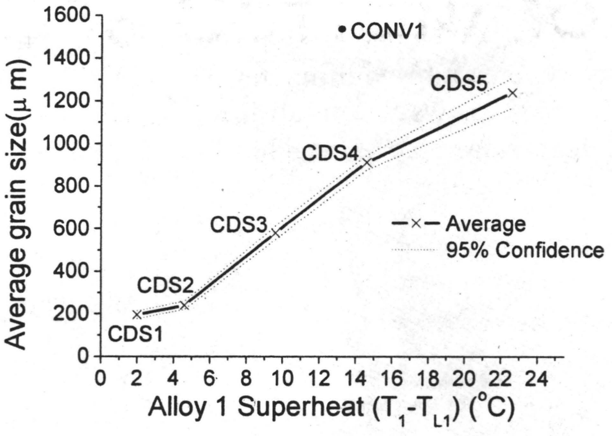

Figure 6-36 Effect of superheat temperature of Alloy1 above the liquidus temperature (T_1-T_{L1}) on the average grain diameter for the laboratory CDS experiments with mr6 and mixing rate of 167 gs^{-1} as described in Table 5-1 CDS1 (T_1 = 662 °C), CDS2 (T_1 = 665 °C), CDS3 (T_1 = 670 °C), CDS4 (T_1 = 675 °C), CDS5 (T_1 = 683 °C) and CONV1 (mr6). Also shown are the 95% confidence boundaries for the data set.

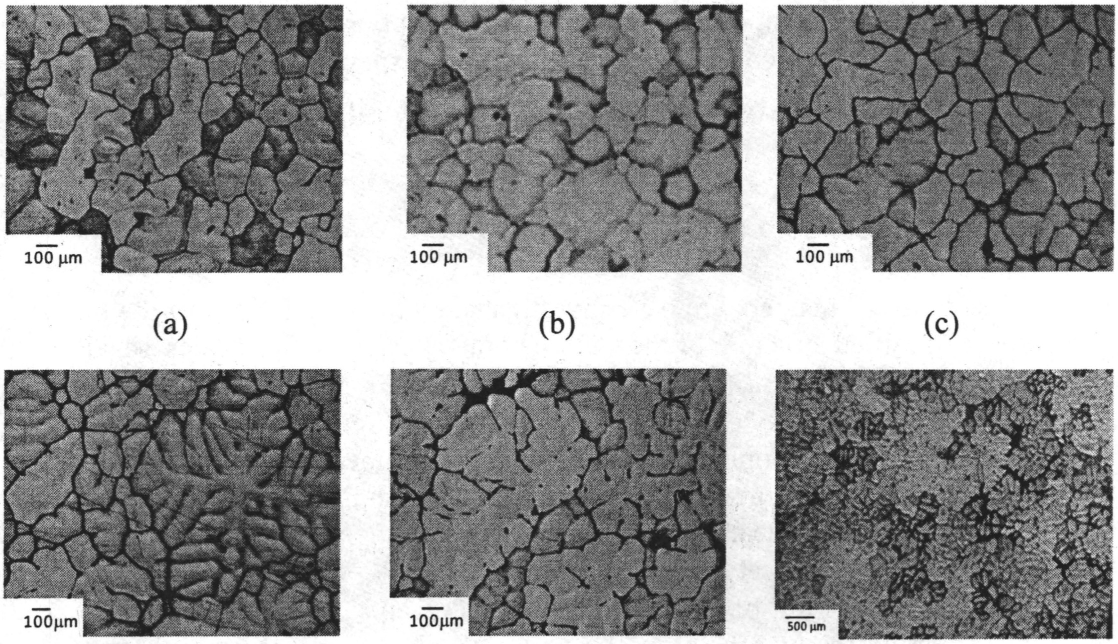

(a) (b) (c)

(d) (e) (f)

Figure 6-37: Typical microstructure from an optical microscope from samples in the laboratory CDS experiments with mr6 and mixing rate of 167 gs^{-1} as described in Table 5-1. (a) CDS1 (T_1 = 662 °C), (b) CDS2 (T_1 = 665 °C), (c) CDS3 (T_1 = 670 °C), (d) CDS4 (T_1 = 675 °C), (e) CDS5 (T_1 = 683 °C and (f) CONV1 (mr6).

Figure 6-38 (a) and (b) shows the relationship between the grain size and (T_1-T_{L1}) for the CDS laboratory experiments mr6 with mixing rate of 113 gs^{-1}, and mr3 with 167 gs^{-1}, respectively. Figure 6-38 shows that in all the CDS laboratory experiments, the grain size increases with increasing value of the Alloy1 temperature (T_1).

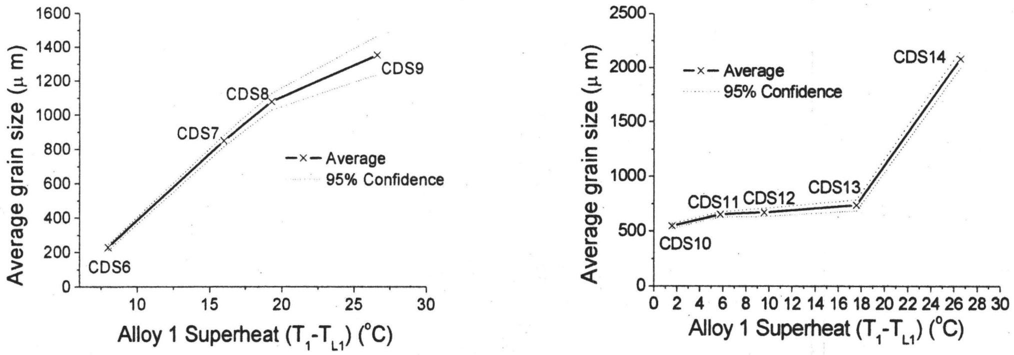

(a) (b)

Figure 6-38: Relationship between grain size and superheat temperature of Alloy1 for the samples from the various CDS laboratory experiments described in Table 5-1 (a) CDS6 to CDS9 (mr6 and 167 gs^{-1}) and (b) CDS10 to CDS14 (mr3 and 167 gs^{-1})

6.3.2Temperature of Alloy2 (T_2)

Two levels of Alloy2 temperature were investigated on the morphology of the primary Al phase in the solidified structure of the CDS laboratory experiments as described in Table 5-1of Section 5.1.2.1: CDS2 (mr6, 167 gs^{-1}, T_1 = 665°C and T_2 = 555 °C) and CDS15 (mr6, 167 gs^{-1}, T_1 = 665°C and T_2 = 578 °C). Figure 6-39 shows the typical microstructures of the samples from these two experiments; wherein no discernable difference in the size or morphology of the primary Al grains was observed and in both the cases the grains were nearly non-dendritic representing a good CDS process. It was concluded that the superheat temperature of Alloy2 (T_2 – T_{L2}) had a lesser effect on changing the morphology of the primary Al phase and even a value of 30 °C had negligible effect on the morphology. This may be because, the thermal mass of Alloy2 was significantly lower than that of Alloy1 and hence the effect of Alloy2 would be marginal on the changes to the events in the CDS process. Specifically, Alloy2 would influence the transient temperature of the mixture during the mixing process which would influence the number of nucleation events in this stage and a increasing the temperature of Alloy2 by nearly 30 °C would still render the transient resultant mixture temperature as significantly lower than the liquidus temperature of Alloy1 (Figure 6-11) to present a favorable undercooled temperature environment for copious nucleation events.

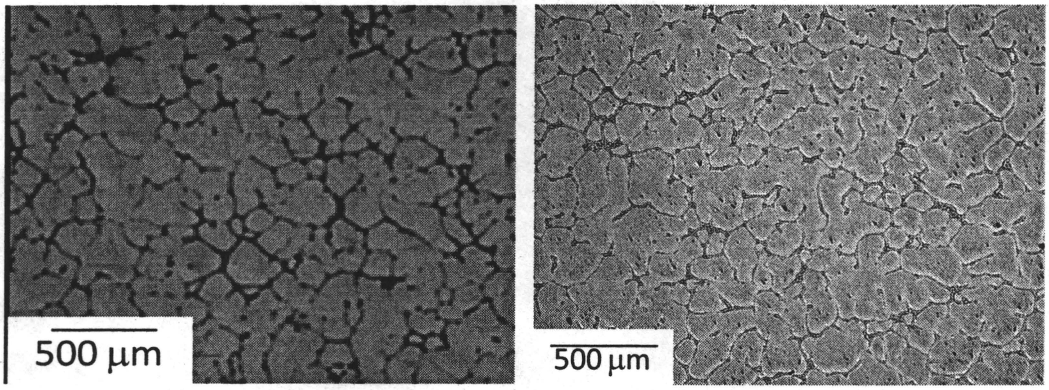

(a) (b)

Figure 6-39 Typical microstructure of Al-Cu system for second alloy superheat changes (a) 10°C and (b) 31°C.

Further, the numerical simulations described in Section 5.3.2 was carried out for three levels of Alloy2 temperature with the mr6, $T_1 = 665$ °C, domain dimensions as constants. These simulations are described in Table 5-4 as NS5 ($T_2 = 555$ °C), NS11 ($T_2 = 565$ °C) and NS12 ($T_2 = 580$ °C). Figure 6-40 (a), (b) and (c) shows the results of these three simulations wherein the T_2 was initialized at the three increasing levels, respectively; wherein the region of undercooling of the melt temperature below the respective liquidus temperature is marked by a shaded region. In the case of T_2 values of 555 °C to 580 °C, the thermal condition in the cells forming Area2, specifically the region of undercooling in the liquid is fairly similar with only marginal variations which could lead one to safely assume that a large range of initial temperature of Alloy2, T_2 could lead to creating a favorable environment for a nucleation event in the cells forming Area2 and promote a non-dendritic morphology of the primary Al phase.

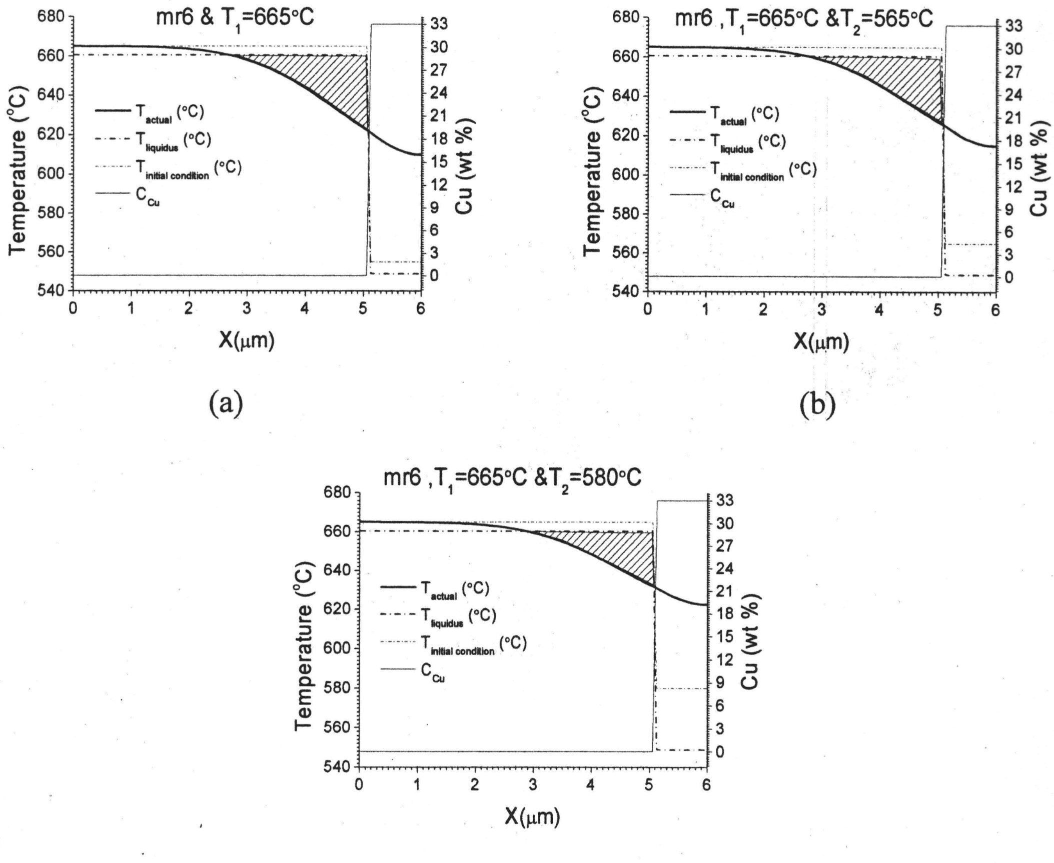

(a) (b)

(c)

Figure 6-40 Numerical date for CDS process of mr6 and Alloy1 665°C carried out at different Alloy2 temperature a) 555°C, b)565°C and c) 580°C.

The results in Figure 6-40 confirm the observations in Figure 6-39 and our proposal that due to the significantly lower thermal mass of Alloy2 than Alloy1, a large variation in T_2 would be permissible to yield a successful CDS process, specifically the preferred nucleation event in Area2 and the subsequent growth of a nearly stable S/L interface to effect a nearly non-dendritic morphology of the primary Al phase in the resultant solidified microstructure.

6.3.3 Mass Ratio of Mixing (mr)

To obtain a resultant Alloy, Alloy3, of a desired composition of the solute elements, a variety of mass ratio of Alloy1 to Alloy2 could be used as precursor alloys for mixing. The value of such a mass ratio has an impact on the morphology of the primary phase in the final solidified alloy. The desired resultant alloy of Al-4.7 wt% C (Alloy3) was chosen to determine the effect of mass ratio, mr. Table 6-4 shows the details of five experiments that were carried out to obtain the Alloy3 with five different values of mass ratio. In Table 6-4, the Alloy1 in all the experiments were pure Al and the composition of Cu in Alloy2 was varied as 10, 15, 20, 25 and 33 wt% to obtain respective mass rations of 1.1, 2.1, 3.2, 4.2 and 6 while mixing the two precursor alloys. The experiment setup shown in Figure 5-4 and described in Section 5.1.2 was used for the experiments in Table 6-4, with a mixing rate of 167 gs^{-1}.

Table 6-4 Experiment conditions to evaluate effect of mass ratio of precursor alloys. Resultant Alloy, Alloy3 was Al – 4.7 wt% Cu alloy.

Designation	Alloy 1				Alloy 2					Mixing Rate (gs^{-1})
		Mass (g)	T_1 (°C)	T_{L1} (°C)		Mass (g)	T_2 (°C)	T_{L2} (°C)	mr	
CDSmr1	Pure Al	182	665	660	Al-10wt% Cu	165	638	633	1.1	167
CDSmr2		234			Al-15wt% Cu	109	618	625	2.1	
CDSmr3		263			Al-20wt% Cu	82	604	600	3.2	
CDSmr4		279			Al-25wt% Cu	65	590	582	4.2	
CDSmr5		292.1			Al-33wt% Cu	47.5	555	547	6	

The decrease in the value of T_{L2} with increasing mass ratio (decreasing solute in Alloy 2) directly affects the amount of the heat transferred from Alloy1 to Alloy2 and the temperature of the resultant mixture which increases the amount of the nucleation taking place during the mixing process. The extent of nucleation from Alloy 1 during the mixing process could be ascertained by the location of point B (refer to Figure 6-4) relative to the liquidus temperature, T_{L1}; the farther point B is below T_{L1}, the higher the amount of nucleation. Figure 6-41 shows the effect of the mass ratio on the location of point B, wherein, the point B lies between T_{L1} and T_{L3}. As the mass ratio increases, the location of Point B is farther down below T_{L1} leading to an increased undercooling of the Alloy 1 during mixing and hence enhance an increased amount of nucleation of teh primary Al phase in the resultant mixture. Figure 6-42(a) to (d) shows the typical microstructure of the samples extracted from the experiments denoted as CDSmr1, CDSmr2, CDSmr3, CDSmr4 and CDSmr5 in Table 6-4 for mr1.1, mr2.1, mr3.2, mr4.2 and mr6, respectively. Figure 6-42(a) shows that the microstructure is pre-dominantly dendritic for the lowest mass ratio, mr 1.1 and gradually changes to a rosette shaped followed by a pre-dominantly globular morphology of the primary Al phase in the microstructure as the mass ratio increases to 3.2, 4.2 and 6, respectively, as shown in Figure 6-42(c), (d) and (e), respectively.

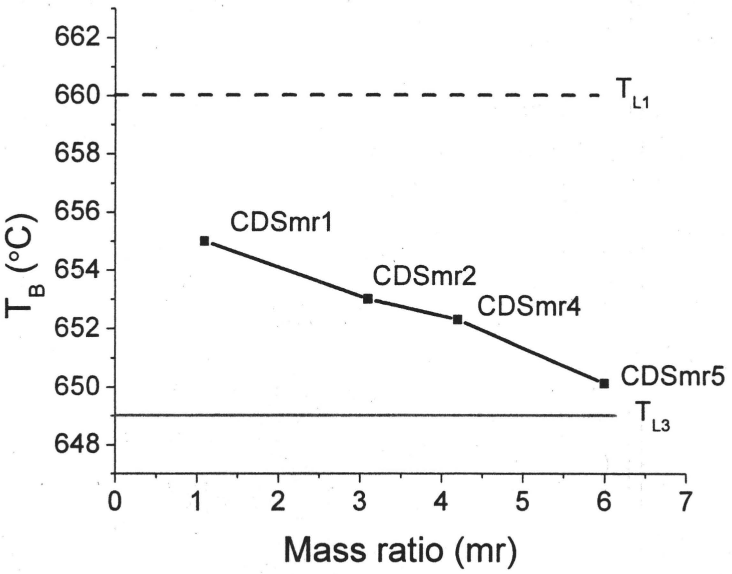

Figure 6-41 Typical thermal data of point B (refer to Figure 6-4) taken from the thermal data of the experiments in Table 6-4.

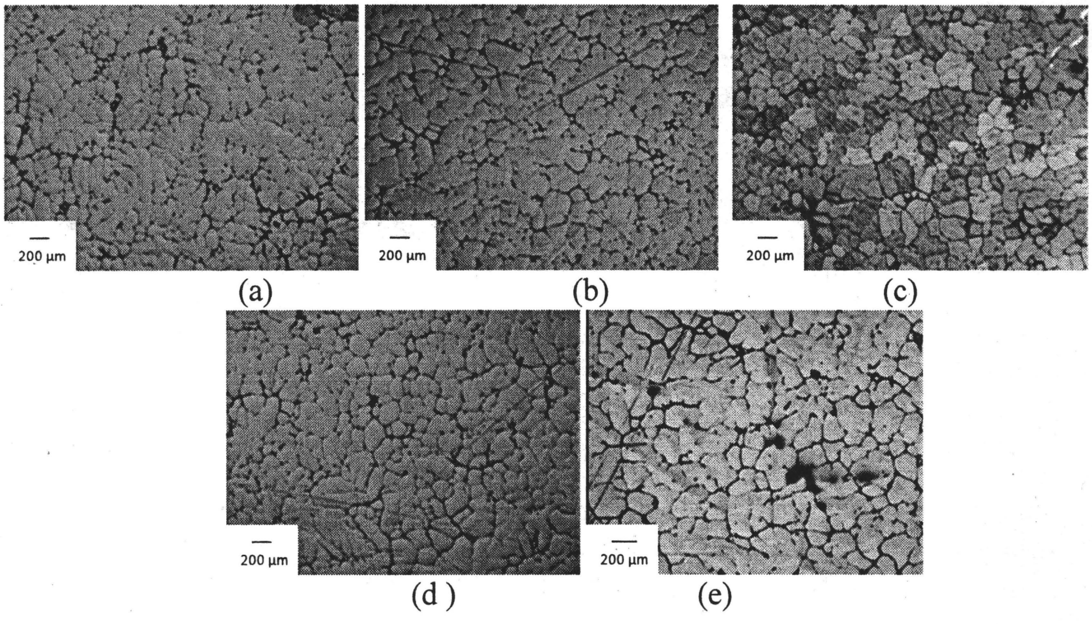

Figure 6-42 Typical microstructure from light optical microscope for CDS samples from difference mass ratio shown in Table 6-4, (a) CDSmr1 (mr1.1), (b) CDSmr2 (mr2), (c) CDSmr3 (mr3.2), (d) CDSmr4 (mr4.2) and (e) CDSmr5 (mr6).

The results of changing the mass ratio to obtained Al-4.7wt% Cu resultant alloy show that the lower mass ratio (less than 2) is not favourable in the CDS process for the Al-Cu system because the dendritic microstructure forms in the casting sample whereas, the non- dendritic microstructure is obtained for mass ratio greater than 3. Typically in a commercial casting process, a suitable mass ratio of the precursor alloys could be so chosen such that there is an appreciable undercooling of the point B of at least 8 K.

6.3.4 Rate of Mixing Alloy1 into Alloy2

The effect of two rates of mixing were investigated on the morphology of the primary Al phase in the solidified sample in the laboratory CDS experiments for the Al-4.7 wt% Cu (mr6) alloy: 167 gs^{-1} and 113 gs^{-1}, by using two funnel diameters of 9 and 6 mm, respectively. Figure 6-43 shows the graphical relationship between the average grain size and superheat temperature of Alloy1. At lower superheat temperatures, the experiments carried out with a mixing rate of 113 gs^{-1} shows a smaller grain size and the rate of increase of grain size for the lower mixing rate is slower which is more favorable. The slower increase in grain size with the T_l for the lower mixing rate is because of the increased number of nucleation event of the primary Al phase during the mixing stage as explained in Section 6.2.1. Commercially a larger allowable range of superheat temperatures of Alloy1 for a successful CDS process is more favorable and hence, a slower rate of mixing is more favorable, as well.

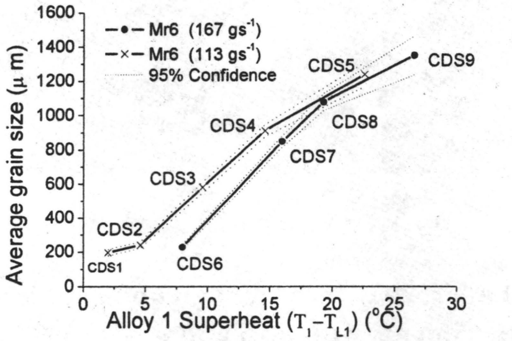

Figure 6-43: Relationship between average grain size and superheat temperature of Alloy1 for the two rates of mixing in the laboratory CSD experiments presented in Table 5-1 of Section 5.1.2.1: 113 gs^{-1} and 167 gs^{-1}.

Figure 6-44 shows the typical microstructures of the samples used for the grain size assessment in Figure 6-43 for the mixing rate of 113 gs^{-1}. the morphology of the primary Al phase is predominantly non-dendritic for $T_l \leq 20$ °C and this compared to the lower range of T_l (10 °C) when the mixing rate was 167 gs^{-1} as shown by the results in Figure 6-37. The lower rate of mixing Alloy1 into Alloy2 is favorable for an improved CDS process and the use of an increased range of temperature for the Alloy1 (commercially more viable); however, the mixing rate could not be lowered indefinitely, because mixing process should terminate prior to the equalization of the temperature field in the resultant mixture and the formation of the cells forming Area2 in the mixture.

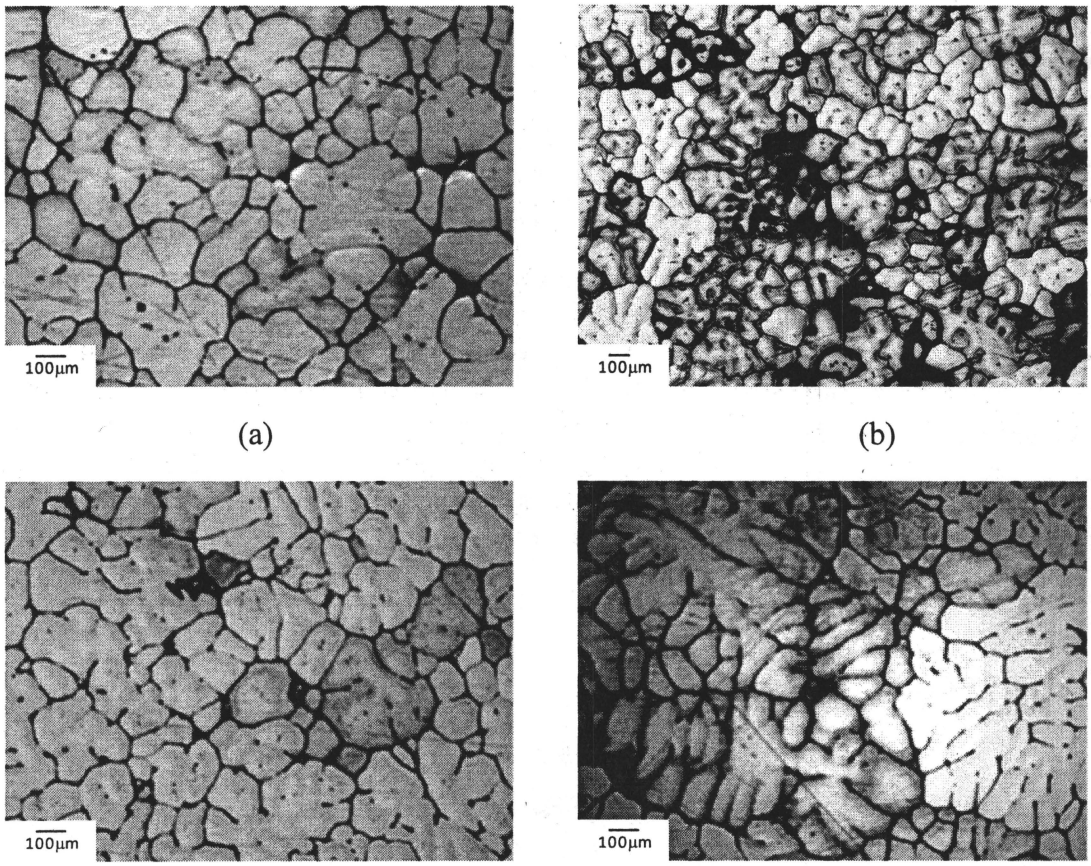

(a) (b)

(c) (d)

Figure 6-44: Typical microstructure from an optical microscope from samples in the laboratory CDS experiments with mr6 and mixing rate of 113 g/s as described in Table 5-1. (a) CDS6 (T_1 = 668 °C), (b) CDS7 (T_1 = 676 °C), (c) CDS8 (T_1 = 680 °C), and (d) CDS9 (T_1 = 687 °C)

6.4. *Verification of the Proposed Mechanism*

The proposed events during a successful CDS process for the Al-Cu alloy were validated with for various solute types using the following alloy systems.

- Al-Si
- Al-Zn Alloy (7050)

- Organic Alloys
    - Succinonitrile-Acetone (SCN-Ac)
    - Succinonitrile-D-Camphor (SCN-DC)
    - Succinonitrile-water (SCN- H_2O)

6.4.1Al-Si alloy

Al-1.8 wt% Si alloy was cast using the CDS process with the experiment condition shown in Table 6-5.

Table 6-5: Experiment conditions to cast Al – 1.8 wt% Si alloy with CDS process

Parameters	Level
Alloy1	Pure Al with T_{L1} = 660 °C
Alloy2	Al – 12.7 wt% Si (eutectic) with T_{L2} = 578 °C
T_1	665 °C
T_2	582 °C
Mass ratio	mr6
Rate of Mixing	167 gs^{-1}

Figure 6-45 (a) and (b) shows the typical microstructure of the primary Al phase obtained from samples cast with the CDS process and conventional solidification process, respectively; wherein it could be observed that the morphology of the primary Al phase obtained in the CDS was predominantly non-dendritic as compared dendritic Al phase in the conventional casting in which the Al - 1.8 wt% Si alloy was poured at 665 °C into an empty crucible maintained at 570 °C.

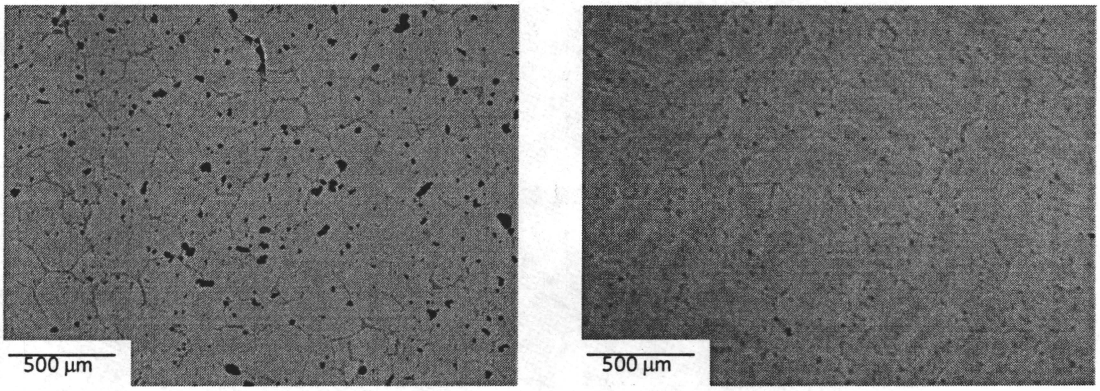

(a) (b)

Figure 6-45 Typical microstructure of Al – 1.8wt% Si alloy cast with the CDS process with the parameters listed in Table 6-5. (a) CDS process and (b) Conventional solidification.

The results show that the favourable parameters (Table 6-5) chosen from our understanding of the events during the CDS process in this study were successful in carrying out a successful CDS process.

6.4.2 Al-Zn Alloy (7050)

Al- Zn alloy (7050) was cast via CDS process with the experiment setup shown in Figure 5-4 and conditions shown in Table 6-6. Figure 6-46 (a) and (b) show the location of the Alloy1 and Alloy2 on the phase diagram with their respective liquidus temperatures. The thermal curve during solidification was ascertained to verify the liquidus temperatures of Alloy1 and Alloy2. The CDS casting of the resultant alloy was re-melted at 665°C and solidified conventionally in air in the same crucible.

Table 6-6 Experiment conditions to cast 7050 Al-Zn alloy via CDS process

Parameters	Level
Alloy1	Al-2.67wt%Mg-2.5wt%Cu with $T_{L1} = 641$ °C
Alloy2	Al – 42.5 wt% Zn with $T_{L2} = 602$ °C
Alloy3	Al-5.97wt%Zn-2.3wt%Mg-2.16wt%Cu
T_1	646 °C
T_2	615 °C
Mass ratio	mr6

Figure 6-47 (a) and (b) shows a typical microstructure of the primary Al phase obtained from samples cast via CDS and conventional solidification processes, respectively; wherein it could be observed that the primary Al phase morphology obtained in the CDS was predominantly non-dendritic whereas in conventional casting it was dendritic.

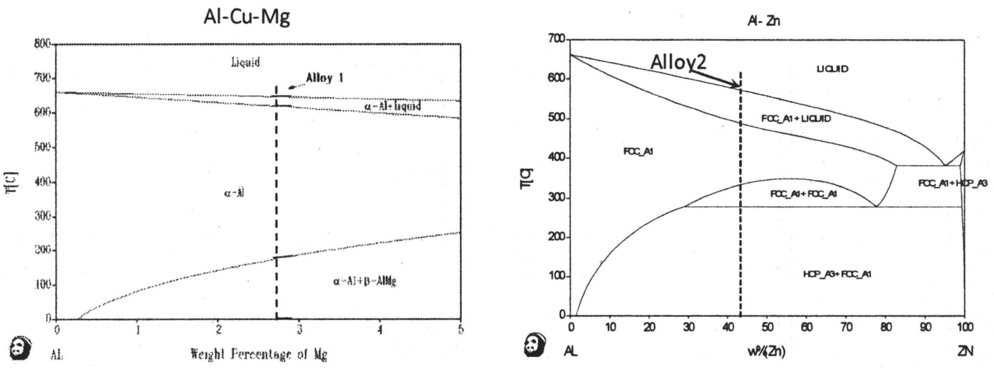

(a) (b)

Figure 6-46 Typical phase diagram of the two precursor alloys for CDs casting of 7050 Al alloy, (a) isopleth of Al-Cu-Mg phase diagram to represent Alloy1 and (b) Al-Zn binary phase diagram to represent Alloy2.

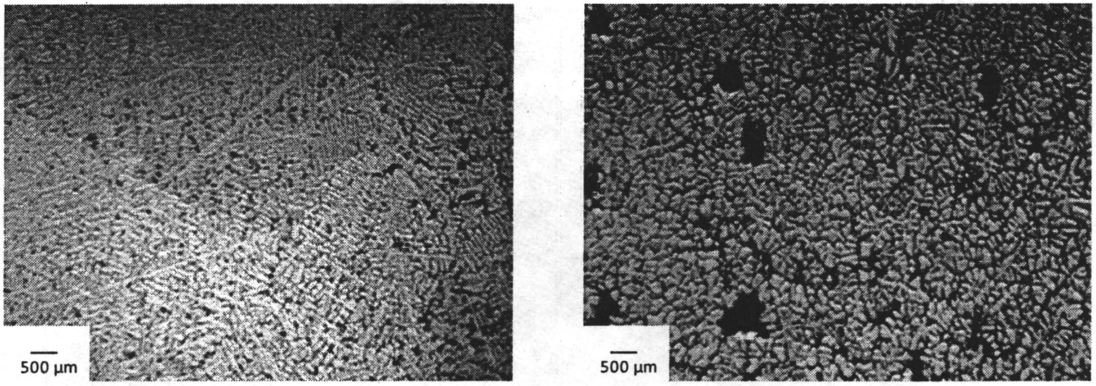

(a) (b)

Figure 6-47 Typical microstructure of 7050 alloy (a) conventional solidification and (b) cast via CDS process with the parameters listed in Table 6-6.

The results shown in Figure 6-47 verifies the validity of the CDS process and effect of parameters on the same and shows one of the favourable parameters to shape cast the 7050 Al wrought alloy by the CDS process.

6.4.3Organic Alloys

Three organic alloys were investigated to verify our understanding of the events during a successful CDS process: SCN – 2.5 wt% Ac; SCN – 2 wt% DC and SCN – 1 wt% H_2O. Figure 6-48 (a), (b) and (c) show the binary phase diagram for above organic systems respectively.

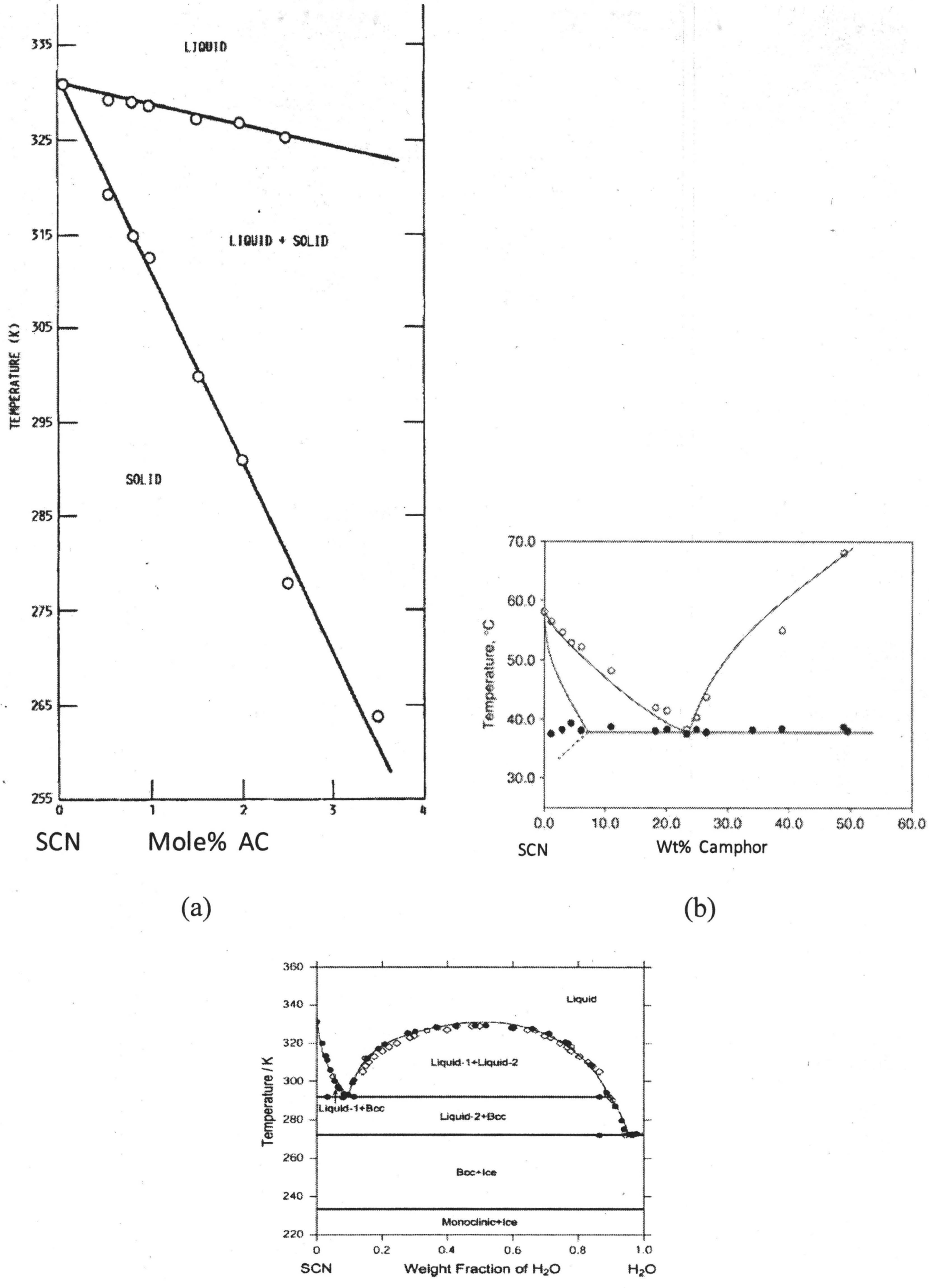

(c)

Figure 6-48: Binary alloy phase diagram for the organic alloys. (a) SCN – Ac [120], (b) SCN – DC [121], and (c) SCN – H_2O [122].

Table 6-7: Experiment conditions to cast the three organic alloys alloy with CDS process

Alloy	Parameters	Level
SCN – 2.5 wt% Ac	Alloy1	Pure SCN with T_{L1} = 57.8 °C
	Alloy2	SCN – 6.5 wt% Ac with T_{L2} = 51 °C
	T_1	58.8 °C, 61.6 C°C,65.5 °C and 72.1 °C.
	T_2	53.6 °C
	Mass ratio	mr1.6
SCN – 2 wt% DC	Alloy1	Pure SCN with T_{L1} = 57.8°C
	Alloy2	SCN – 5 wt% DC with T_{L2} = 53 °C
	T_1	59 °C
	T_2	54 °C
	Mass ratio	mr1.5
SCN – 1 wt% H_2O	Alloy1	Pure SCN with T_{L1} = 57.8 °C
	Alloy2	SCN – 6.5 wt% H_2O with T_{L2} = 24 °C
	T_1	59 °C
	T_2	25 °C
	Mass ratio	mr2.5

Figure 6-49 shows the typical microstructure for the SCN – 2.5 wt%Ac alloy solidified by the CDS process as shown by the experiment parameters in Table 6-7 for the four increasing values of T_1. In Figure 6-49, the morphology of the primary SCN phase in the solidified microstructure is initially predominantly non-dendritic for lower values of T_1 and becomes more dendritic at higher values.

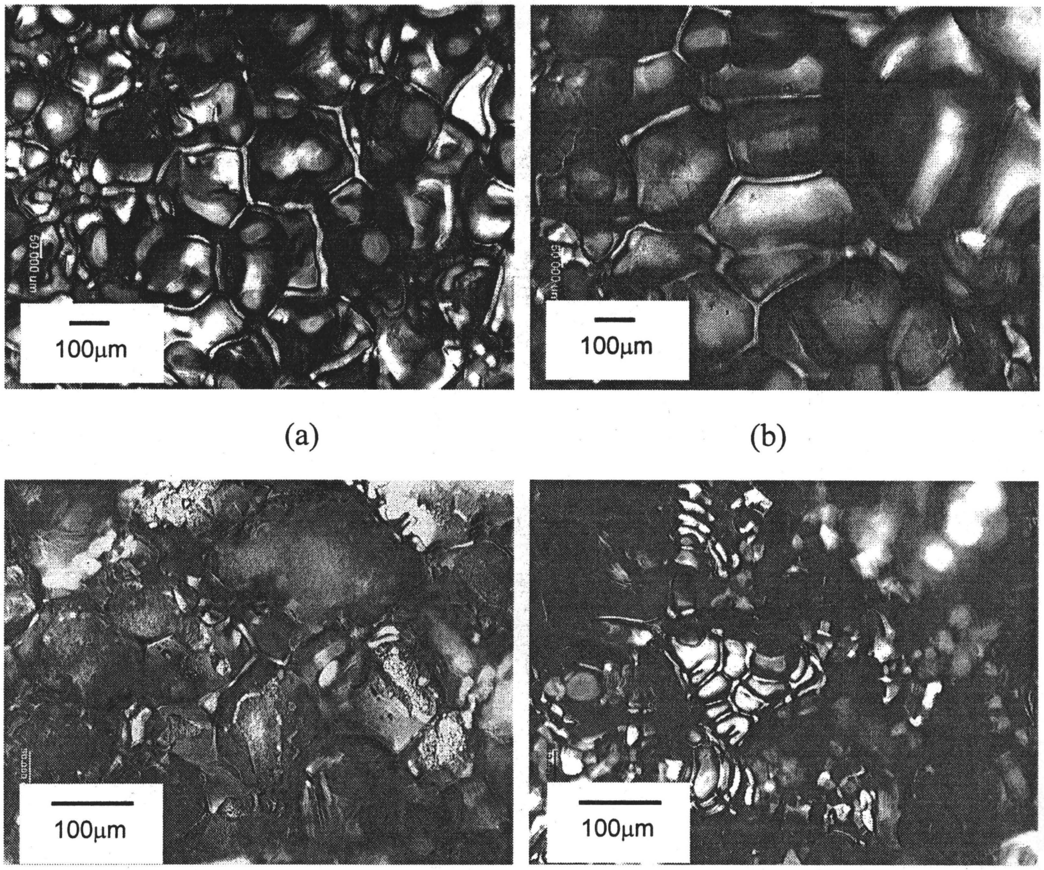

(a) (b)

(c) (d)

Figure 6-49: Typical microstructure of samples of SCN – 2.5 wt% Ac alloy solidified by CDS process. The value of T_1 were (a) 58.8°C, (b) 61.6 °C, (c) 65.5 °C, and (d) 72.1°C, and the experimental parameters are listed in Table 6-7.

Figure 6-50 (a) and (b) shows the typical microstructures for eth SCN – 2 wt% DC alloy solidified by the CDS process (Table 6-7) and conventional process, respectively. The morphology of the primary SCN phase is predominantly non-dendritic in the CDS process and that in the conventional solidification is dendritic.

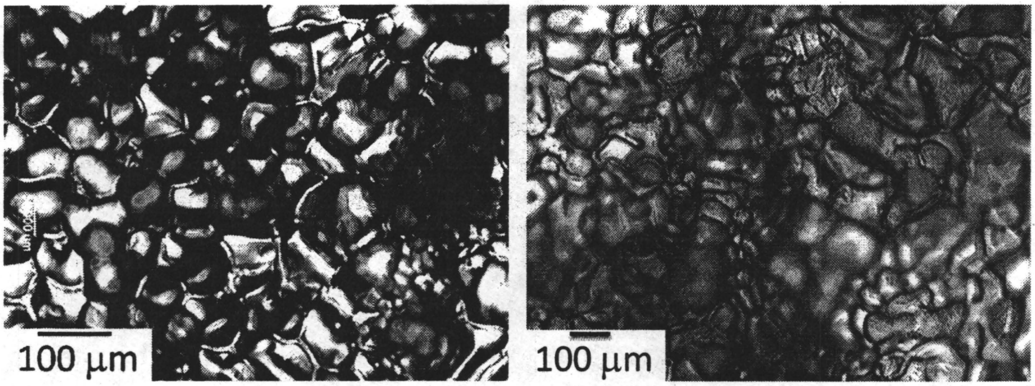

(a) (b)

Figure 6-50: Typical microstructure of samples of SCN – 2 wt% DC alloy solidified by (a) CDS process with the experimental parameters are listed in

Table 6-7 and (b) conventional solidification.

Figure 6-51(a) and (b) shows the typical microstructures for the SCN – 1 wt% H_2O alloy solidified by the CDS process (Table 6-7) and conventional process, respectively. The morphology of the primary SCN phase is predominantly non-dendritic in the CDS process and that in the conventional solidification is dendritic.

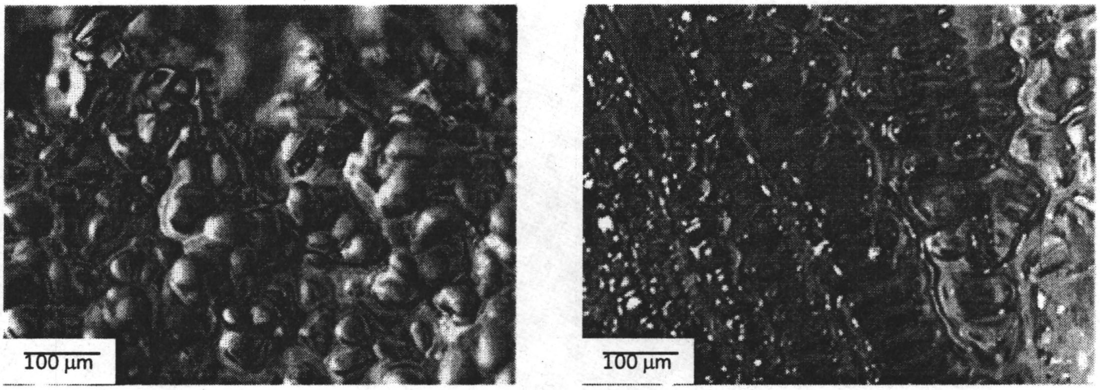

(a) (b)

Figure 6-51: Typical microstructure of samples of SCN – 1 wt% H_2O alloy solidified by (a) CDS process with the experimental parameters are listed in Table 6-7 and (b) conventional solidification.

The results of the experiments with the organic alloys show that the experiment parameters chosen for a successful CDS process with the in-depth understanding of the events developed in this study proved successful and the trend of the morphology of the primary SCN phase with increasing values of T_1 in Figure 6-49 is similar to that obtained in the Al-Cu system as shown in Figure 6-37.

The verification study was carried out to corroborate the fact that the various events proposed for the CDS process in this study seem to be accurate.

CHAPTER 7. SUMMARY AND CONCLUSION

The study had successfully led to a more in-depth understanding of the various events occurring during a successful CDS process. A master's level graduate project [31] was carried out in tandem with this study to utilize the understanding developed in this study to develop viable commercial casting processing routes to cast Al based wrought alloys such as 2024, 6082 and 7075 alloys with the CDS process. The results of that study were successful and some salient results were presented in Section 4.1 of this dissertation. Utilizing the results of this study would enable the successful casting Al based wrought alloys into near net shaped components using the CDS process without much change to the economics of the casting process.

The following presents a brief list of events in a CDS process:

Event (1) *Start of the mechanical mixing* at point A and end around point B.
Event (2) *Heat added to the system from Alloy1* (enthalpy of Alloy1) depending on the thermal mass of Alloy1.
Event (3) *Nucleation of primary phase of Al takes place from Alloy1.* The enthalpy of fusion from the nucleation event would be released into the mixture during the mixing process.
Event (4) *Re-distribution of the thermal and solute fields* by diffusion/convection occurs in the mixture in the macro-scale.
Event (5) *Formation of cells* in the micro-scale with lower Cu concentration on the middle of the cell and higher Cu concentration in the cell boundaries.
Event (6) *Re-distribution of thermal and solute fields inside cells* in micro-scale.
Event (7) *Nucleation of primary Al phase inside cells.*
Event (8) *Final nucleation event* at point D from the pockets of liquids with nearly homogeneous Cu concentration.
Event (9) *Growth of primary Al grain from nucleation events listed in Events 3, 7 and 8, respectively.*

There is a complex interplay among the above listed events and the critical parameters that affect the thermal and temporal fields of these events are listed below:

- Temperature of Alloy1 (T_1)
- Temperature of Alloy2 (T_2)
- Mass ratio
- Rate of mixing (Alloy1 into Alloy2)

When considering developing a strategy to cast an Al based cast or wrought alloys with typically three or more solute elements, the following could be adopted as the initial consideration for developing a successful list of alloy and process parameters:

- An in-depth study of the various isopleths of the multicomponent phase diagram including all the critical solute elements would lead to:
    - A favorable composition of the two precursor alloys: Alloy1 and Alloy2; such that the mass ratio of mixing the alloys would be at least 3.
    - Identifying the compositions of Alloy1 and Alloy2 would identify the respective liquidus temperatures as well. Typically the difference between these liquidus temperatures would have to be greater than 30 °C. If there are more than one possible combination of pre-cursor alloys (as the case in most systems), the largest difference between the respective liquidus temperatures of the precursor alloys would typically be preferred.
    - The rate of mixing the alloys would typically be preferred to be low. However, a few simple experiments would yield the time to attain the maximum temperature of the resultant mixture and the mixing rate should be such that the Alloy1 with the higher thermal mass should be fully poured into Alloy2 with the lower thermal mass prior to the resultant mixture attaining the maximum temperature during mixing.
    - The superheat temperature of Alloy1 above its liquidus temperature would typically have to be about 5 to 10 °C and that for Alloy2 could be about 20 °C. The higher the mass ratio of mixing, the more freedom one would have an increasing the initial superheat temperature of Alloy2.
    - Typically the crucible used for mixing the two alloys should be maintained at a temperature close to the initial temperature of Alloy2 so that the heat extracted by the environment is limited prior to casting the resultant mixture and this enables the successful completion of the three nucleation events in the mixture and enable a nearly non-dendritic growth morphology in the resultant solidified component.
    - The resultant mixture would have to be let to sit for a few seconds (~5 s) prior to injection of the mixture into a die mould cavity for casting. This would ensure an initial stable growth of the S/L interface from all the nucleation events to enable nearly non-dendritic primary phase morphology in the resultant cast microstructure.

The above-mentioned steps are merely a guideline to initiate the design of the alloy and process parameters for a successful CDS process of an Al alloy. Each alloy would exhibit individually unique characteristics and these would have to be treated on a case by case basis.

In conclusion, this study has shown that the solidification characteristics (nucleation and growth) observed in a CDS process is uniquely and significantly different from those observed in a conventional casting process and semi-solid rheocasting process, alike.

There are typically three types of nucleation events and the stability criteria for each of these nucleation events are uniquely different. The Area1 of the microstructure are large primary Al grains that would nucleate in the pockets of liquid of Alloy1 distributed in the resultant mixture at an undercooled temperature below the liquidus of Alloy1 and the growth would primarily be stable with a non-dendritic phase morphology. The Area2 consisting of cells formed immediately after the end of the mixing process due to the large difference in the surface tension and density of between Alloy1 and Alloy2, would present a favorable thermal and solute field for a nucleation event depending on the type and rate of re-distribution of these fields inside the cells forming Area2. The growth morphology of the phase form nuclei in Area2 would be increasingly stable until the solute field is equalized and begin to become unstable subsequently. However, the limited solidification time available after the equalization of the solute fields in Area2 would limit the extent of breakdown of the growing S/L interface in these areas and typically a worst case scenario would present a rosette shaped morphology of the primary Al phase in the final microstructure. Nucleation and growth in Area3 consisting of a nearly homogeneous solute and thermal field would take place like that in a conventional solidification process. The size of this area of liquid in the process would determine the extent of breakdown of the growing S/L interface and larger value of superheat temperature of Alloy1 would increase the amount and size of Area3 in the mixture resulting in a more dendritic morphology of the primary Al phase. Hence, the objective to attain a successful CDS process would be to increase the breakdown of Alloy1 during mixing, increase the amount of liquid mixture with Area2 and limit the amount of Area3. This could be achieved by maximizing the turbulence dissipation energy during mixing without causing air entrapment bubbles, ensure a large difference in surface extension and density between Alloy1 and Alloy2 and limiting the superheat temperature above the liquidus temperature of Alloy1 to a minimum possible for a commercial process.

CHAPTER 8. RECOMMENDATION FOR FUTURE WORK

Based on this study, the following would be the recommendation for future work on this topic:

- Develop viable process and equipment for successful mixing of Alloy1 with Alloy2 without formation of air bubbles during mixing and ensuring a high rate of turbulence dissipation energy.
- Develop a numerical model for the nucleation and growth of the primary Al phase from the pockets liquid of Alloy1 dissipated throughout the mixture during the mixing process.
- Develop a numerical model to incorporate the effect of fluid flow within the cells forming Area2 of the microstructure to enable a better understanding of the re-distribution of the thermal and solute fields inside these cells and further develop the model to predict the growth of the primary Al grains nucleated within these cells.
- Develop favorable compositions of solute elements in specific families of Al based wrought alloy such that these compositions would dictate a successful CDS process of these alloys to attain a near net shaped component. The properties of these alloy families could be marginally compromised to achieve near net shaped casting of these alloys. The final properties of the components with these wrought alloys would still be superior to the cast alloy counterparts. It should be noted that the as-cast properties of most Al wrought alloys would be poorer than the cast alloy counterparts and specific controlled heat treatment procedures of the components cast with wrought alloys result in a significantly higher properties and performance.
- Develop specific heat treatment procedures for components cast by the CDS process with specific Al based wrought alloys. Since the mechanism of solidification in a CDS process is vastly different from other casting processes, the solute re-distribution in the resultant cast component would also be significantly different and specific heat treatment procedures would have to be developed from fundamentals to successfully achieve superior properties and performance. The mechanism of solute distribution in a CDS process would be better understood from this dissertation and this information could be used to design new heat treatment cycles.
- The CDS process would be extended to other commercial important alloys systems such as Fe and Mg based alloys. Feasibility studies are warranted to establish a proof-of-concept of the CDS process for these systems.

CHAPTER 9. REFERENCES

1 B. Upton, Pressure Die Casting, Part 1, Promsyrioimport, Moscow, USSR, (1978).

2 Z. Fan, X. Fang, S. Ji, Materials Science and Engineering, 412 (2005) 298-306.

3 Girish Kumar, Sathyapal Hegde, K. Narayan Prabha, Journal of Materials Processing Technology, 182 (2007) 152-156.

4 D.G.Eskin, Suyitno and L. Katgerman, Progress in Materials Science, 49 (2004) 629-711.

5 Davies, solidification and casting, John Wiley & sons, Canada, (1973).

6 M. Rappaz, J.M. Drezet, and M. Gremaud, Metallurgical and Materials Transactions A, v 30A, February, (1999) 449-455..

7 M. C. Flemings, Metallurgical Transactions A, v 22A, May (1991) 957.

8 www.nrc-cnrc.gc.ca, National Research Council Canada.

9 S. Chayong, H.V. Atkinson, P. Kapranos, Materials Science and Engineering, A390 (2005) 3–12.

10 Science and Technology of Semi-Solid Metal Processing, Ed. Anacleto de Figueredo, North American Die Casting Association, (2001).

11 J. G. SIM et al, ISIJ International, v49, n 11, (2009) 1700–1709.

12 D. Saha, S. Shankar, D. Apelian and M. M. Makhlouf, Metallurgical and Materials Transaction A, v.35A, July, (2004). 2147

13 Symeonidis, PhD thesis, Worcester Polytechnic Institute, April, (2009).

14 SIM et al, ISIJ International, v 49, n 11, (2009) 1700–1709.

15 Freitas et al, Materials Science and Engineering, A 479 (2008) 171–180.

16 Canadian Aluminium Transformation Technology Roadmap, 2006 Edition Complete Version, National Research Council Canada and Réseau Trans-Al, Reseau Trans-Al Inc., QC, Canada, (2007).

17 C.G. Goetzl and J.L. Ellis, U.S. Patent 2,611,443, September 30 (1952).

18 G. Langford, R. E. Cunningham, Metallurgical Transactions B, v 9B, (1978) 5-19.

19 D. Apelian and G. Langford, Rapid Cycle Casting of Steel, (1980).

20 D. Saha, S. Shankar, D. Apelian and M. Makhlouf, Proceedings of the John Campbell Honorary Symposium Edited by P. Crepeau and M. Tiryakioglu TMS (The Minerals, Metals & Materials Society), (2004)

21 S. Shankar, private communications, Department of Mechanical Engineering, McMaster University, Hamilton, ON, Canada L8S 4L7.

22 D. Apelian, M.M. Makhlouf, and D. Saha, Materials Science Forum, v 519-521 (2006) 1771-1776.

23 David. R. Caskell, Introduction to the Thermodynamics of materials, Third Edition, Taylor & Francis, (1995).

24 D.A. Porter, and K.E. Easterling, Phase transformations in metal and alloy, second addition, CRS Press, UK, (2004).

25 E. Cini, B. Vinet and P. J. Desr, Philosophical Magazine, v.80, n.4, (2000) 955-966.

26 A.Das, S. Ji, Z. Fan, Acta Materialia, 50 (2002) 4571-4585.

27 W. Shusen. W. Xueping, and X. Zehui, Acta Materialia, v 52 (2004) 3519-3524.

28 P. Ashtari, G. Birsan and S. Shankar, Shape Casting The 3rd International Symposium, Ed. J. Campbell, P. N. Crepeau, M. Tiryakioglu, TMS (The Minerals, Metals and Materials Society), Warrendale, PA, USA, (2009) 223-230.

29 A. Khalaf, P. Ashtari and S. Shankar, Shaped Casting:The 3rd International Symposium, Ed. J. Campbell, P. N. Crepeau, M. Tiryakioglu, TMS (The Minerals, Metals and Materials Society), Warrendale, PA, USA, (2009), 215-222.

30 A. A. Khalaf, P. Ashtari, and S. Shankar, Metallurgical and Materials Transactions B, v 40B, December (2009) 843.

31 Gabriel Birsan, Master Thesis, Mechanical Engineering, McMaster University (2009).

32 Z. Fan, International Materials Reviews, v 47, n 2 (2002) 49.

33 D.B. Spencer, R. Mehrabian, and M.C. Flemings, Metallurgical Transaction, v 3, July (1972) 1925.

34 G. Kim, M. Koç, R. Mayor and J.Ni, Journal of Manufacturing Science and Engineering, v 129, April, (2007) 237.

35 H.V. Atkinson, Progress in Materials Science, 50 (2005) 341–412.

36 G. R. Burgos, A.N. Alexandrou and V. Entov, Journal of Materials Processing Technology, 110 (2001) 164-176.

37 S. Nafisi and R. Ghomashchi, Materials Characterization 57,(2006) 371-385.

38 M. Qian, Acta Materialia, 54 (2006) 2241–2252

39 B.S. Murty, S.A. Kori, K. Venkateswarlu, R.R. Bhat, M. Chakraborty, Journal of Materials Processing Technology, v 89–90 (1999) 152–158.

40 Z. Yang, C.G. Kang, P.K. Seo, Scripta Materialia, 52 (2005) 283–288.

41 Y. Birol, Journal of Materials Processing Technology, 186 (2007) 94–101

42 Y. c. Birol, Journal of materials processing technology, 207 (2008) 200–203

43 Q.D. Qin, Y.G. Zhao, P.J. Cong, W. Zhou, B. Xu, Materials Science and Engineering, A 444 (2007) 99–103

44 T. Hagaa and P. Kapranosb, Journal of Materials Processing Technology, 130-131 (2002) 581–586.

45 G. Wang, P. Lu, H.Y. Wang, Q.C. Jiang, Materials Letters, 58 (2004) 3852–3856.

46 Q.Q. Zhang, Z.Y. Cao, Y.F.Zhang, G.H.Su, Y.B. Liu, Journal of Materials Processing Technology, 184 (2007) 195–200.

47 H.Q. Lin, J.G. Wang, H.Y. Wang, Q.C. Jiang, Journal of Alloys and Compounds, 431 (2007) 141–147.

48 J.G. Wang, P. Lu, H.Y. Wang, J.F. Liu, Q.C. Jiang, Journal of Alloys and Compounds, 395 (2005) 108–112.

49 J.G. Wang, H.Q. Lin , Y.Q. Li, Q.C. Jiang, Journal of Alloys and Compounds, 457 (2008) 251–258.

50 Zhanga et al, Journal of materials processing technology, 209 (2009) 792–797.

51 Y. Kwon, Z. Lee, Materials Science and Engineering, A360 (2003) 372- 376.

52 Nafisi et al, Acta Materialia, 54 (2006) 3503–3511.

53 Jun et al, Journal of Alloys and Compounds, 470 (2009) 228–232.

54 M. C. Flemings, Solidification Processing, McGraw Hill, (1974).

55 J. Jorstad, High Integrity Die Casting, chapter 3, North American Die Casting Association (NADCA), Rosemont, IL, USA, July (2008).
56 P.K. Seo a, D.U. Kimb, C.G. Kangc, Journal of Materials Processing Technology, 176 (2006) 45–54.
57 NADCA Product Specification Standards for Die Casting Produced by the Semi-Solid and Squeeze Processes, North American Die Casting Association (NADCA), Rosemont, IL, USA, v 5, (2009).
58 M.M. Rovira, B.C. Lancini, M.H. Robert Journal of Materials Processing Technology, 92-93 (1999) 42-49.
59 E.J. Zoqui Journal of Materials Processing Technology, 143–144 (2003) 195–201.
60 P.K. Seoa, S.M. Leeb, C.G. Kang, Journal of materials processing technology, 209 (2009) 171–180.
61 G. Hongmin1, Y. Xiangjie and H. Bin Journal of Wuhan University of Technology-Mater, Sci. Ed. Feb. (2008).
62 J.L. Jorstad, private communications, JLJ Technlogies Inc., USA
63 D. Brabazon, D.J. Browne , A.J. Carr Materials Science and Engineering, A326 (2002) 370–381.
64 Zhang Xiao-li, Li Ting-ju, Xie Shui-sheng, Teng Hai-Tao, Jin Jun-ze, Journal of materials processing technology, 209 (2009) 2092–2098.
65 P.K. Seoa, S.M. Leeb, C.G. Kangc, Journal of materials processing technology, 209 (2009) 171–180.
66 K. Sukumaran a, B.C. Pai a, M. Chakraborty, Materials Science and Engineering, A369 (2004) 275–283.
67 S. Nafisi and R. Ghomashchi, Materials Characterization, 57 (2006) 371–385.
68 H. Mirzadeh, B. Niroumand, Journal of Alloys and Compounds, 474 (2009) 257–263.
69 Z. Fan, Materials Science and Engineering, A 413–414 (2005) 72–78.
70 D. Brabazon, D.J. Browne, A.J. Carr Materials Science and Engineering, A326 (2002) 370–381.
71 Y. Birol, Journal of Alloys and Compounds, 480 (2009) 365–368.
72 T. Li, X. Lin and W. Huang, Acta Materialia, 54 (2006) 4815–4824.
73 M. Reisi and B. Niroumand, Journal of Alloys and Compounds, 475 (2009) 643–647.
74 S. Tahamtan, A.F. Boostani and H. Nazemib, Journal of Alloys and Compounds, 468 (2009) 107–114.
75 M. Reisi, B. Niroumand, Journal of Alloys and Compounds, 470 (2009) 413–419.
76 M. Hitchcock, Y. Wang and Z. Fan, Acta Materialia, 55 (2007) 1589–1598.
77 P. Falak and B. Niroumand, Scripta Materialia, 53 (2005) 53–57.
78 B. Niroumand and K. Xia, Materials Science and Engineering, A283 (2000) 70–75.
79 P.K. Seo, D.U. Kim and C.G. Kang, Journal of Materials Processing Technology, 162-163 (2005) 570-578.
80 C.G. Kang, J.W. Bae and B.M. Kim, Journal of Materials Processing Technology, 187–188 (2007) 344–348.
81 D. H. Kirkwood, Semi-solid Processing of Alloys, Springer, November, (2009).

82 T. Okubo, J. Okamoto and A. Tsuchida, Colloid Polym Science, 287 (2009) 645–657.

83 E.R.G. Eckert and R.M. Drake, Heat and Mass Transfer, second edition, McGraw Hill, Toronto (1959).

84 K. Eckert, M. Besthorn and A. Thess, J. Fluid Mech., v 356, (1998) 155-197.

85 A. I. Mizev and D. Schwabe, Physics of Fluids, **21**, 112102, (2009).

86 C. B. Sobhan and G. P. Peterson, Microscale and NanoScale Heat Transfer, CRC Press, (2008).

87 Z.Y. Guo and Z.X. Li, International Journal of Heat and Fluid Flow, 24 (2003) 284–298.

88 Z.Y. Guo and Z.X. Li, International Journal of Heat and Fluid Flow, 46 (2003) 149–159.

89 P. Stephan and J. Kern, International Journal of Heat and Fluid Flow 25 (2004) 140–148.

90 T. Nishimura, International Journal of Heat and Mass Transfer, 31 (1999) 1479-1489.

91 J. Tanny and B. Yakubov, International Journal of Heat and Mass Transfer, 45 (2002) 2101–2105.

92 M. Lamsaadi, M. Naımi, M. Hasnaoui, Energy Conversion and Management 47 (2006) 2535–2551.

93 M.M. Malik et al, Journal of Non-Newtonian Fluid Mechanics, 165 (2010) 733–742.

94 J. W. Rutter and B. Chalmers, Can. Journal of Physics, 31 (1953) 15.

95 W. W. Mullins and R. F. Sekerka, Journal of Applied Physics, 35 (1964) 444.

96 G. Muller, J. J. Metois and P. Rudolph, Crystal Growth from Fundamentals to Technology, Elsevier (2004).

97 Y. Ogasawara, K. Eda and A. Kitada, Journal of the Physical Society of Japan, v 74, n. 9, September, (2005) 2439–2442.

98 S. O. Hara, A. Tarshis and R. Viskanta, Journal of Crystal Growth, 3-4 (1968) 583-593.

99 R. F. Sekerka, Journal of Applied Physics, v 36 January, (1965) 264.

100 R. F. Sekerka, Journal of Crystal Growth, 128 (1993) 1-12.

101 D. E Holmes and H. C. Catos, Journal of Applied Physics, 42 (4) April (1981).

102 W. W. Mullins and R. F. Sekerka, Journal of Applied Physics, 34 February, (1963) 323.

103 B.K. Dhindaw, L. Kumar, N. C. Amer AlKarkhi and H. Fredriksson, Materials Science and Engineering, A 413-414 (2005) 165-164.

104 R. A. Martinez, A. Karma, and M.C. Flemings, Metallurgical and Materials Transactions A, v 37A, September (2006) 2807-2815.

105 M. Qian, Acta Materialia, 54 (2006) 2241-2252.

106 M. Hitichcock, Y. Wang and Z. Fan, Acta Materialia, 55 (2007) 1589-1598.

107 V.S Zolotorevsky, N. Belov, M. Glazoff, Casting Aluminum Alloys, Moscow, Pittsburgh, (2007).

108 M.Gupta, L. Lu and S.E. Ang, Journal of Materials Science, v 32, n 5, March, (1997) 1261-1267.

109 V. Vishan and A.V. Narlikar, Mat. Res. Bull, v II, (1976) I257-1264.
110 G.Y.Liu, Master Thesis, Mechanical Engineering, McMaster University (2009).
111 A T Dinsdale and P N Quested, ISSN 0018-151X, High Temperature, v 47, n 3, (2009) 336–341.
112 S. B. Pope, Turbulent Flow, Cambridge university press, (2000).
113 Y. A. Cengel and M. A. Boles, Thermodynamics An Engineering Approach, sixth Edition, Mc Graw Hill, (2008).
114 Y. A. Cengel and J. M. Cimbala, Fluid Mechanics Fundamentals and Applications, Second Edition, Mc Graw Hill, (2010).
115 W. Kurs and D. J. Fisher, Fundamentals of Solidification, Third Edition, Trans Tech Publications, USA, (1989).
116 Y. Du et al, Materials Science and Engineering, A363 (2003) 140–151.
117 ASM Handbook committee, Metals Handbook, Metallographic, Structure and Phase diagram, v8, 8th Edition, American Society for Metals (1973).
118 H. Bruus, Theoretical Microfluidics, Oxford University Press, (2008).
119 L. Nastac and D. M. Stefanescu, Modeling of Casting, Welding and Advanced Solidification Processes, vI, (1993).
120 M. A. Chopra, M. E. Glicksman and N. B. Singh, Metallurgical Transactions A, v19A, December (1988) 3087.
121 J. Teng and S. Liu, Journal of Crystal Growth, 290 (2006) 248-257.
122 S. Zhang, Z. K. Liu and Q Han, Journal of Phase Equilibria and Diffusion, v 29, n3, (2008).